Universität Bonn

Physikalisches Institut

Measurement of the top quark mass in the $t\bar{t} \rightarrow$ dilepton decay channel using the m_{T2}, $m_{\mathrm{T2}\perp}$ and $m_{\ell b}$ variables with ATLAS data

Phan Thi Hong Ngoc

A measurement of the top quark mass is studied in the $t\bar{t} \rightarrow$ dilepton decay channel. Three different variables: m_{T2}, $m_{\mathrm{T2}\perp}$ and $m_{\ell b}$ are used in this study. The m_{T2} and $m_{\mathrm{T2}\perp}$ are applied to solve the challenging of the production of two neutrinos in this decay channel while the $m_{\ell b}$ only focuses on the lepton-jet (ℓb) system.
The calibration curve method is applied in the mass measurement, using the ATLAS data of 4.7 fb^{-1} at $\sqrt{s}$ = 7 TeV collected in 2011. The purpose of the study is to reduce the uncertainty of the measurement. Two main analyses are presented. The baseline analysis corresponding to the standard selection measured the top quark mass with m_{top} = 173.6 ± 0.9 (stat.) ± 1.7 (syst.) GeV for m_{T2}, m_{top} = 173.8 ± 0.7 (stat.) ± 1.8 (syst.) GeV for $m_{\mathrm{T2}\perp}$ and m_{top} = 173.2 ± 0.8 (stat.) ± 1.5 (syst.) GeV for $m_{\ell b}$. The analysis with the optimisation selection in order to optimise the uncertainty of the measurement obtained the final results of m_{top} = 175.1 ± 0.9 (stat.) ± 1.6 (syst.) GeV for m_{T2}, m_{top} = 174.1 ± 0.8 (stat.) ± 1.4 (syst.) GeV for $m_{\mathrm{T2}\perp}$ and m_{top} = 174.1 ± 0.9 (stat.) ± 1.3 (syst.) GeV for $m_{\ell b}$. Among the three variables used, the $m_{\ell b}$ variable yields the result with the lowest uncertainty, which is consistent with a new ATLAS top-quark mass measurement in dileptonic decay channel released in 2013.

CERN-THESIS-2013-173
23/09/2013

Physikalisches Institut der
Universität Bonn
Nussallee 12
D-53115 Bonn

BONN-IB-2013-02
October 2013

Universität Bonn

Physikalisches Institut

Measurement of the top quark mass in the $t\bar{t} \rightarrow$ dilepton decay channel using the m_{T2}, $m_{\mathrm{T2}\perp}$ and $m_{\ell b}$ variables with ATLAS data

Phan Thi Hong Ngoc

Dieser Forschungsbericht wurde als Masterarbeit von der Mathematisch-Naturwissenschaftlichen Fakultät der Universität Bonn angenommen.

Angenommen am:	02.09.2013
1. Gutachter:	Prof. Dr. Norbert Wermes
2. Gutachter:	Prof. Dr. Klaus Desch

Acknowledgements

I wish to express my deepest gratitude to my supervisor Dr. Markus Cristinziani for his enthusiatic support and patience to help me finish my thesis. He gave me an opportunity and guided me to engage in a scientific research step by step.

I would like to acknowledge and show my gratitude to Prof. Dr. Norbert Wermes for his agreement to be the referent for my thesis and giving me the chance to study in his group. I would like to thank Prof. Dr. Klaus Desch for accepting to participate in my final examination.

I am much obliged to my Vietnamese government and the Mekong 1000 project for their financial support.

Moreover, I would like to give heartfelt thanks to all members in our group: Dr. Kirika Uchida, Dr. Tatevik Abajyan, Dr. Gia Khoriauli and Agnieszka Leyko for help, discussions and friendliness, especially to Kaven Yau Wong for his enthusiatic help during the year.

Finally, I would like to thank all members of my family for their understanding and encouragement as well as my Vietnamese and international friends in Bonn, who helped and encouraged me during the time I have been far away from home.

Contents

CHAPTER 1

Introduction

The top quark is the most massive elementary particle in the Standard Model of particle physics, which was predicted by Makoto Kobayashi and Toshihide Maskawa in 1973 to explain the observed CP violation in neutral kaon decays [1]. In 1995, the CDF [2] and D0 [3] collaboration discovered the existence of the top quark with a mass of around 176 GeV.

The top quark mass is an interesting parameter of the SM. It has a special role in electroweak symmetry breaking, linking to physics beyond the SM and limiting the allowed Higgs boson mass via radiative corrections [4]. The top quark decays before hadronisation and gives us access to a "bare quark" due to its short lifetime (5×10^{-25} s) [5]. Top quark events are background in many processes beyond the SM. It is produced in abundance at the Large Hadron Collider (LHC), which allows many precise measurements.

The top quark mass can be measured by several methods in different channels, which have their own advantages and disadvantages. A top mass of $m_{\text{top}} = 173.20 \pm 0.51$ (stat.) $\pm$ 0.71 (syst.) GeV using data luminosity up to 8.7 fb^{-1} [6] is the best result so far, reported by the Tevatron combination in 2013. The top quark mass has also been measured at the LHC by the CMS and ATLAS collaboration [7–10]. In the dilepton decay channel at LHC, the ATLAS collaboration using 4.7 fb^{-1} data measured top quark mass, giving a value of $m_{\text{top}} = 175.2 \pm 1.6$ (stat.) $\pm$ 2.98 (syst.) GeV [7] and a top mass $m_{\text{top}} = 172.5 \pm 0.43$ (stat.) $\pm$ 1.48 (syst.) GeV [9] was reported by the CMS collaboration.

This thesis focuses on studying the top quark mass in the $t\bar{t}$ →dilepton decay channel with the data collected by the ATLAS detector at the LHC. The main purpose of the analysis is to reduce the total uncertainty of the top quark mass measurement. The method applied in the study is the calibration curve method using three variables: the stranserve mass (m_{T2}) [11], the orthogonal decomposition of m_{T2} ($m_{\text{T2}\perp}$) [12] and the invariant mass of lepton and b-jet system ($m_{\ell b}$). In the $t\bar{t}$ dilepton decay channel, the final state is characterised by two leptons, two b-jets and missing transverse momentum due to the two neutrinos escaping the detector, which leads to a challenge to a top quark mass measurement in this channel. In order to circumvent this problem, m_{T2} and $m_{\text{T2}\perp}$variables are applied. The m_{T2} and $m_{\text{T2}\perp}$ variables are used in events with two invisible particles in the final state and represent a lower boundary for the parent particle mass, and can therefore be interesting to measure the top quark mass in the $t\bar{t}$ →dilepton decay channel. In addition, $m_{\ell b}$ variable is used to measure the top quark mass, where only lepton and b-jet system are considered.

The thesis is organised as follows:

- Chapter one introduces the top quark measurements in general and gives the outline of the thesis.

- Chapter two summarises some important theoretical views of the SM, the properties of top quark and the $t\bar{t}$ →dilepton decay channel. In addition, the definitions of the m_{T2}, $m_{\mathrm{T2}\perp}$ and $m_{\ell b}$ variables are presented in this chapter.
- Chapter three introduces the general descriptions of the LHC and the ATLAS detector.
- Chapter four describes the methodology of the analysis. The signal and background estimation are first presented, followed by a description of the data and Monte-Carlo (MC) samples used in the analysis. Then, the objects, event selections and optimisation cuts are given. The methodology of the study is discussed in the last section.
- Chapter five introduces the systematic sources that can affect the top mass measurement and describes the procedure to estimate systematic uncertainty in the analysis.
- Chapter six shows the results of the analysis. Control plots for each selection are presented, among other figures illustrating the application of the methodology described in former chapters. Lastly, the measurements of the top quark mass and its uncertainties are summarised.
- Chapter seven summarises and concludes some important points from the study.

In this work, the convention $\hbar = \mathrm{c} = 1$ is applied and valid for all formulas and distributions. Therfore, masses, energies and momenta are expressed in the unit of [eV].

CHAPTER 2

Theoretical aspects

This chapter contains a short introduction to the Standard Model (SM) of particle physics. In addition, the top quark and its decay production are discussed, followed by the definitions of the m_{T2}, $m_{\mathrm{T2}\perp}$ and $m_{\ell b}$ variables.

2.1 The Standard Model of particle physics

More detailed information of the SM can be found for instance in references [13–15]. This section only mentions the most significant parts of the SM relevant to the study.

The SM of particle physics describes the elementary particles and their fundamental interactions. The primary particles are the point-like components of matter with substructure limits of 10^{-18}–10^{-19}m. The basic building blocks of matter are known as matter particles, called fermions. The matter particles can interact by exchanging their corresponding mediators, called gauge bosons. The gauge bosons in the SM are classified in three groups, which correspond to three interactions: strong, weak and electromagnetic.

Although the SM is an incomplete theory of fundamental interactions due to the absence of the other fundamental interaction (gravity), it is considered as a very successful theory in particle physics.

2.1.1 Fermions

Fermions are matter particles with spin $\frac{1}{2}$ and classified in leptons and quarks. The SM has twelve elementary fermions, six quarks and six leptons (and their corresponding anti-particles), organised in pairs or generations. All stable matter in the universe are made from particles belonging to the first generation. Any heavier particle quickly decays into the next most stable level.

There are six types of quark flavours: up, down, strange, charm, bottom and top, paired in three generations (Table 2.1). Each generation includes one charge $+\frac{2}{3}$ particle and one particle with electrical charge $-\frac{1}{3}$. The up and down quarks have the lowest masses of all quarks and form the first generation. The charm and strange quarks constitute the second generation while the third generation includes the bottom and the top quarks. Every quark has its anti-particle, called anti-quark with the same mass but opposite charge.

The heavier quarks quickly decay into the lighter quarks. Therefore, the up and down quarks are generally stable and are the most common in the universe, whereas the strange, charm, top, and bottom quarks can only be produced in high energy collisions.

Table 2.1: The list of fermions in the SM [16].

Generation	Particle name	Symbol	Mass	Charge
Quarks				
I	up	u	2.3 MeV	$+\frac{2}{3}$
	down	d	4.8 MeV	$-\frac{1}{3}$
II	charm	c	1.275 GeV	$+\frac{2}{3}$
	strange	s	95 MeV	$-\frac{1}{3}$
III	top	t	173.07 GeV	$+\frac{2}{3}$
	bottom	b	4.18 GeV	$-\frac{1}{3}$
Leptons				
I	electron neutrino	ν_e	≈ 0 MeV	0
	electron	e	0.511 MeV	-1
II	muon neutrino	ν_μ	≈ 0 MeV	0
	muon	μ	105.7 MeV	-1
III	tau neutrino	ν_τ	≈ 0 MeV	0
	tau	τ	1.77 GeV	-1

The quarks carry colour charge, and interact via the strong interaction. They can not be directly observed in isolation due to the colour confinement. They also have electric charge and weak isospin; therefore, they interact with other fermions via both electromagnetic and weak interactions.

The six other fermions do not contain colour charge and are called leptons, which are similarly divided into three generations. Each generation consists of a negatively charged lepton, and its corresponding electrically neutral neutrino. The first generation is comprised by the electron and the electron neutrino, while the muon, muon neutrino, tau and tau neutrino are arranged in the second and the third generations, respectively. The electron, muon and tau have sizeable masses, whereas the neutrinos are nearly massless and do not decay. Because the electron has the lightest mass of all the charged leptons, it is the stable and most common fermion in the universe.

Similarly to quarks, each lepton has a corresponding type of antiparticle, known as anti-lepton. The leptons do not participate in the strong interaction, but are subject to the other fundamental interactions, except for lepton neutrinos only taking part in weak interaction. All leptons exist as free particles. The summary of leptons is shown in the bottom part of Table 2.1.

2.1.2 Gauge bosons

The exchange of force-carrying particles results in the three fundamental forces in the SM. Gauge bosons with integer spin are mediators, transferring discrete amounts of energy between fermions. Each fundamental interaction corresponds to its associated gauge bosons, as shown in the Table 2.2.

The electromagnetic force is responsible for practically all the phenomena outside the nucleus, except

Table 2.2: The list of gauge bosons in the SM [16].

Interaction	Particle name	Symbol	Mass	Charge
Electromagnetic	Photon	γ	0 MeV	0
Weak	W^+ boson	W^+	80.4 GeV	+1
	W^- boson	W^-	80.4 GeV	-1
	Z^0 boson	Z^0	91.2 GeV	0
Strong	Gluons (8 types)	g	0 MeV	0

for gravity, and is carried by the photon. The electromagnetic interactions act on all particles carrying charge, for example electron–electron scattering (Figure 2.1a). This force holds electrons inside atoms and around the nucleus.

The weak interaction is responsible for the existence and structure of the atomic nuclei, the radioactive decay of particles and the nuclear fusion. In the SM, this interaction involves the exchange of the intermediate gauge bosons, the W and the Z bosons. The weak force has the noticeable role in the quarks transmutation involved in many decays of nuclear particles. The existence of the weak interaction is revealed through radioactive decay, like the beta decay (Figure 2.1b). The weak interaction is the only process where a quark can change to another quark, or a lepton to another lepton, known as "flavour changes".

The strong interaction is one of the three fundamental interactions of the SM, which binds nucleons together to form the nucleus of an atom and holds the quarks constituting a nucleon together. The strong interaction between quarks is mediated by gluons (Figure 2.1c). Gluons, in turn, can interact among themselves because of their effective colour charge, described by the theory of the quantum chromodynamics (QCD).

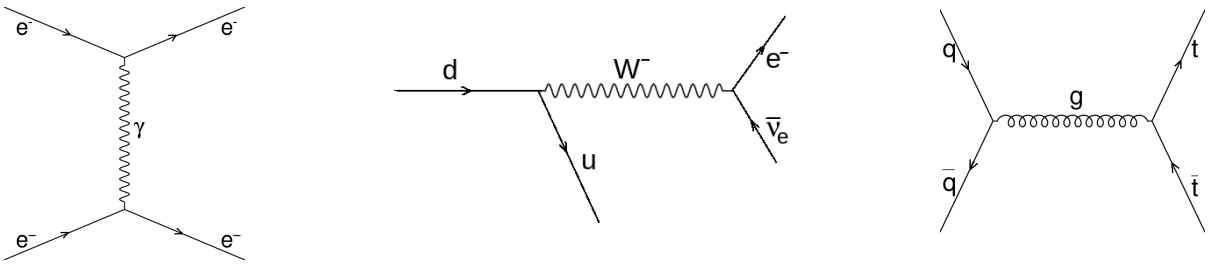

(a) (b) (c)

Figure 2.1: Examples of three fundamental interactions in the SM. (a): electron-electron scattering, (b): beta decay and (c): quark-quark annihilation.

From the theoretical point of view, the SM is a quantum field theory based on the local gauge symmetry group $SU(3)_C \times SU(2)_L \times U(1)_Y$. The $SU(3)_C$ symmetry group or QCD identifies the strong interactions, whereas the unified group of electroweak forces is the $SU(2)_L \times U(1)_Y$ group.

Among the gauge bosons of the SM, the photon and gluons are massless, in contract to the massive W and Z bosons, which points that the electroweak symmetry group is not a symmetry of the vacuum.

The so-called Higgs mechanism is introduced as a spontaneous symmetry breaking term [17, 18] that breaks the SM group $SU(3)_C \times SU(2)_L \times U(1)_Y$ into $SU(3)_C \times U(1)_{em}$. This results in the massive W and Z bosons as well as a scalar field with its associated particle: the Higgs boson with spin zero and mass of around 126 GeV[1], which is probably the remaining particle that would complete the SM theory.

2.2 The top quark in the Standard Model

A more detailed review of the top quark physics can be found in [19, 20], the following section summarises the most important aspects of the top quark.

As discussed in the previous section, the top quark (t) is an elementary particle and one of the fundamental constituents of matter. It is the most massive fermion in the SM with spin $\frac{1}{2}$, and the weak-isospin partner to the b-quark, together constituting the third generation of quarks. The top quark experiences all fundamental interactions in the SM. It has an electric charge of $+\frac{2}{3}$ and an expected Yukawa coupling $y_t \approx 1$.

2.2.1 Motivation for top quark mass measurements

The top quark mass is an fundamental parameter of the SM and contributes significantly to the electroweak radiative corrections. The accurate measurements of the top quark mass are indispensable tasks for precision tests of the stability of the SM [21]. Together with the W boson mass, it is a crucial input to global electroweak fits, providing a constraint on the Higgs boson mass as well as potentially discovering physics beyond the Standard Model [22]. Figure 2.2 shows the constraint from the W boson mass and top mass on the Higgs boson mass and a global constraint originating from different electroweak observables.

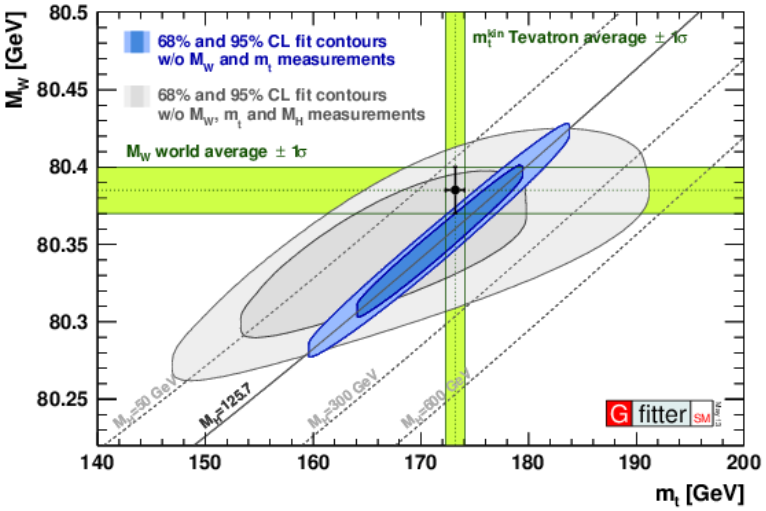

Figure 2.2: Constraints from m_W and m_{top} measurements on m_H within the SM. The confidence level (CL) contours are given from scan of fixed m_W and m_{top}. The green bands point the $\pm 1\sigma$ region of the direct m_W and m_{top} measurements. The blue area with 68% CL shows the fit results without m_W and m_{top} measurements and m_W, m_{top} and m_H measurements are excluded from the 95% CL contour (grey colour) [22]

[1] On July 4, 2012, CERN announced the discovery of a new subatomic particle that's consistent with the Higgs boson, a particle that's been searched for since the 1970s, http://home.web.cern.ch/about/physics/search-higgs-boson

2.2.2 Top quark productions and decays

The top quark can be produced singly or in pairs in hadron collisions where the pair productions are mainly dominant via the strong interactions. The $t\bar{t}$ production in the gluon fusion and quark-antiquark ($q\bar{q}$) annihilation processes are given in Figure 2.3. At the LHC, the gluon fusion channel is more dominated (90%) while the $q\bar{q}$ annihilation has a smaller contribution (10%).

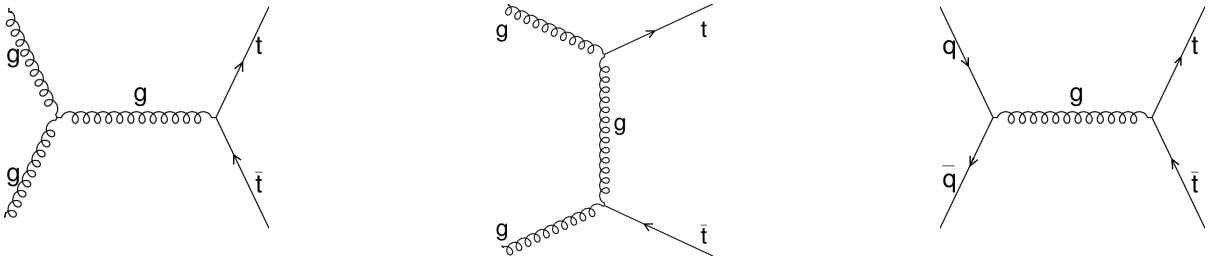

Figure 2.3: Leading-order Feynman diagrams for the top pair production. (a & b): gluon fusion processes and (c):quark-antiquark annihilation process

After production, the top quark mostly decays into a W boson and a bottom quark through the weak interaction, with the fraction determined by the near unity value of the Cabibbo-Kobayashi-Maskawa (CKM) quark mixing matrix element $|V_{\mathrm{tb}}(\approx 0.9992)|$ [16]. The bottom quark then hadronises and forms a b-jet while the W boson can decay hadronically (BR[2] of 68%) or leptonically into electron (e), muon (μ) or tau (τ) (BR of 32%) [16]. Hence, a $t\bar{t}$ pair decays into different channels, based on the W boson decay modes: dileptonic, lepton + jets and full hadronic decay channels.

Note that the leptonic decay mode of the W boson can occur in the three final states: $e\nu_e$, $\mu\nu_\mu$ or $\tau\nu_\tau$. If electron or muons in the final state of the $t\bar{t}$ events are come from the W boson decay, it leads to the final signature with two jets, two leptons, and missing transverse momentum[3]. On the contrary, if the W boson decays into a τ lepton, the situation is different. The τ, in turn, can decay into a electron or muon (BR of 35%) that contributes to the leptonic category or into hadrons (BR of 65%), classified to the lepton + jets or all hadronic categories of the $t\bar{t}$ event. Therefore, one has no chance to recognise if the electron or muon in the final state of the $t\bar{t}$ process results from the direct W boson decay or not.

To summarise, in the final state of a $t\bar{t}$ event, the charged lepton can be electrons or muons and the quark (q) represents a first or second generation of the quarks.

The mass of the top quark has been measured in separate channels. Different channels and measurements can be combined together to improve the precision. Some measurement results of the top quark mass from various experiments are displayed in Table 2.3.

2.2.3 The dilepton decay channel

The dilepton decay channel has the smallest branching fraction in all $t\bar{t}$ decay channels. However, this channel has a very clear and distinctive signature in the detector, only diluted by the missing transverse energy attributed to two undetected particles, neutrinos. In addition, the background of this process from gluon-multijet production in the event is small, leading to a snaller effect of the systematic uncertainty

[2] BR: Branching ratio
[3] Defined in Appendix A

Table 2.3: Top quark mass results at different measurements

Measurement	Channel	Luminosity (fb^{-1})	Mass result (GeV)	Uncertainty (GeV)	
				Statistical	Systematic
ATLAS 2011 [7]	dilepton	4.7	175.2	1.6	2.98
ATLAS 2011 [8]	lepton + jets	4.7	172.31	0.75	1.35
ATLAS 2011 [23]	all jets	2.04	174.9	2.1	3.8
CMS 2011 [9]	dilepton	5.0	172.5	0.43	1.48
CDF [24]	dilepton	5.6	170.28	1.95	3.09
D0 [25]	dilepton	5.3	174.0	2.36	1.44
Tevatron Combination [6]	combination	8.7	173.2	0.51	0.71

related to jets such as jet calibration on the measurement. In the dilepton decay channel, each top quark decays into a W boson and a bottom quark. The W bosons in both decay branches, in turn, produce two leptons and two lepton neutrinos in the final state.

Depending on the final state of the events, the dilepton decay channels can be classified into three subgroups, given by Table 2.4 [26]. The e^+e^- and $\mu^+\mu^-$ decay mode in the $t\bar{t} \to b\ell^+\nu\bar{b}\ell^-\bar{\nu}$ event shares the same relative abundance value of around 1.8% while the BR of the $e^\pm\mu^\mp$ mode is around 3.6%.

Table 2.4: Top dilepton channel decay modes

Decay mode	Symbol	Final state
electron-electron	e^+e^-	two electrons, two jets, missing transverse momentum
electron-muon	$e^\pm\mu^\mp$	one electron, on muon, two jets, missing transverse momentum
muon-muon	$\mu^+\mu^-$	two muons, two jets, missing transverse momentum

Some processes mimic the dilepton decay channel with the same final state. The dominant process is the single top quark production through the Wt-channel, followed by the Z + jets processes and the diboson production. The fake leptons similarly contribute to the background of the $t\bar{t}$ →dilepton decay events. The background of the dilepton decay channel will be discussed in more detail in Chapter 4.

2.3 Definitions of the m_{T2}, $m_{\mathrm{T2}\perp}$ and $m_{\ell b}$ variables

In a two-body decay, the relationship between the momenta of both children particles in the parent rest frame and the mass of the parent particles is straightforward. However, it is more complicated in a

three-body decay like the $t \to b\ell\nu$ decay because of the kinematic boundary of the phase space of the children [27].

A top quark mass measurement can be done with the $t\bar{t} \to b\ell^+\nu\bar{b}\ell^-\bar{\nu}$ process, accompanied by two charged lepton leaving a clear signature and a significant amount of missing transverse energy. It has a low background because of very few jets in the process. However, this process also get some noticeable challenges. The transverse momentum of the $t\bar{t}$ system is different from event to event. Moreover, the missing transverse momentum in the final state consists of two transverse momenta of two invisible particles, the lepton neutrinos. These problems can be circumvented by using the kinematic variable m_{T2} and its orthogonal decomposition, called $m_{\mathrm{T2}\perp}$.

Three variables m_{T2}, $m_{\mathrm{T2}\perp}$ and $m_{\ell b}$ used in this study are discussed in the following subsections.

2.3.1 The m_{T2} variable

The stransverse momentum m_{T2} variable is a kinematic variable, initially introduced to measure the mass of a massive particle in pair production events decaying into two invisible particles in the final state. This variable also represents a lower boundary of the mass of the parent particle. Therefore, the m_{T2} variable is suitable for measuring the top quark mass in the $t\bar{t}$ →dilepton decay process in this study.

A first use of this variable for measuring the top quark mass in ATLAS was reported in reference [7], in summer 2012. More detailed information about the m_{T2} variable is found in [28–33]. This part only shows the definition of the m_{T2} variable in the $t\bar{t}$ →dilepton decay channel.

In order to calculate m_{T2} the transverse mass m_{T} of a top quark in the decay $t \to b\ell\nu$ is first considered by the following formula:

$$m_{\mathrm{T}}(m_\nu, \vec{p}_{\mathrm{T}}^{\,\nu}) = \sqrt{m_{\ell b}^2 + m_\nu^2 + 2(E_{\mathrm{T}}^{\ell b} E_{\mathrm{T}}^{\nu} - \vec{p}_{\mathrm{T}}^{\,\ell b} \cdot \vec{p}_{\mathrm{T}}^{\,\nu})} \simeq \sqrt{m_{\ell b}^2 + 2(E_{\mathrm{T}}^{\ell b}|p_{\mathrm{T}}^{\nu}| - \vec{p}_{\mathrm{T}}^{\,\ell b} \cdot \vec{p}_{\mathrm{T}}^{\,\nu})} \tag{2.1}$$

where:

- "ℓb" means the lepton–b-jet system, denoted as the visible particles group. $m_{\ell b}$, $E_{\mathrm{T}}^{\ell b}$ and $\vec{p}_{\mathrm{T}}^{\,\ell b}$ are the invariant mass, transverse energy and transverse momentum of ℓb system, all defined in Appendix A.
- the $m_\nu \approx 0$, E_{T}^{ν} and $\vec{p}_{\mathrm{T}}^{\,\nu} = p_{\mathrm{T}}^{\mathrm{miss}}$ are the mass, transverse energy and transverse momentum of the neutrino, denoted as the invisible particle. $|\vec{p}_{\mathrm{T}}^{\,\nu}| \approx E_{\mathrm{T}}^{\nu}$ due to $m_\nu \approx 0$.

Let us consider a $t\bar{t}$ pair decay: $t\bar{t} \to b\ell^+\nu\bar{b}\ell^-\bar{\nu}$

There are two transverse masses ($m_{\mathrm{T}}^{(1)}$and $m_{\mathrm{T}}^{(2)}$) in the $t\bar{t}$ decay system. If the two missing transverse momenta of the $t\bar{t}$ decay were measured separately and $b\ell\nu$ could be assigned correctly to t and $\bar{t}$, m_{T} could be determined for each of the twin decay chains and $\max(m_{\mathrm{T}}^{(1)}, m_{\mathrm{T}}^{(2)}) \leqslant m_{\mathrm{top}}$ then infers the top mass. However, the two missing momenta can not be measured independently in practice. The missing transverse momentum[4] in the final state is the combination of two transverse momenta of two neutrinos in both decay branches, as shown in Eq.(2.2).

$$\vec{p}_{\mathrm{T}}^{\,\nu(1)} + \vec{p}_{\mathrm{T}}^{\,\nu(2)} = \vec{p}_{\mathrm{T}}^{\,\mathrm{miss}} \tag{2.2}$$

Hence, all the possibilities of $\vec{p}_{\mathrm{T}}^{\,miss}$ dividing into two assumed components $\vec{p}_{\mathrm{T}}^{\,\nu(1)}$ and $\vec{p}_{\mathrm{T}}^{\,\nu(2)}$ have to be considered, taking into account the coherence of the observed kinematics of the events [27]. Following this discussion of the m_{T} concept, the m_{T2} variable is then defined by the formula [30–32]:

[4] Defined in Appendix A

$$m_{T2} = \min[\max[m_T(m_\nu, \vec{p}_T^{\nu(1)}), m_T(m_\nu, \vec{p}_T^{\nu(2)})]] \tag{2.3}$$

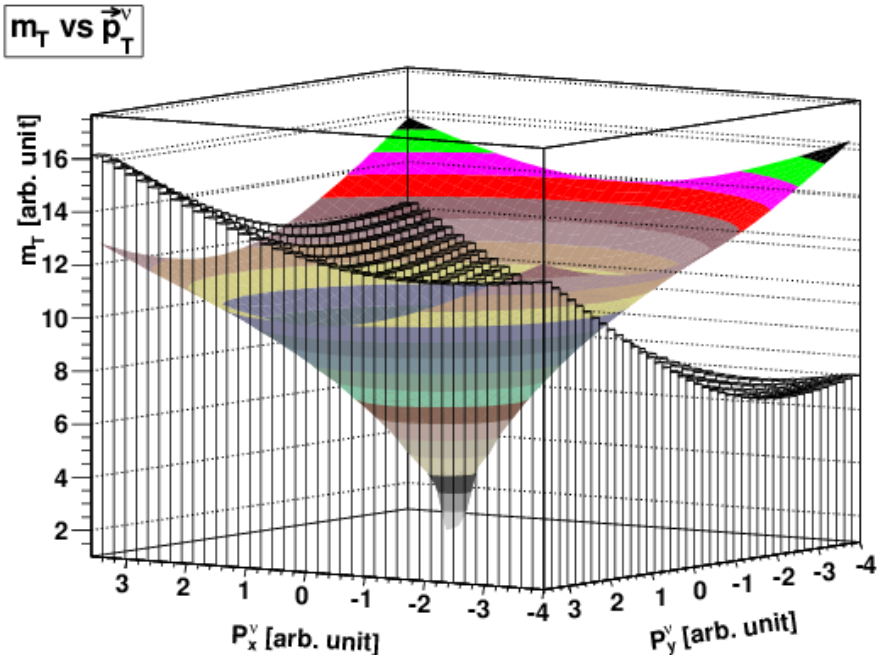

Figure 2.4: m_T distributions by one scanned neutrino transverse momentum [26].

In Eq.(2.3), the m_{T2} is the minimum value of the surface that collects all of the points with highest values between two m_T distributions. The neutrinos' momenta are scanned to determine the m_T distributions. Figure 2.4 shows an example of two m_T distributions depending on the two dimensions of the transverse momentum of one neutrino, for instance $\vec{p}_T^{\nu(1)}$.

Note that $\vec{p}_T^{\nu(1)}$ and $\vec{p}_T^{\nu(2)}$ are related; therefore, the m_T values defined by Eq.(2.1) can be expressed as a function of $\vec{p}_T^{\nu(1)}$ or $\vec{p}_T^{\nu(2)}$.

2.3.2 The $m_{T2\perp}$ variable

The definition of the $m_{T2\perp}$ variable is discussed in more detail in references [12], [27], [28]. The $m_{T2\perp}$ variable is the orthogonal dimensional decomposition of the m_{T2} value on the direction defined by the upstream transverse momentum vector $\vec{U}_T$. Unlike m_{T2}, this variable is invariant under $\vec{U}_T$ boosts of the underlying the $t\bar{t}$ system [27]. The upstream transverse momentum is defined as follows.

$$\vec{U}_T = -(\vec{p}_T^{visible} + \vec{p}_T^{invisible}) = -(\vec{p}_T^{\ell b} + \vec{p}_T^{miss}) \tag{2.4}$$

The structure defining the $m_{T2\perp}$ variable is similar to the the m_{T2} observable in Eq.(2.3), with exception that all the $\vec{p}_T$ vectors appearing explicitly and implicitly are replaced by $\vec{p}_{T\perp}$. The definitions of perpendicular transverse momentum $\vec{p}_{T\perp}$ perpendicular transverse mass $m_{T\perp}$ and $m_{T2\perp}$ values are given in the following formulas.

$$\vec{p}_{T\perp} = \frac{1}{U_T^2}.\vec{U}_T \times (\vec{p}_T \times \vec{U}_T) \tag{2.5}$$

$$m_{\mathrm{T}\perp}(m_\nu, \vec{p}^{\,\nu}_{\mathrm{T}\perp}) \simeq \sqrt{m^2_{\ell b} + 2(E^{\ell b}_{\mathrm{T}\perp}|\vec{p}^{\,\nu}_{\mathrm{T}\perp}| - \vec{p}^{\,\ell b}_{\mathrm{T}}.\vec{p}^{\,\nu}_{\mathrm{T}\perp})} \tag{2.6}$$

$$m_{\mathrm{T2}\perp} = \min[\max[m_{\mathrm{T}\perp}(m_\nu, \vec{p}^{\,\nu(1)}_{\mathrm{T}\perp}), m_{\mathrm{T}\perp}(m_\nu, \vec{p}^{\,\nu(2)}_{\mathrm{T}\perp})]] \tag{2.7}$$

where: $E^{\ell b}_{\mathrm{T}\perp}$, $\vec{p}^{\,\ell b\perp}_{\mathrm{T}}$ and $E^{\nu}_{\mathrm{T}\perp} \simeq |\vec{p}^{\,\nu}_{\mathrm{T}\perp}|$ are the perpendicular transverse energy and the perpendicular transverse momentum of the ℓb system and a neutrino.

One consideration is that there are two combinations between leptons and b-jets; therefore, the m_{T2} and $m_{\mathrm{T2}\perp}$ values are calculated for all possibilities of the combinations and the smallest value is taken as the final m_{T2} and $m_{\mathrm{T2}\perp}$.

2.3.3 The $m_{\ell b}$ variable

The $m_{\ell b}$ value is the invariant mass of the lepton–b-jet system, defined by the formula:

$$m_{\ell b} = \sqrt{m^2_\ell + m^2_b + 2(E_\ell E_b - \vec{p}_\ell.\vec{p}_b)} \tag{2.8}$$

In a $t\bar{t} \to b\ell^+\nu\bar{b}\ell^-\bar{\nu}$ event, two values of $m_{\ell b}$ can be computed, one for each decay chain. However, four invariant masses of ℓb pairs can be calculated in practice because there is no knowledge of the association of the leptons and b-jets. Therefore, a value of the $m_{\ell b}$ variable in every combination is determined by the average of the two invariant masses. This study considers the lower value of the average invariant mass of ℓb systems of each combination as the $m_{\ell b}$ study variable for each event because more ℓb correct combinations are expected to be associated with the lower $m_{\ell b}$ values.

CHAPTER 3

Experimental aspects

3.1 The Large Hadron Collider

The Large Hadron Collider (LHC) [34–36] is the biggest and most powerful circular accelerator for particle physics research aiming to explore the validity and limitations of the Standard Model. It is located at CERN (European Organization for Nuclear Research) in the border between France and Switzerland. The LHC is composed of a 27 km circumference of superconducting magnets with accelerating structures to perform proton-proton and heavy ion collisions.

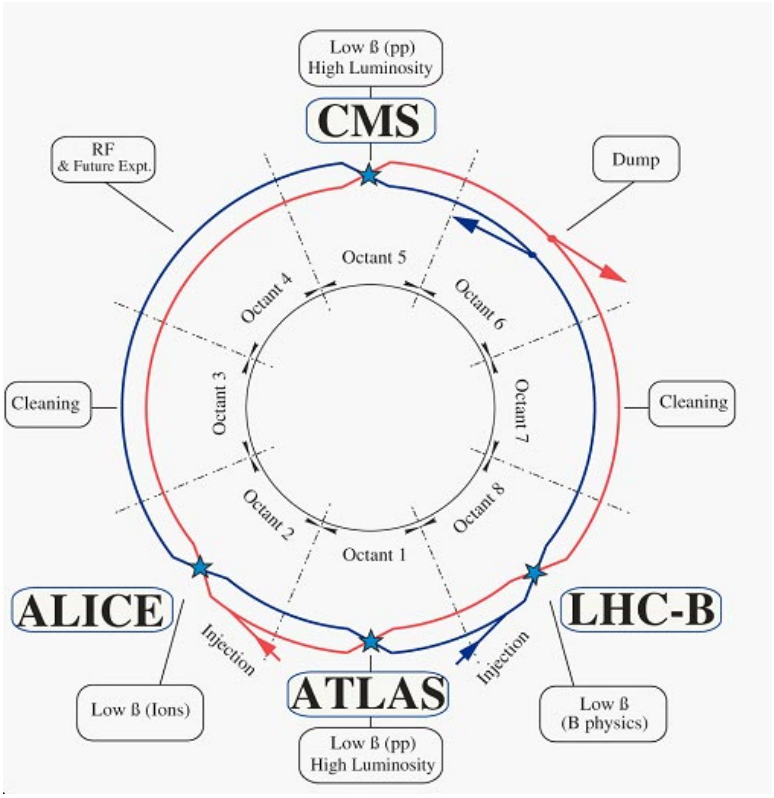

Figure 3.1: Scheme of the four main experiments and two ring structures of the LHC [34]

As a proton–proton collider, the LHC is designed to run at a centre-of-mass energy of 14 TeV and the admirable luminosity of $10^{34}\,\mathrm{cm}^{-2}\mathrm{s}^{-1}$. However, the LHC has run at half its designed beam energy so far with a total of 7 TeV center of mass energy. It accelerates two proton beams in two opposite directions in the accelerator ring up to the record energy of 3.5 TeV. The opposite proton beams then collide at four locations corresponding to four experiments: ALICE, ATLAS, CMS and LHCb (Figure 3.1).

ATLAS (A Toroidal LHC Apparatus) [37] and CMS (Compact Muon Solenoid) [38] are general purpose detectors for particle physics. They are designed to study a large range of particles and phenomena, from measuring precisely the properties of previously discovered particles and phenomena produced in LHC interactions to exploring new physics such as the search of Higgs boson, extra dimensions and dark matter. In contrast, ALICE (A Large Ion Collider Experiment) [39] and LHCb (LHC-beauty) [40] do more specific researches, with ALICE optimized to detect heavy ions and LHCb studying the parameters of CP violation in B hadrons decays.

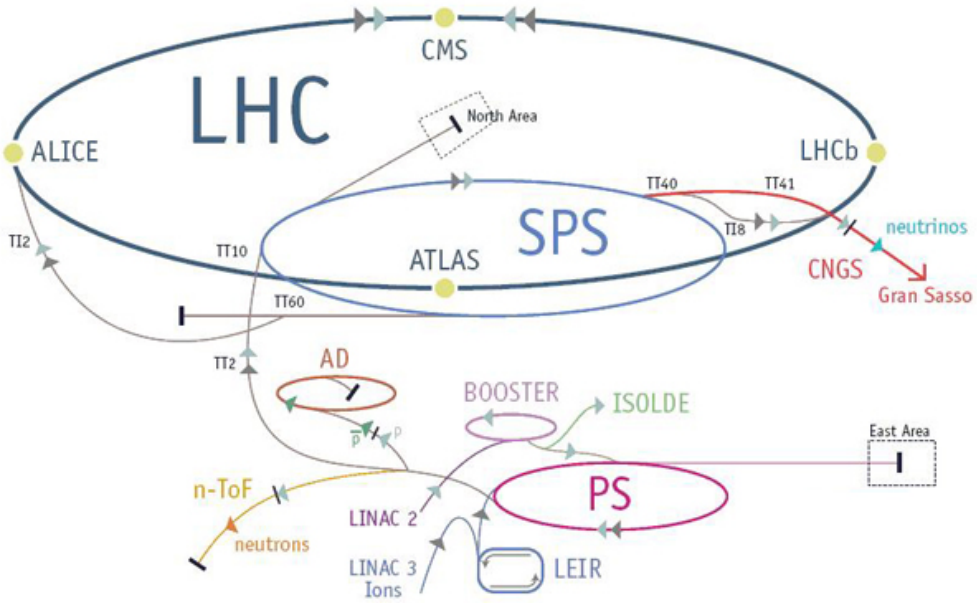

Figure 3.2: Overview of CERN's accelerator layout complex [34]

The acceleration of protons in the accelerator complex at CERN is sketched in Figure 3.2 [41]. The summary of this procedure is as follows [34].

- The protons splitting from hydrogen atoms are first accelerated up to the energy of 50 MeV at the Linear Accelerator 2 (Linac2) before being injected into the PS Booster (PSB) to attain an acceleration energy 1.4 GeV.
- The Proton Synchrotron (PS) continues to do the accelerating process of protons reaching to 25 GeV in the next step, followed by the 450 GeV energy of accelerated protons in the Super Proton Synchrotron (SPS).
- Finally, the protons move into the LHC ring where the radio frequency (RF) cavities accelerate them for 20 times of the last energy, corresponding to the nominal energy of 7 TeV. The proton beams arriving at the LHC ring in bunches will go around inside the LHC beam pipes under normal operating conditions.

One consideration is that the maximum energy of the beams is limited by the about 8.3 Tesla magnetic field. This field bends the orbit of the protons inside the circle by about 14 m dipole magnets, located in an almost continuous line along the ring. There is only small interruptions in the magnet chain for acceleration cavities or detectors.

3.2 The ATLAS detector

The ATLAS detector is a big instrument with 44 m length, 25 m diameter and about 7000 tons weight covering almost the full solid angle. It is designed to accommodate a large range of particle physics studies, measuring known objects, for instance, heavy quarks and gauge bosons with a high accuracy as well as discovering new physics like Higgs bosons or super-symmetric particles [37], [42], [43].

The ATLAS coordinate system is a right-handed system where the x axis directs to the centre of LHC circle, the y axis points upward and the z axis goes along the beam pipe. The x-y plane is the transverse plane and the distance from this plane to z axis is called as r. From the nominal interaction point, the polar angle θ is the angle respected to the beam axis and an angle identified around the beam direction is called the azimuthal angle φ. The pseudo-rapidity is defined by the formula $\eta = -\ln(\tan(\frac{\theta}{2}))$ and $\Delta R = \sqrt{\Delta\eta^2 + \Delta\varphi^2}$ denotes the distance between two physics objects in $\eta - \varphi$ space [43].

The ATLAS detector is a combination of many detector components (Figure 3.3), divided into three main groups: the inner detector, a pair of calorimeters to measure particle energies (electromagnetic and hadronic calorimeters) and the muon spectrometer.

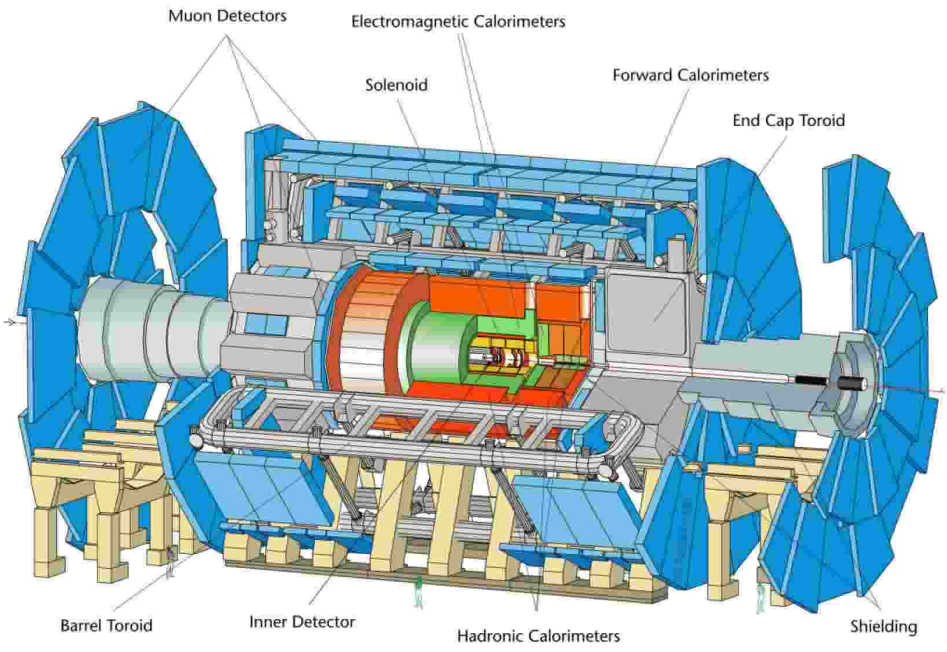

Figure 3.3: Overall layout of the ATLAS Detector [37]

3.2.1 The Inner Detector

The Inner Detector (ID) is the ATLAS central tracker that the momentum of charged particles can be measured from the tracks recorded. It is placed in the 2T magnetic field produced by the central solenoid. The ID size is about 6 m length and 2 m diameter and covers a pseudo-rapidity of $|\eta| \leqslant 2.5$. It comprises the pixel detector, the semiconductor tracker and the transition radiation detector, where each consists of a barrel part and end-caps. Figure 3.4 gives the overview of the ATLAS ID and the spatial layout of the ID barrel is shown in Figure 3.5.

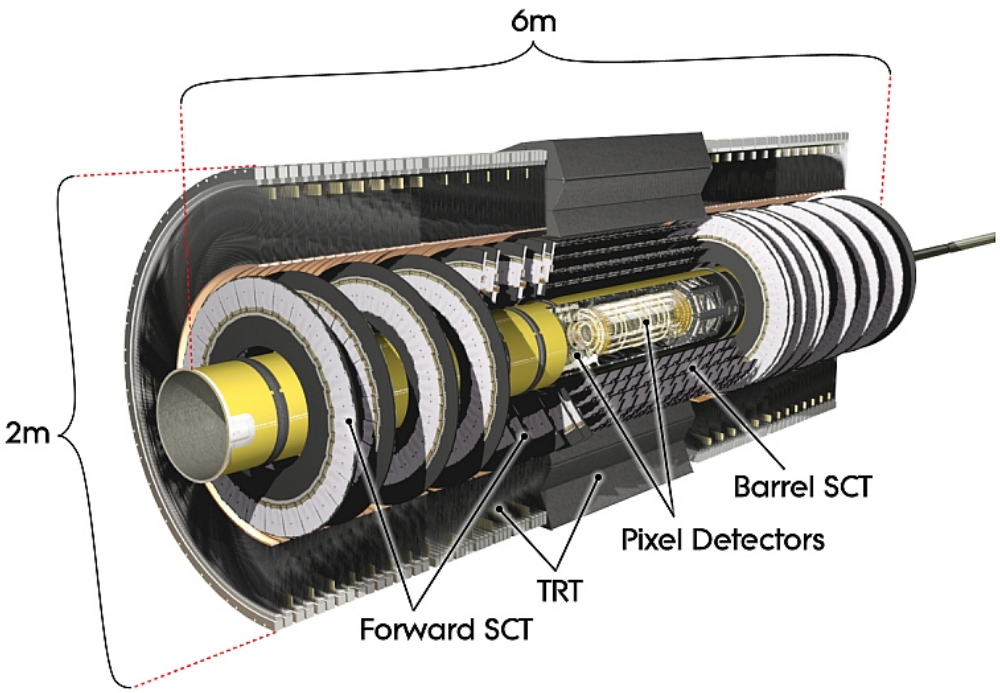

Figure 3.4: Overview of the ATLAS ID [44]

The Pixel Detector [45] is a silicon pixel detector and the innermost component. It plays a major role in the precision measurements of the trajectories of charged particles as close to the interaction point as possible. This system is composed of three cylindrical barrels and five disks on each side covering completely the angle of $|\eta| \leqslant 2.5$. It is able to serve the signals with over 80 million pixels, equipped by theirs own electronic circuits. The system can help to reconstruct the primary interaction point and the secondary vertices.

The semiconductor tracker (SCT) is located in the intermediate radial range with eight silicon micro-strip sensor layers. It helps to measure the particle momentum, impact parameters and vertex position as well as providing a good model recognition with its high granularity. The SCT system contains silicon detectors of 61 m^2 area with 6.2 million readout channels. The intrinsic accuracy of the SCT is 16 μm in r-φ space and 580 μm in the beam direction, which can distinguish the tracks separated by more than approximately 200 μm. Both the SCT and the Pixel detector have to be designed with low coefficient thermal expansion materials.

The transition radiation tracker (TRT) is the last part comprising the inner detector of ATLAS. It

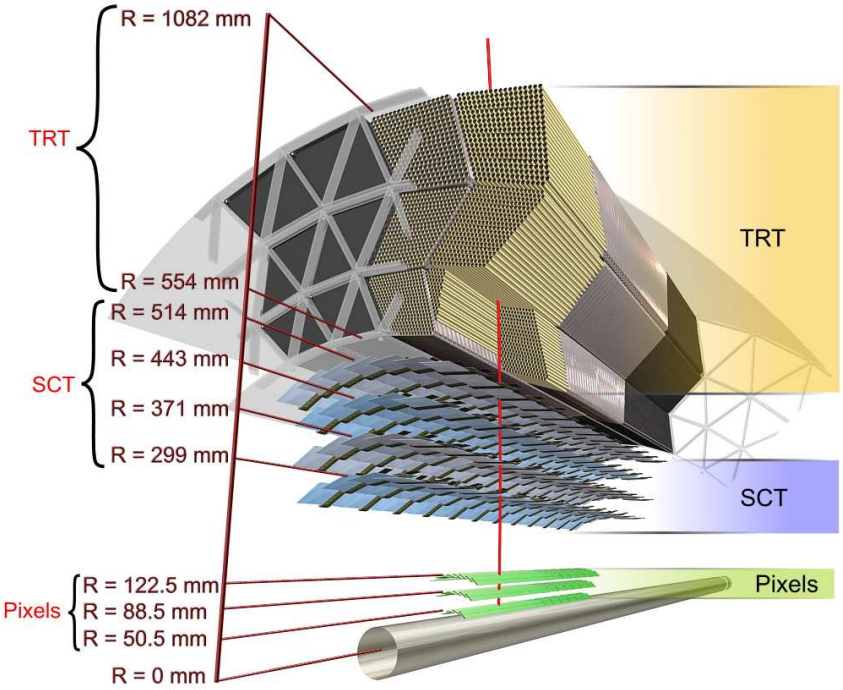

Figure 3.5: Three dimensional overview of the ATLAS ID barrel [43]

is covered by 4 mm diameter straw tubes in the gas volumes with the mixture of xenon, carbon dioxide, and carbon fluoride. Straws are equipped by the gold-plated wires which obtain a fast response and good properties of mechanics and electrics. The TRT provides typically 36 hits per track in $|\eta| \leqslant 2.0$ and can read out approximately 420000 electronic channels. With its high hit rates, it contributes to electron identification. Furthermore, it provides the discrimination between electrons and hadrons such as pions.

3.2.2 Calorimeters

The ATLAS calorimeters measure the energy of charged and neutral particles with energies up to some TeV, with high resolution and linearity. The calorimetry is grouped into two main components: the electromagnetic calorimeter and the hadronic calorimeter. Calorimeters cover a wide pseudo-rapidity scale of $|\eta| \leqslant 4.9$, which can precisely measure the missing transverse energy. The calorimeters have to give a good containment for electromagnetic and hadronic showers to eliminate punch-throughs into the muon system. An overview of the ATLAS calorimeters ia shown in Figure 3.6.

The electromagnetic (EM) calorimeter is the inner layer of the calorimeters, including a pre-sampler detector and a lead–liquid-argon (LAr) detector using lead as absorber material and liquid Argon (LAr) as active material. It measures the energies of photons and electrons by the electromagnetic showers with a cluster-based algorithm.

The EM calorimeter consists of a barrel with $|\eta| \leqslant 1.475$ and two end-caps with $1.375 < |\eta| < 3.2$. The barrel includes two identical half-barrels separated by a small gap of 6 mm. The end-caps are splitted into two coaxial wheels at $|\eta| = 2.5$.

The accordion-shaped Kapton electrodes and lead plates mechanically give the full coverage of the EM calorimeter; therefore, the EM calorimeter is also called a lead LAr detector.

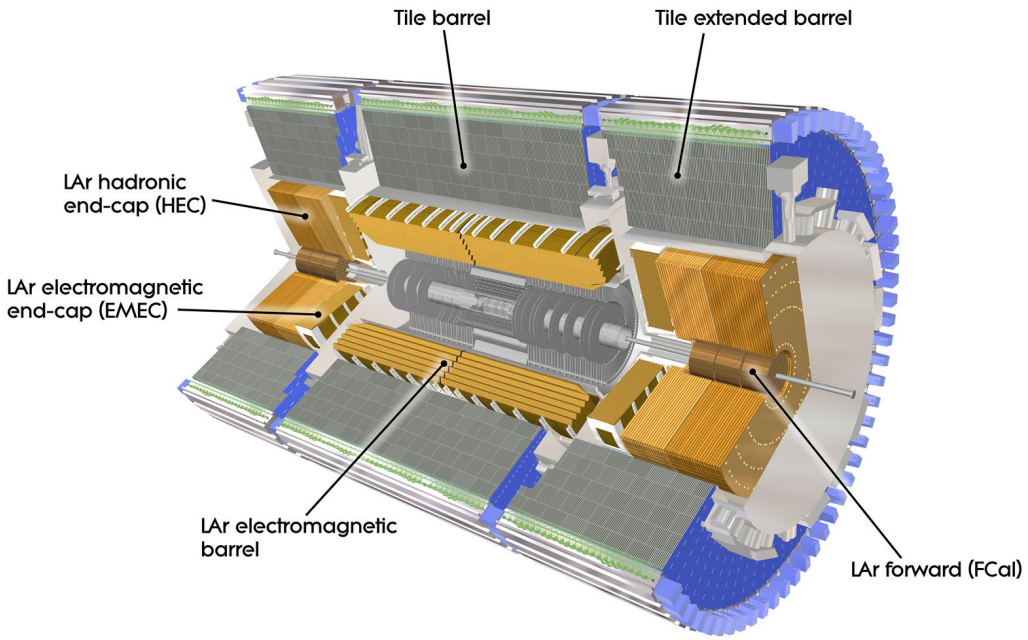

Figure 3.6: Three dimensional overview of the ATLAS calorimeter [44]

Moreover, the barrel and outer wheel of the EM calorimeter are segmented into three sections in longitudinal direction, while the inner wheel is separated in two sections. The thickness of the EM calorimeter is larger than 22 radiation lengths for the barrel and more than 24 radiation lengths for the end-caps.

The signals collected from the EM calorimeter are at the inner and outer faces of the detector. The region $1.37 < |\eta| < 1.52$ is not used for the measurements due to the large amount of material located in front of the EM calorimeter.

The hadronic calorimeter produces and records the tracks and energy of hadron particles such as protons, neutrons and mesons. It is the outer layer of the calorimeters and covers the range of $|\eta| < 4.9$. The operation principle of the hadronic calorimeter is the same as the EM calorimeter that detects the light from the particle shower and measure the energy of the original hadron. However, the average nuclear interaction length determining the longitudinal development is much larger than the radiation length. Therefore, the hadronic calorimeter is much bigger than its EM counterpart. It also needs to be dense and thick enough to guarantee that hadrons are absorbed completely.

There are three main components to form the ATLAS hadronic calorimeter: the tile calorimeter, the hadron end-cap calorimeter, and the forward calorimeter.

The scintillation tile calorimeter is used to detect the shower particles in the barrel region. It is subdivided into two parts with a barrel in the pseudo-rapidity range of $|\eta| < 1.0$ and two extended barrels in the $0.8 < |\eta| < 1.7$ region.

The hadron end-cap calorimeter is directly placed behind the EM calorimeter end-caps in the beam axis. It covers the pseudo-rapidity in the scale of $1.5 < |\eta| < 3.2$ with two independent wheels per end-cap. The wheels are made of copper plates with different sizes and includes 32 identical modules.

The forward calorimeter is the remaining section of the hadronic calorimeter, occupying the pseudo-rapidity range of $3.1 < |\eta| < 4.9$. It is located inside the hadron end-cap calorimeter. The forward

calorimeter is composed of three modules: one of them using copper as an absorber is expected for electromagnetic measurements, while the others made of tungsten measure most of the hadronic showers.

3.2.3 Muon spectrometer

The muon spectrometer system [46] is the outermost layer of the ATLAS detector. It is designed to detect and reconstruct muons escaping the calorimeter system by using a magnetic field.

The muon spectrometer consists of high precision tracking chambers with $|\eta| < 2.7$ and includes trigger chambers in the range of $|\eta| < 2.4$. The magnetic field bending muon tracks in the $|\eta| < 1.0$ region is provided by the big barrel toroidal magnet while the end-cap magnet creates the magnetic field in the region of $1.4 < |\eta| < 2.7$. The magnetic field in the $1.0 < |\eta| < 1.4$ area is combined of the magnetic field from both barrel toroidal and end-cap magnets.

The muon spectrometer system is a compound of different elements with two technologies employed. The momentum measurements are fulfilled by the field of barrel toroid and end-cap toroid systems. The Resistive-Plate Chambers (RPCs) and Thin-Gap Chambers (TGCs) are used in the barrel and end-caps respectively for triggering. The Monitored Drift Tubes (MDT) are generally utilised in the high precision chambers, with the exception of the innermost section of the end-cap disk, using Cathode strop chambers (CSCs) (Figure 3.7).

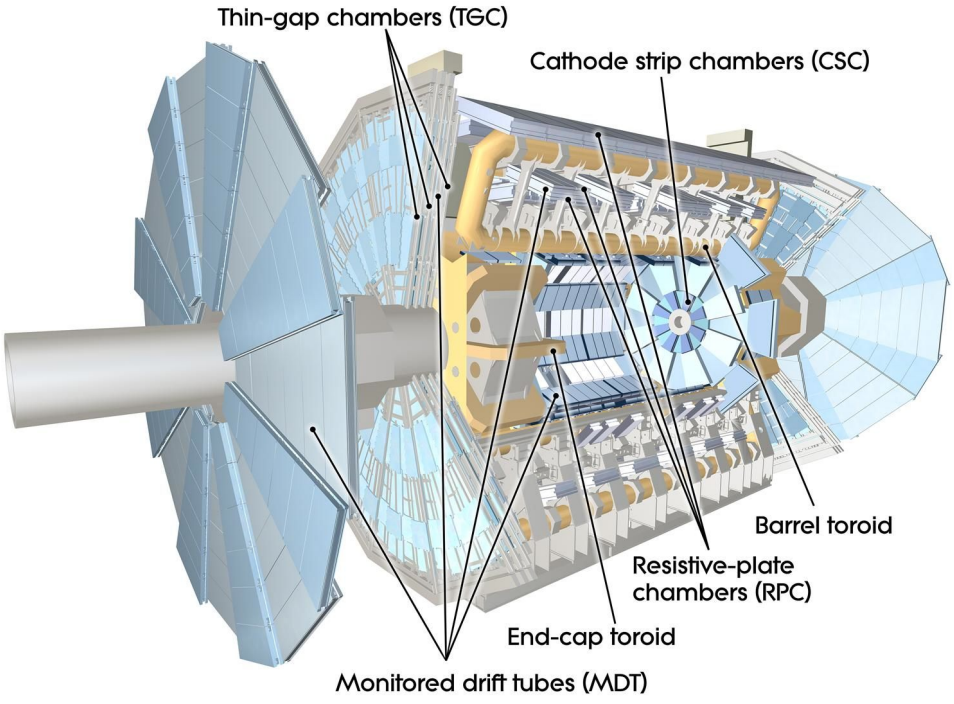

Figure 3.7: Layout of the ATLAS muon spectrometer [46]

3.2.4 Trigger system

The data at LHC is always produced with a high rate, whereas the data writing to storage at LHC is limited. In addition, the interaction processes are not usually interesting. Therefore, a trigger system is

applied to select and save the interesting physics events for offline analysis.

Choosing and recording online events of the ATAS trigger system are carried through three different levels. Each trigger level refines and adds necessary selection criteria to the choices of the former level [43], [47].

The level 1 trigger makes the first level of event selection. It explores signatures from leptons, photons and jets, and selects the physics processes having high missing transverse energy. This level cuts down the number of events from a bunch-crossing rate of 40 MHz to lower than 75 kHz.

The level 2 trigger uses the so-called Regions-of-Interest (RoI) data identified by the level 1 trigger with approximately 10 ms average event time of treatment. In order to get this time, the level 2 trigger uses a succession of highly optimised trigger selection algorithms. It can access the data in different elements such as coordinates, energy and type of signatures to reduce the rate of events from the regions of interest to around 1 kHz.

The level 3 trigger, known as the Event Filter, completes the event building procedure. It reduces the event rate to approximately 100 Hz and classifies the selected events according to the ATLAS physics streams, for instance electrons, muons, jets, photons, missing transverse energy, tau-leptons and *b*-physics.

3.2.5 Objects identification

The ATLAS detector is constructed by the systematic and logical arrangement of different types of instruments in many layers in order to detect preferably all particles produced from interactions. The objects of the interesting events can be collected and measured at different layers of the detector because of their properties.

As mentioned in Chapter 2, the final state of the $t\bar{t}$ pair decay contains two leptons and two neutrinos which are products of W bosons decay as well as two b-jets.

Electrons (positrons) are charged particles, leaving tracks in the ID as the first signature in the detector. They then lose their energy almost exclusively by bremsstrahlung radiation at high energies and produce showers in the EM calorimeter. The length of a shower is set by the radiation length based on the calorimeter material. The energy of particles can be determined by the cascades measurements when they pass through the active material and ionize.

One should take into account that photons also lose their energy in the EM calorimeter by the cascades of producing electrons–positrons. However, photons are neutral particles, so they do not leave tracks in the ID. Therefore, in order to separate electrons from photons, electrons reconstructed from ID tracks have to be associated with EM calorimeter clusters.

Muons (anti-muons) are charged leptons which can pass through the calorimeters almost without losing their energy thanks to their much larger mass. Nevertheless, they are detected when passing through the muon spectrometer system with the coherent information between this system and the tracking system.

The *b* quarks have a long lifetime and form regular jets by hadronisation. They can be discriminated from light quark jets mainly due to the long lifetime of *B*-hadrons[1]. The jets are reconstructed by the anti-k_t algorithm. The secondary decay vertex is typically located away from the primary vertex, which can be measurable by suitable reconstruction methods in the detector. The so-called *b*-tagging algorithm is used in order to identify the jets originating from *b* quarks and is based on which properties of *B*-hadrons.

[1] These are hadrons with *b*-quark flavour

Neutrinos are neutral and virtually massless. They hardly interact with the detector materials. However, they carry a significant transverse momentum and contribute to the large amount of missing transverse energy of the investigated event.

An illustration of particle detection in the subsystems of the ATLAS detector is given in Figure 3.8.

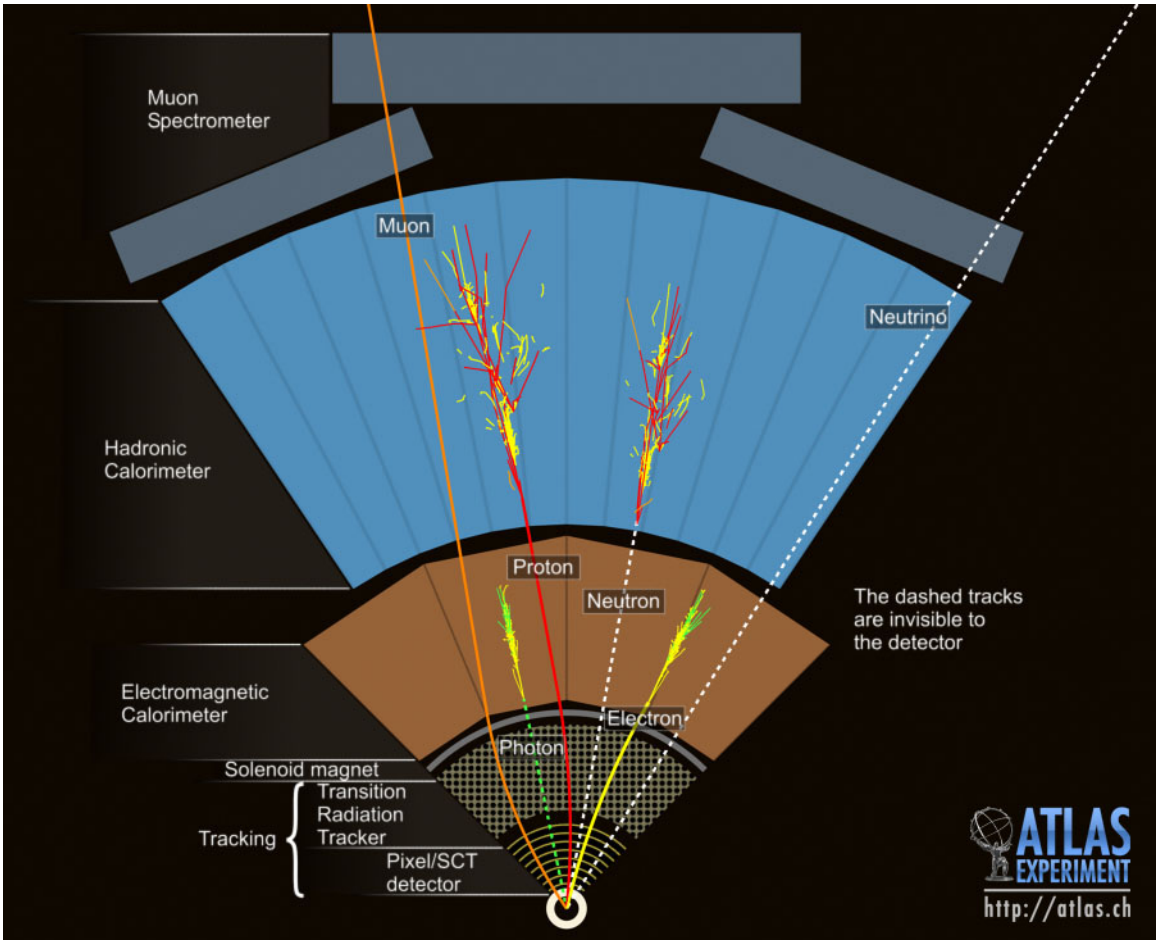

Figure 3.8: The signature of particles in different detector components of the ATLAS detector(Courtesy CERN).

CHAPTER 4

Methodology

This chapter explains the signal and background estimations in the dilepton decay channel of the $t\bar{t}$ events, and then the data and MC samples used for the analysis are described. The next discussion in this chapter is the object and event optimisation cuts applied to select the candidate signal event from the data samples. Finally, the methodology used for the top quark mass measurement is presented.

4.1 Signal and background estimation

As mentioned in Chapter 2, the $t\bar{t}$ pairs mainly decay into three modes with dileptonic, lepton + jets and all hadronic channels. The dilepton decay channel of the top pair production consists of:

- two leptons that can be electrons or muons with opposite charges.
- two jets coming from b-jets. Note that additional jets in the event are possible due to gluon emissions but they are expected to have relatively low transverse momenta.
- the missing transverse energy (E_{T}^{miss}) mostly contributed by two lepton neutrinos.

To summarise, the expected experimental signature of the signal process has exactly two isolated leptons with opposite charges and high transverse momentum, at least two jets coming from two b quarks and high E_{T}^{miss}.

However, there are several processes that give the same final state as the dilepton decay channel of the $t\bar{t}$ event in the detector, the so-called physics background. The physics background of the dilepton channel can be estimated directly from the MC sample technique by using their theoretical cross sections. The background estimation is determined as follows.

The single top production, from the Wt channel, is the most important process of the background estimated by the MC simulation (Figure 4.1a).

The diboson productions, including WW, WZ and ZZ production, contribute into the background of dilepton analysis, known to be due to leptons coming from W and Z decays. Figure 4.1b also shows one of the example of the diboson production.

The Z + jets processes are produced with associated jets and E_{T}^{miss} due to resolution effects and measurement errors. The Feynman diagram of Z + jets production and decay process is displayed in Figure 4.1c.

Fake leptons or fakes are hadrons misidentified as leptons or non-prompt leptons which are not created from the W-boson decay. The fakes of the dilepton signatures are more common from the lepton + jets decay channel of the top pair production. In this process, one lepton can be real from the W-boson decay, and one fake lepton is probably originated from a decay product of one of the jets. The fakes background affects the e^+e^- and $e^\pm\mu^\mp$ modes much more than the $\mu^+\mu^-$ mode because the electrons misidentification sources, such as jets, photons and heavy flavour decays, are more likely to be misidentified than their muons counterparts, namely heavy flavour hadrons. To estimate the fake leptons background, a data driven matrix method is applied [48], consisting of a full matrix method that estimates fake rates from lepton + jets selections.

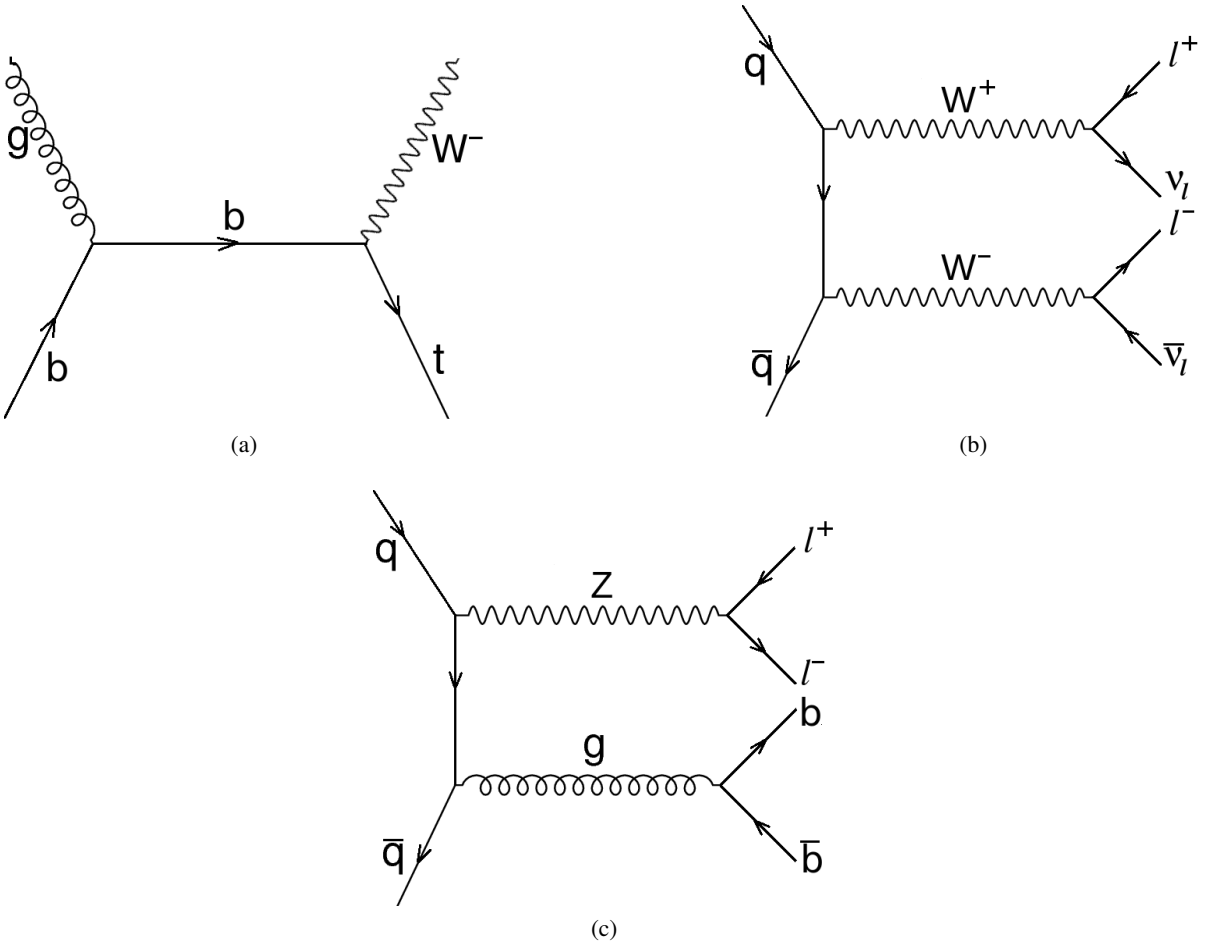

Figure 4.1: Physics background of the $t\bar{t}$ →dilepton decay channel. (a): The Wt-channel of single top production, (b): Diboson production and (c): The Z + jets process

4.2 Data and Monte-Carlo samples description

4.2.1 Data samples

In this thesis, the data collected by the ATLAS detector in the LHC proton-proton collisions at $\sqrt{s}$ = 7 TeV during the year of 2011 (from March, 2011 to October, 2011) are used. The data-taking is

composed of different small time intervals, called luminosity block, corresponding to a coherent configuration of the detector and the trigger systems [49].

The total integrated luminosity is determined by integrating over the luminosity blocks [50]. The data samples used in the study have a total integrated luminosity of 4.7 fb^{-1} with an uncertainty of 1.8% [51]. The ratio of the recorded to delivered luminosity in ATLAS is 93.5% [52] the data taking efficiency.

The data samples used are divided into different periods, associated to the letters from B2 to M [49]. The list of data samples is shown in Table 4.1.

Table 4.1: 2011 data taking periods [53]

Period	Date range	Run range
B2	Mar 22th – Mar 24th, 2011	178044 - 178109
D	Apr 24th – Apr 29th, 2011	179710 - 180481
E	Apr 30th – May 3rd, 2011	180614 - 180776
F	May 15th – May 25th, 2011	182013 - 182519
G	May 27th – Jun 14th, 2011	182726 - 183462
H	Jun 16th – Jun 28th, 2011	183544 - 184169
I	Jul 13th – Jul 29th, 2011	185353 - 186493
J	Jul 30th – Aug 4th, 2011	186516 - 186755
K	Aug 4th – Aug 22th, 2011	186873 - 187815
L	Sep 7th – Oct 5th, 2011	188902 - 190343
M	Oct 6th – Oct 30th, 2011	190503 - 191933
Total	Mar 22th – Oct 30th, 2011	178044 - 191933

4.2.2 Monte-Carlo samples

Monte-Carlo (MC) simulation is used to determine the acceptance of the signal events as well as the contributions of background processes. The MC samples used in the study are provided by GEANT4 simulation [54] and the MC11 production campaign of the ATLAS Production Group [55]. The luminosity of MC samples are re-weighted in order to make the MC expectation compatible with the collected data.

The MC samples used in the study can be ordered in three groups: $t\bar{t}$ signal samples, background samples and $t\bar{t}$ systematics variation samples.

Signal samples are separated in two subgroups and are displayed in Table 4.2. All samples simulated consists of the multiple soft proton-proton collisions. The standard $t\bar{t}$ sample of 172.5 GeV used in this analysis is created by POWHEG + PYTHIA MC generator (sample no. 117050). The other nominal value of top mass samples coming from other generators such as MC@NLO+HERWIG /JIMMY are used for estimating systematic uncertainties. The $t\bar{t}$ samples of the full simulation with different assumed masses (from 165 GeV to 180 GeV) are produced from POWHEG + PYTHIA MC generator.

Table 4.2: $t\bar{t}$ signal MC samples [55].

Sample mass	Sample number	MC generator
$t\bar{t}$ baseline samples (GeV)		
172.5	105200	MC@NLO + HERWIG /JIMMY
172.5	105860	POWHEG + HERWIG /JIMMY
172.5	117050	POWHEG + PYTHIA
$t\bar{t}$ variation samples (GeV)		
165.0	117836	POWHEG + PYTHIA
167.5	117838	POWHEG + PYTHIA
170.0	117840	POWHEG + PYTHIA
175.0	117842	POWHEG + PYTHIA
180.0	117844	POWHEG + PYTHIA
190.0	117846	POWHEG + PYTHIA

Background samples are generated with different MC generators listed in Table 4.3. Background processes are described in Section 4.1. Note that multiple soft proton-proton collisions are added to all samples simulated.

- Diboson production samples are modelled using the ALPGEN + HERWIG generator.
- There are three categories of Z + jets background samples. Z + *jets* unfiltered samples are generated with dileptons in the invariant mass range of 40 GeV–2 TeV. $Z + b\bar{b}$ + jets samples are created with the mass of the lepton pair formed within the window 30 GeV–10 TeV. On the other hand, the low iMass Z + jets (Drell-Yan) samples have the dileptons invariant mass range of 10 GeV $< m_{\ell\ell} <$ 40 GeV. All these samples are created from the ALPGEN + HERWIG /JIMMY generator.
- Single top quark production in the Wt-channel is simulated using the ALPGEN + HERWIG/JIMMY.

Table 4.3: Background MC samples [55].

Sample	Sample number	MC generator
Diboson	107100 - 107111	ALPGEN + HERWIG
***Z* + jets unfiltered**		
$Z(e^+e^-)$ + jets	107650 - 107655	ALPGEN + HERWIG /JIMMY
$Z(\mu^+\mu^-)$ + jets	107660 - 107665	ALPGEN + HERWIG /JIMMY
$Z(\tau\tau)$ + jets	107670 - 107675	ALPGEN + HERWIG /JIMMY
Drell-Yan		
$Z(e^+e^-)$ + jets	116250 - 116255	ALPGEN + HERWIG /JIMMY
$Z(\mu^+\mu^-)$ + jets	116260 - 116265	ALPGEN + HERWIG /JIMMY
$Z(\tau\tau)$ + jets	116270 - 116275	ALPGEN + HERWIG /JIMMY
***Z* + $b\bar{b}$ + jets**		
$Z(e^+e^-)bb$ + jets	109300 - 109303	ALPGEN + HERWIG /JIMMY
$Z(\mu^+\mu^-)bb$ + jets	109305 - 109308	ALPGEN + HERWIG /JIMMY
$Z(\tau\tau)bb$ + jets	109310 - 109313	ALPGEN + HERWIG /JIMMY
Single top		
Wt-channel	108346	ALPGEN + HERWIG /JIMMY

Systematic variation samples are used to estimate the systematic uncertainties, which are discussed more precisely in Chapter 5. The list of systematic sources is shown in Table 4.4.

- The $t\bar{t}$ ISR/FSR variation samples are produced with increased and decreased initial/final state radiation with the AcerMC + PYTHIA generator.
- The $t\bar{t}$ samples used to determine the uncertainty due to non-perturbative modelling consist of colour reconnection (CR) and underlying event (UE) variations, which are estimated using the POWHEG + PYTHIA.
- For evaluation of the $t\bar{t}$ renormalisation and factorisation (Ren./Fac.) scale variation systematic uncertainties, the MC@NLO + HERWIG/JIMMY are used in order to assess the possible differences in acceptance.

Table 4.4: Systematic source samples [56].

Sample	Sample number	MC generator
$t\bar{t}$ ISR/FSR variation		
More parton showers (PS)	117862	AcerMC + PYTHIA
More parton showers (PS)	1117863	AcerMC + PYTHIA
$t\bar{t}$ non perturbative		
Base	117428	POWHEG + PYTHIA
Underlying Event (UE)	117429	POWHEG + PYTHIA
Colour Reconnection (CR)	117430	POWHEG + PYTHIA
$t\bar{t}$ renormalisation and factorisation (Ren./Fac.) scale variation		
μ_{down}	110006	MC@NLO + HERWIG /JIMMY
μ_{up}	110007	MC@NLO + HERWIG /JIMMY

4.3 Object and event selection

As mentioned in Section 4.1, the reconstructed objects in the detector are lepton candidates (electrons or muons), jets and E_{T}^{miss}. All requirements applied for objects and event selections are based on the "TopCommonObjects2011" section available in reference [57].

4.3.1 Object selection

Electrons candidates are required to have a transverse energy $E_{\mathrm{T}} > 25$ GeV and a pseudo-rapidity from the central part of the detector $|\eta| < 2.47$, except for the calorimeter crack region of $1.37 < |\eta| < 1.52$ because of the clusters falling in the calorimeter transition area.

In order to select high quality electrons, isolation criteria known as the "Tight++" criteria must be applied to limit the amount of energy situated near the candidates, which can discriminate well between selected electrons and jets duplicating electron signatures or heavy flavour decays inside jets.

The deposited energy in the EM calorimeter not associated to an electron cluster and located within a cone of radius $\Delta\mathrm{R} = 0.2$ to an accepted electron must not exceed a threshold depending on η and the number of primary vertices. Additionally, the summed scalar p_{T} of all tracks within a cone of $\Delta\mathrm{R} = 0.3$ around the electron direction is also required to be lower than a threshold based on the cluster energy and η.

Furthermore, the jet-electron overlap removal is applied for jets in a cone of $\Delta R \leqslant 0.2$ from the electron direction. After that, the electrons are rejected if any jets having $p_{\mathrm{T}} > 20$ GeV are found within a cone of $R \leqslant 0.4$.

Muons candidates are selected by an ATLAS muon reconstruction chain algorithm, the so-called Muid [58], where the combined information of both muon spectrometer and ID systems are used for reconstructing muon objects.

In the muon spectrometer system, the requirements of muon transverse momentum $p_{\mathrm{T}} > 20$ GeV to be on the plateau of the single muon trigger efficiency and the detector acceptance of $|\eta| < 2.5$ are applied in order to accept muon candidates.

Similarly to the electrons, the muon isolation is also used to remove muons overlapping with jets. In order to reduce muon candidates from heavy and light flavour decays, the muons placed in the spatial distance of $\Delta R \leqslant 0.4$ between muons and jets having $p_{\mathrm{T}} > 25$ GeV and the jet vertex fraction $|\mathrm{JVF}| > 0.75$ are discarded. JVF is the ratio of the scalar total transverse momenta p_{T} associated to the tracks used to reconstruct the primary vertex and the jet. Furthermore, the sum of the transverse energy within a cone of $\Delta R = 0.2$ around selected muons and the transverse momentum of ID tracks with $\Delta R \leqslant 0.3$ of muons directions are required to be less than 4 GeV and 2.5 GeV, respectively. In addition, the ID hit requirements are used for muon selection.

Jets are reconstructed by the anti-k_t jet reconstruction algorithm of ATLAS with a radius parameter of 0.4, using the topological clusters with EM calorimeter and jet energy scale (JES) calibration [59]. The jets with negative energy are removed. The jet quality criteria are applied to suppress the so-called bad jets which are the jets not associated to real energy deposits in the calorimeters. The criteria follow the loose selection detailed in reference [60]. Jet candidates with $p_{\mathrm{T}} > 25$ GeV and $|\eta| < 2.5$ are considered. In order to reduce the effect of pile-up, a cut on $|\mathrm{JVF}| > 0.75$ is suggested. The jets overlapping with accepted electrons within $\Delta R \leqslant 0.2$ distance are removed such that the double-counting of objects is avoided.

An important selection criterion applying for top quark events is the identification of b-jets. The b-jets can be distinguished from light quark jets thanks to the relatively long lifetime of b-flavoured hadrons. This leads to a significant flight path of B hadrons with secondary vertices as well as impact parameters of the decay products that could be measured. The so-called b-tagging algorithms are used for identifying b-quark jets, using the tracks associated with the jets. The MV1-tagger takes the weights of tagging algorithms, as well as p_{T} and η of the jet, as an input to a neural network method [61]. The MV1-tagger working point used in the study correspond to an overall b-tagging efficiency with 70% and 85% respectively.

Missing transverse momentum $\vec{p}_{\mathrm{T}}^{\,miss}$ and its magnitude E_{T}^{miss} are computed using energy clusters

determined in the electromagnetic cells, corresponding to reconstructed high p_{T} objects in the event consisting of electrons, photons, jets, soft jets, and muons. Muons are included using their momentum measured from the tracks in the ID and muon spectrometers, whereas the electrons, high p_{T} jets and soft jets clusters are used after calibration at the electromagnetic scale and corrected for the objects energy scale. The remaining energy from cells that is not associated with a high p_{T} object are called the "CellOut" term. The E_{T}^{miss} is calculated as follows.

$$E_{\mathrm{T}}^{miss} = \sqrt{(E_{\mathrm{x}}^{miss})^2 + (E_{\mathrm{y}}^{miss})^2} \tag{4.1}$$

where:

$$E_{\mathrm{x,\,y}}^{miss} = -(E_{\mathrm{x,\,y}}^{e} + E_{\mathrm{x,\,y}}^{\mu} + E_{\mathrm{x,\,y}}^{jets} + E_{\mathrm{x,\,y}}^{softjets} + E_{\mathrm{x,\,y}}^{CellOut}) \tag{4.2}$$

4.3.2 Event selection

As considered in Section 4.1, the final state of $t\bar{t}$ pair decay is characterised by the presence of two isolated leptons with high p_{T}, at least two b-jets and E_{T}^{miss} coming from two neutrinos. Following the selection requirements of reconstructed objects, the events for this study are selected as follows:

- The suitable single electron or single muon trigger are required depending on the data taking period.
- At least one primary vertex candidate reconstructed from at least five tracks is required.
- The matching distance between a selected lepton and the trigger object shall not be larger than 0.15.
- Events must have exactly two opposite charged leptons.
- Events in the e^+e^- and $\mu^+\mu^-$ modes must satisfy $E_{\mathrm{T}}^{miss} > 60$ GeV. Other requirements added in theses modes are $m_{\ell\ell} > 15$ GeV to reduce the low mass resonances background, and $|m_{\ell\ell} - m_Z| > 10$ GeV ($m_Z = 91$ GeV) to suppress the Drell-Yan processes.
- The scalar sum of p_{T} of all selected leptons and jets, H_{T}[1] > 130 GeV is required in the $e^{\pm}\mu^{\mp}$ channel.
- Events must include at least two jets, in which at least two b-tagged jets at leading p_{T} are taken into account.

4.3.3 Optimisation cuts

For this analysis, the criteria of jets transverse momentum and the working point of b-tagging efficiency have been obtained from a optimisation analysis, similarly to what has been done in reference [26]. The optimisation is based on reducing the total uncertainty value on the top quark mass measurement. The total uncertainty consisting of the statistical and all systematic sources uncertainties is determined by $\sqrt{\sigma_{\mathrm{stat.}}^2 + \sigma_{\mathrm{syst.}}^2}$. Systematic sources are discussed in detail in Chapter 5.

The analysis considers various cuts applied and estimates the optimal woring point with minimise systematic uncertainties. This analysis is fulfilled in a series of steps. The study starts with the standard selection defined as in subsection 4.3.2 at the working point of MV1 corresponding to the b-tagging

[1] Defined in Appendix A

efficiency of 70% and compare the performance to the b-tagging efficiency of 85%. Following this change, the jets transverse momentum cuts applied vary from 25 GeV to 50 GeV in a step of 5 GeV.

Thanks to this analysis, the extra selection of events is selected with the working point MV1 at 85% b-tagging efficiency and $p_{\mathrm{T}}^{jet} > 45$ GeV.

4.4 Methodology

4.4.1 The calibration curve method

There are different analysis strategies to measure the top quark mass. This thesis uses a calibration curve with the general description in the following steps [26], [7].

- Choose an observable sensitive to the top quark mass.
- Use MC simulation samples at different top quark mass points as the templates to measure the selected observable, and then create the calibration curve to perform the relation of this observable values and the top mass.
- Apply the measurement to determine the chosen observable value in data.
- Assess the top quark mass value from the measured value in data through the calibration curve.
- Evaluate systematics effects that possibly modify the measurement result.

The thesis analysis proposes a particular strategy in order to measure the top quark mass as follows.

- The distributions of three kinematic variables m_{T2}, $m_{\mathrm{T2}\perp}$ and $m_{\ell b}$ in the dilepton channel are considered.
- An optimised function is selected to fit these variables distributions. The selected observable for the measurement is the mean parameter of the fit function.
- A selected function is used to fit all distributions of signal and background templates for the variables illustrated at different MC top mass variation samples in the range from 165 GeV to 180 GeV, introduced in Table 4.2. The mean parameter values of the fit function from these distributions are then collected to make the calibration curve corresponding to each variable. The central value of 172.5 GeV of the top mass sample is used as a test mass in order to guarantee the accuracy of the measurement.

Note that the top quark mass is measured by these three variables independently and thus the most optimal estimator of the analysis is identified.

4.4.2 Top quark mass determination from the calibration curve

From fitting the distributions at different top mass input values of the MC samples, the value of the observable, mean parameter value of the fit function (μ), as well as its statistical uncertainty at every mass point is extracted.

The calibration curve showing the relation of the observed value of the top mass is a first degree polynomial function (a linear function). From the calibration curve, the top quark mass value is determined by the formula:

$$m_{\text{top}}(p_0, p_1, \mu) = \frac{(\mu - p_0)}{p_1} \tag{4.3}$$

where: p_n is the calibration parameter corresponding to the n–th degree term of coefficient.

A calibration curve created from different mass variations of MC samples and a mass extraction are illustrated in Figure 4.2.

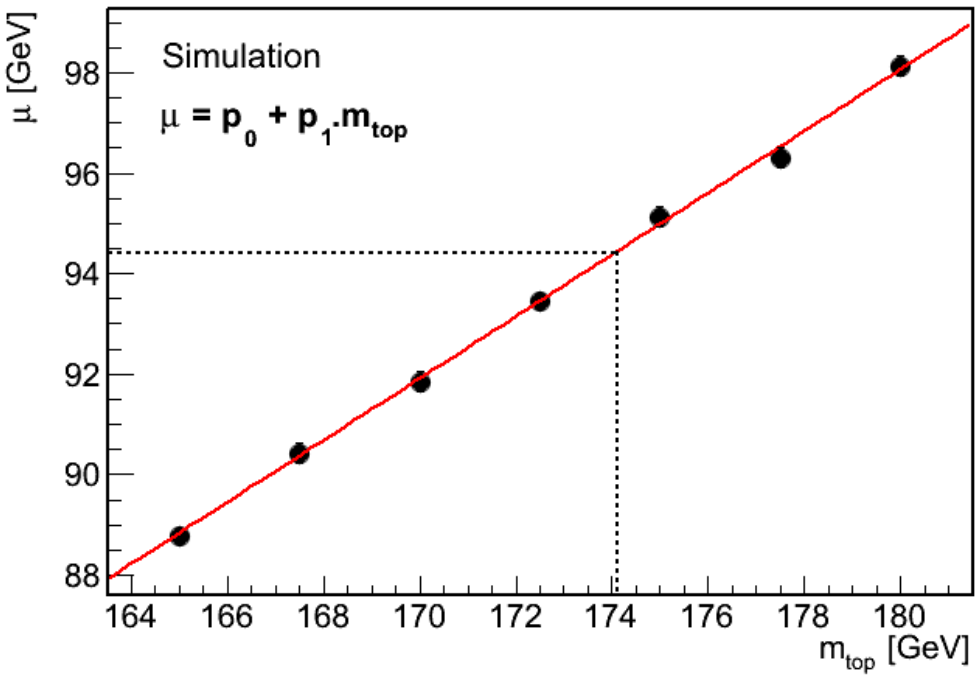

Figure 4.2: An example of calibration curve and top mass extraction

CHAPTER 5

Systematic uncertainties

Measurements are always affected by statistical and systematic uncertainties. Statistical uncertainties are due to the random fluctuations coming from the finite set of observations. On the other hand, systematic uncertainties result from uncertainties related to the nature of the measurement apparatus, assumptions made by the experimenter or the model used to make inferences based on the observed data [62].

The systematic uncertainties of the present analysis are estimated by varying the quantities associated with different systematic sources in the signal and background MC samples. The effect of these variations are interpreted as one standard deviation in the upward or downward direction. The differences to the evaluation from the nominal analysis are reported as systematic uncertainties. The total systematic uncertainty is computed by the quadratic sum of the systematic values, since different components. The estimation of systematic uncertainties in this thesis is based on the final recommendations for 2011 release 17 analysis of the ATLAS top reconstruction group [56].

This chapter contains a short description of the systematic sources as well as their estimation in the $t\bar{t}$ →dilepton decay channel, according to the following list:

- Objects systematics
  - Jets
    - Jet energy scale
    - b-jet energy scale
    - Jet energy resolution
    - Jet reconstruction efficiency
    - b-tagging and mistag rate efficiency
  - Electrons
    - Electron trigger efficiency
    - Electron reconstruction and identification efficiency
    - Electron energy scale
    - Electron energy resolution
  - Muons
    - Muon trigger efficiency

        - Muon reconstruction and identification efficiency
        - Muon momentum scale
        - Muon momentum resolution
    - Missing transverse momentum
        - Cell-Out and soft jets uncertainty
        - Pile-up uncertainty
- Signal and background normalisation systematics
- Systematics from the method calibration
- $t\bar{t}$ production modelling
    - Initial and final state radiation modelling
    - Underlying events
    - Colour reconnection
    - Hadronisation
    - Monte-Carlo generator systematics
    - Renormalisation and Factorisation variations

5.1 Objects systematics

5.1.1 Systematics related to jets

Jet energy scale (JES) uncertainty is the dominant systematic uncertainty in this study. It accounts for the JES calibration derived by using the information from test-beam data, the LHC collision data and simulation and depends on the jet transverse momentum (p_{T}^{jet}) and η [63]. The "MultijetJES-UncertaintyProvider" tool is implemented to estimate the JES uncertainty values for individual jets, described in a number of steps [56]. The JES uncertainty is composed of different components resulting from the detector simulation, the calorimeter response, the calibration curve and the particular selection of parameters in the MC event generator. There are different components of JES with a proper treatment of the correlations between the nuisance parameters. Therefore, these components are uncorrelated. Each JES component in the corresponding MC samples is independently varried by $\pm 1\sigma$ with respect to the default value and scaled by the values of one standard deviation upward and downward in order to estimate the JES uncertainty. The components of JES in this analysis consist of:

- Detector nuisance parameters (Detector NP1 and NP2)
- Mixed nuisance parametesrs (Mixed NP1 and NP2)
- Modelling nuisance parameters (Modelling NP1, NP2, NP3 and NP4)
- Statistical nuisance parameters (Statistical NP1, NP2 and NP3)
- Eta intercalibration (statistical)
- Eta intercalibration (modelling)

- Flavour composition
- Flavour response
- Pile-up offset (μ term)
- Pile-up offset (NPV term)
- Relative non-closure MC
- Single Particle high p_T

***b*-jet energy scale (*b*-JES)** describes the remaining difference between jets coming from *b*-jets and light quarks after the global JES is determined. Its uncertainty is not correlated with the JES uncertainty and accounts for the uncertainties in the *b*-jets modelling of the MC samples. The b-JES scale factor is centrally integrated in the "MultijetJESUncertaintyProvider" package of the ATLAS software.

Jet energy resolution (JER) is the resolution of the reconstructed p_{T}^{jet}. The JER addresses the imperfection of the jet energy measurements in ATLAS. The jets energies in the MC samples are smeared using a Gaussian distributed random scale factor with the width of the resolution uncertainty matching to data. The "JetEnergyResolutionProvider" tool of the ATLAS software is used to estimate the JER uncertainty [56].

Jet reconstruction efficiency (JRE) accounts for the limited efficiency of the jet reconstruction algorithm. The JRE is determined by matching the jets in the calorimeter and tracking systems as a function of p_{T}^{jet} and η. Jets are randomly removed from the events with a JRE of data and MC simulation agreement of about 2%. The event selection and the fit are repeated with the changed samples. The difference of results with respect to the nominal samples are considered as the uncertainty. The "TopJetReconstruction-Efficiency" package is used to determine the JER uncertainty [56].

The jets systematic uncertainties impacts are propagated to the missing transverse momentum E_{T}^{miss}.

***b*-tagging efficiency and mistag rate (*b*-tagging)** agreement between data and MC are described by the *b*-tagging scale factors, derived for a given *b*-tagging working point with their uncertainties for every jet. The scale factors of *b*-tagging for *b*-jet as well as mistag including *c*-jet and light-flavour jets are measured separately within their uncertainties. These uncertainties estimate the systematic uncertainty related to *b*-tagging. The "BtaggingCalibrationDataInterface" tool is used to estimate the *b*-tagging systematic uncertainty [56].

5.1.2 Systematics related to electrons

The electron trigger efficiency (ElTRigS) uncertainty is taken into account because of the limited efficiency of the electron trigger. It can be estimated by reweighting of each event with its scale factor provided by "electron_SF_R17" tool [56].

The electron reconstruction and identification efficiency (ElRecIDS) uncertainties account for the inability to identify and reconstruct electrons perfectly. They are estimated together using the same concept and package as the electron trigger efficiency.

In order to estimate the systematic uncertainty, the reweighting factor, depending on the number of electrons in the event, the energy of each electron and the measured calorimeter cell position, must be considered. For each systematic uncertainty source, two distributions associated with up and down weighting variations are produced.

Electron energy resolution (ElER) and energy scale (ElES) are related to the measurement of electron energy in ATLAS. The electron energy is shifted by $\pm 1\sigma$ to account for a ElES miscalibration.

It is also smeared by a Gaussian distribution associated with random scale factor matching to data in order to consider the ElER uncertainty. The "EnergyRescaler" package is used to estimate these systematic uncertainties [56].

These systematic uncertainties are also propagated to E_{T}^{miss}.

5.1.3 Systematics related to muons

Muon trigger efficiency (MuTrigS) is considered due to the limitation of efficiency of muon trigger. The concept to determine this uncertainty is similar to ElTRigS uncertainty by reweighting method. The "MuonSF" class given by the ATLAS collaboration is used to estimate the MuTrigS uncertainty [56].

Muon reconstruction and identification efficiency (MuRecIDS) also contribute to the final uncertainty. Similar to the electrons, the muon reconstruction and identification efficiency uncertainties are estimated together by reweighting events. The muon identification efficiency is centrally provided by the ATLAS collaboration with the "MuonSF" package while the "MuonEfficiencyCorrections" tool is used to estimate this systematic uncertainty [56].

Muon momentum resolution (MuPtR) and Muon momentum scale (MuPtS) are estimated using the "MuonMomentumCorrections" tool of MCP [56]. They are correlated and related to the muon transverse momentum (p_{T}^{μ}) measurement. Similarly to the jets and electrons, p_{T}^{μ} in the MC simulation is smeared and corrected. The smearing parameters for ID and muon spectrometer momenta are varied upward and downward, separately. The highest and lowest values of the result obtained after smearing with these new parameters has been averaged to quote it as the systematic uncertainty.

As jets and electrons, these systematic uncertainties related to muons also affect $\vec{p}_{\mathrm{T}}^{miss}$.

5.1.4 Systematics related to the missing transverse momentum and jets

The missing transverse momentum $\vec{p}_{\mathrm{T}}^{miss}$ with its magnitude E_{T}^{miss} are determined in Eq. 4.3 and Eq. 4.2. As mentioned above, when the systematic uncertainties of the other objects originating from energy scale, energy resolution and objects reconstruction and identification are evaluated, they also affect the $\vec{p}_{\mathrm{T}}^{miss}$.

Cell-Out and soft jets (METCellOut) are 100% correlated and their uncertainties are calculated together. The Cell-Out term involves all energy deposits in the calorimeter not related to reconstructed objects. The METCellOut systematics is shifted by $\pm 1\sigma$ to accounting for E_{T}^{miss}.

Pile–up (METPileup) also affects the E_{T}^{miss} calculation; therefore, its contribution to the E_{T}^{miss} uncertainty has to be considered.

The "TopMetTool" package is used in order to estimate these systematic uncertainties [56]. This package rescales the E_{T}^{miss} with either upward or downward variations.

5.2 Computation of object systematic uncertainties

The contributions of the objects systematics to the top quark mass measurement are determined independently, where each object systematics contains two distributions of rescaled variations (upward and downward). Therefore, in order to estimate the object systematic uncertainties, three distributions are created:

- One distribution is computed from the standard MC signal + background sample including the central MC signal sample no.117050 and total background sample.
- Two other distributions with upward (or downward) variations of each object systematics.

Based on the calibration curve, the corresponding mass values of the observable value measured from these distributions are computed. The first one is called central mass and the others are named "up" and "down" mass values (from upward and downward variations).

In case that the up and down mass values are on different sides of the control mass, the systematic value for each object is computed as half the difference between the up and down masses and symmetrised for the negative and positive sides. If this is not the case, the half of the largest absolute difference between the up (down) mass and the control mass is taken and symmetrised. In this analysis, the former case generally takes place.

For object systematics consisting of different components, the final uncertainty for each object is the quadratic sum of the components.

5.3 Systematics from signal and background normalisation

The signal and background of the dilepton decay channel are described in Section 4.1, with all samples taken from MC simulation except for the fakes estimated from a data-driven method.

The normalisation uncertainties due to the theoretical cross section used for the MC simulations are considered. The $t\bar{t}$ signal has an uncertainty of 10%, the diboson and Z + jets share the same uncertainty of around 34% and the single top has around 9% [56].

The uncertainty due to the fakes is estimated by varying the data-driven sample with the upward and downward weights. The weights are derived from the difference between the observed (data) and predicted number of fake events in certain control regions for the $t\bar{t}$ →dilepton analyses. The present analysis applies the fake efficiency uncertainty of 50% to determine this systematic uncertainty [56].

5.4 Systematics from the method calibration

The limited size of the MC mass variation samples and the choice of a simplified fit result in a systematic uncertainty, the method calibration. This is reflected in the remaining mass differences between the fitted and input mass given by a MC simulation sample. The systematic uncertainty related to the method calibration is estimated from the propagation of the fit parameters uncertainty values into the mass measurement.

5.5 $t\bar{t}$ production modelling

5.5.1 Initial and final state radiation (ISR/FSR)

The ISR/FSR systematic uncertainty is associated with the difference between the initial (ISR) and final (FSR) state QCD radiations, possibly changing the jet energies and the jet multiplicity of the events. This uncertainty can be estimated by comparing two MC samples with different ISR and FSR parameter settings created from AcerMC + Pythia, corresponding to more and less parton showers.

Two mass measurements corresponding to the observed value from both distributions computed. The ISR /FSR systematics uncertainty is estimated as half of the mass difference between both variations. The value is then symmetrised [56].

5.5.2 Underlying event (UE)

The underlying event systematics addresses the uncertainty due to non-perturbative modelling, estimated using a ME/PS Pythia model with different UE activity levels. The systematic uncertainty is determined by a comparison between two tune samples, including the Perugia 2011 value having more semi-hard Multiple Parton Interactions and the Perugia 2011 mpiHI variation corresponding to sample no. 117428 considered as a base value, used for estimating colour reconnection systematics as well (see 5.5.3).

Similarly to the ISR/FSR systematics, two different mass values are deduced from the measured observable values and the calibration curve. However, the full mass difference between two samples is taken and symmetrised in this case [56].

5.5.3 Colour reconnection (CR)

The colour reconnection systematics contributes to the uncertainty resulting from non-perturbative modelling,similarly to the UE systematics. It is estimated by comparing two MC samples with different CR settings with Perugia 2011 and Perugia 2011 NOCR tune values. The estimation of this kind of systematics is the same as the UE systematics [56].

5.5.4 Hadronisation

Two MC simulation samples of the POWHEG generator are used to determine the systematic uncertainty related to the hadronisation. These are base-line samples with sample no. 105860 and 117050, incorporating the hadronisation and the parton showers with HERWIG/JIMMY and PYTHIA generators, respectively. The same way as UE systematics computation is applied for this systematics [56].

5.5.5 Signal MC generator (MCGen)

Signal MC generator systematic uncertainty is considered due to a possible bias arising by choosing the $t\bar{t}$ signal samples between different MC generator systems to do the measurement. In order to determine the MCGen systematic uncertainty, the study compares a pair of signal MC generator samples at $m_{\text{top}} = 172.5$ GeV, generated with MC@NLO (sample no.105200) and POWHEG (sample no. 105860), using the same program of HERWIG /JIMMY for hadronisation. The full mass difference in the same way as for the UE systematics determination is taken as the systematic uncertainty [56].

5.5.6 Renormalisation and factorisation (Ren./Fac.)

The renormalisation and factorisation systematics are also considered. Two samples corresponding to the matrix element Ren./Fac. scale variations by a factor of 2 (sample no. 110007) and 0.5 (sample no. 110006) are used. The Ren./Fac. systematic uncertainty is calculated the same way as MCGen systematics [56].

One consideration is that the Ren./Fac. systematics and MCGen systematics are compared together and the one having the larger value is considered as the final uncertainty of these systematics in order to avoid a double-counting [56].

CHAPTER 6

Results

This Chapter performs the measurement of the top quark mass, using the ATLAS data samples corresponding to the luminosity of 4.7 fb^{-1}recorded in 2011 at $\sqrt{s} = 7$ TeV. The analysis is based on the m_{T2}, $m_{\mathrm{T2}\perp}$ and $m_{\ell b}$ variables and the methodology explained in previous Chapters.

The main goal of the study is to minimise the total uncertainty. The baseline analysis with the standard selection is first performed at the MV1 working points corresponding to a b-tagging efficiency of 70%. The extra cuts are then discussed in the optimised analysis in order to reduce the total uncertainty.

The results of the study are summarised including the top quark mass values and their uncertainties.

6.1 Sensitivity of variables to the top quark mass

The distributions of three variables, m_{T2}, $m_{\mathrm{T2}\perp}$ and $m_{\ell b}$, were created using the MC samples with different input top quark mass, varying from 165 GeV to 180 GeV, in order to probe the sensitivity of these variables to the top quark mass. The dependence of the m_{T2}, $m_{\mathrm{T2}\perp}$ and $m_{\ell b}$ on the top mass is illustrated by histograms in Figure 6.1.

These histograms are produced at reconstruction level, where the possible detector effects are considered before the observables are obtained. One can see that the m_{T2}, $m_{\mathrm{T2}\perp}$ and $m_{\ell b}$ values are shifted to larger values as the input top mass increases. This gives the fact that the m_{T2}, $m_{\mathrm{T2}\perp}$ and $m_{\ell b}$ variables are sensitive to the top quark mass, in particular, the mean value of the distributions.

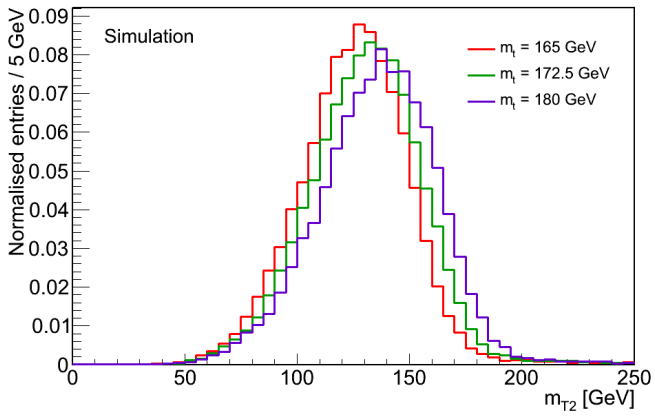

(a)

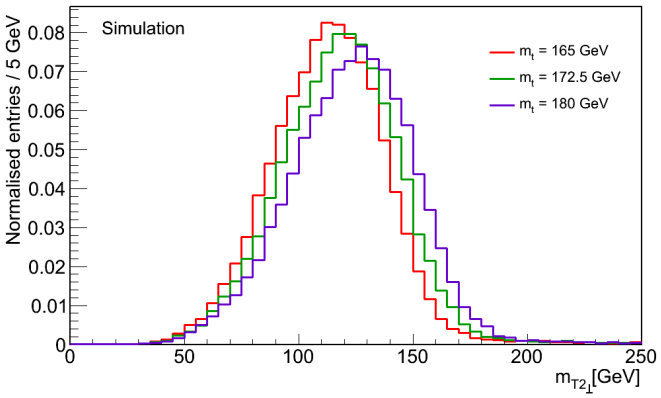

(b)

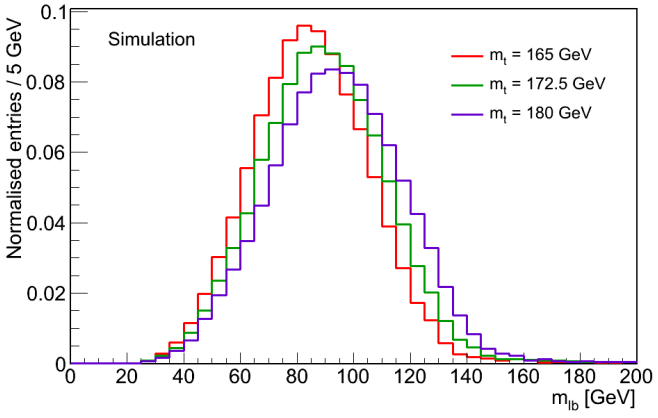

(c)

Figure 6.1: Distributions of the m_{T2} (a), $m_{\mathrm{T2}\perp}$ (b) and $m_{\ell b}$ (c) variables for different top mass points of MC samples after the standard selection

6.2 The repeated Gaussian fit

The top quark mass can be extracted using the calibration curve method as defined in Chapter 4. The observable is chosen to be the estimated mean from a fit function on each distribution for every variable. In the study, the observable is determined by using a repeated Gaussian function to fit the distributions with the following steps:

- Step 1: Use a simple Gaussian function to fit the distributions with a large range containing most of events.
- Step 2: Fit again the distributions by setting a new fit range defined by

  [central bin – binning range, central bin + binning range] (*binning size)

  where:
  - "central bin" is the bin including the mean of the Gaussian fit of the distribution
  - "binning range" is determined by the number of bins chosen.
- Step 3: Repeat step 2 until a stable fit result is found.

Figure 6.2 shows an example of the repeated Gauusian fit on one variable ($m_{\ell b}$) distribution with the standard selection. A reasonable fit on the distribution is evaluated by its acceptable goodness of fit value and its visible association to the distribution.

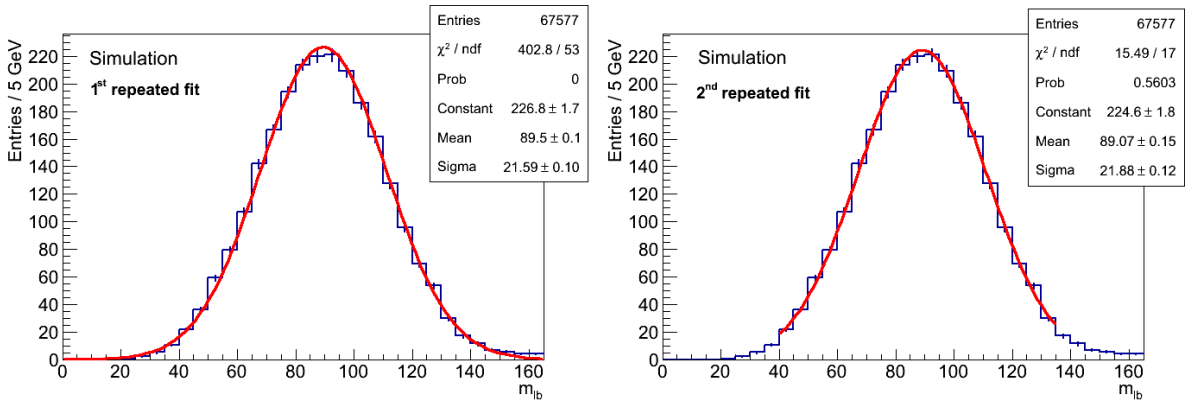

(a) (b)

Figure 6.2: An example of the repeated Gaussian fit,(a): the first repeated fit and (b) the second repeated fit.

The function selected only focuses on fitting a part of the distributions containing the mean of the distribution. The observable value for each distribution is the value of the fitted Gaussian mean. The binning size chosen in the analysis is 5 GeV. The "binning range" is chosen by scanning the numbers of bins in steps of 1 bin. The optimal "binning range" was selected based on the smallest total uncertainty for the measurement. Figure 6.3 shows results of systematic uncertainties based on the scanning of the "binning range". More detailed values of systematics and total uncertainties from the "binning range" scan are shown in Appendix B. Based on the scanning, a "binning range" of 7 bins was chosen for m_{T2} while the study in case of $m_{\mathrm{T2}\perp}$ and $m_{\ell b}$ was analysed at the "binning range" of 9 bins.

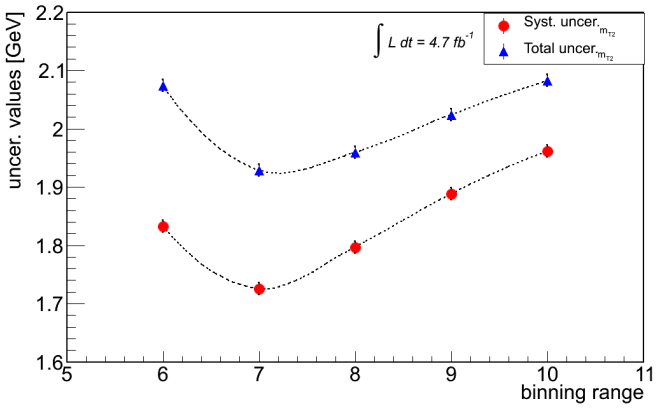

(a)

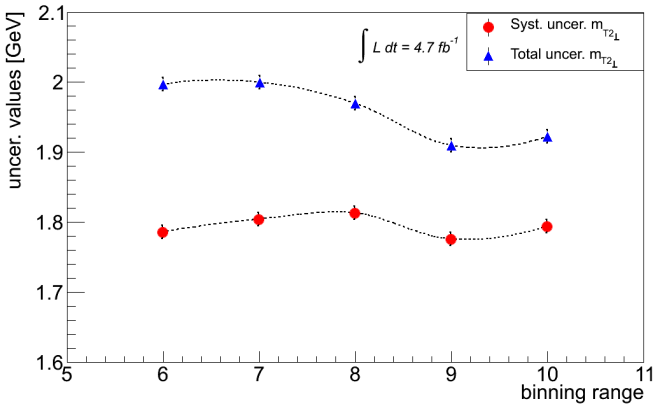

(b)

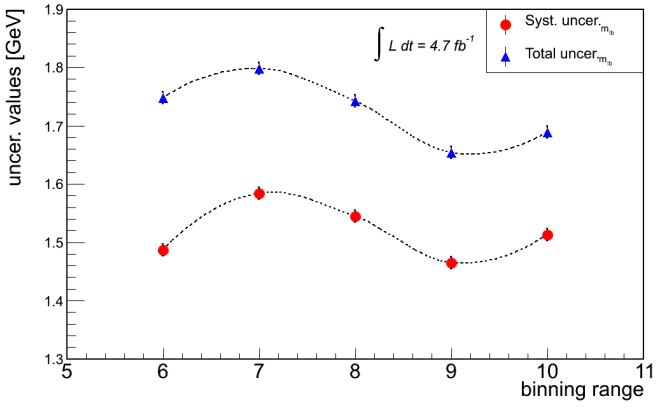

(c)

Figure 6.3: Systematic uncertainties at different binning ranges, (a) for m_{T2}, (b) for $m_{\mathrm{T2}\perp}$ and (c) for $m_{\ell b}$. The circle with red colour presents the systematic value and the triangle with blue colour shows the total uncertainties.

6.3 Basline analysis with the standard selection

Selection

The standard selection is introduced in subsection 4.3.2 together with the conditions of the MV1 corresponding to b-tagging efficiency of 70% and $p_{\mathrm{T}}^{jet} > 25$ GeV. Figure 6.4 shows the distributions of the number of jets and the number of b-tagged jets after the event selection. The distributions of E_{T}^{miss} in different decay modes are shown in Figure 6.5. Figure 6.6 and Figure 6.7 illustrate the distributions of p_{T} and η of the leading leptons and jets after applying the event selection, respectively. One can clearly see that the data and MC expectation distribution are not so agreeable. The difference between the data and MC expectation distribution displayed on the plots is by around 20%.

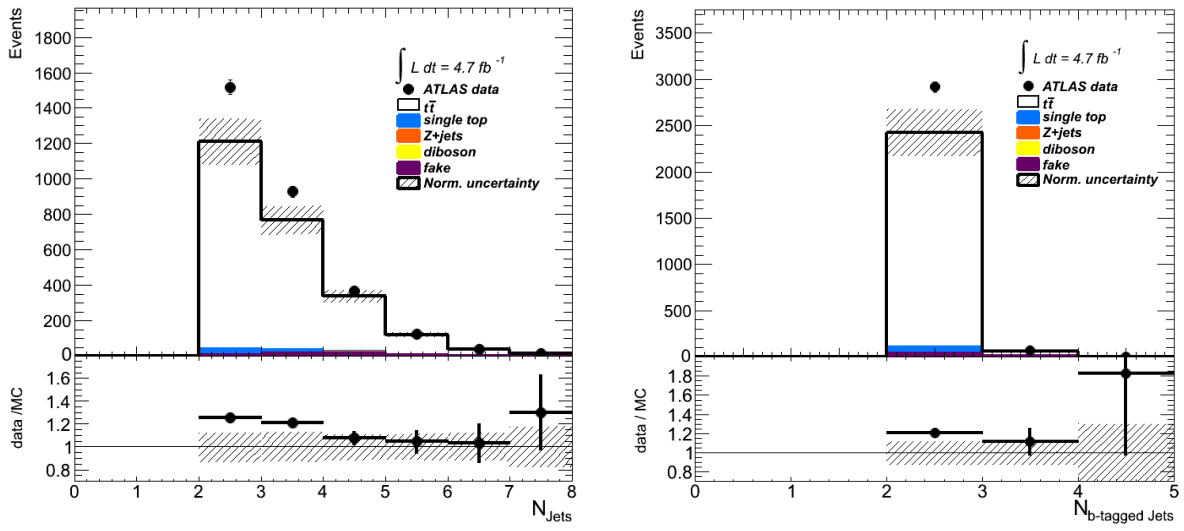

(a) (b)

Figure 6.4: Distributions of the number of jets (a) and b-tagged jets (b) at the standard selection. Histograms show the comparison between data and the expectation from MC simulation and the data-driven estimation of fakes distribution in Section 4.1. The hatched areas show the normalisation uncertainty including signal, background and luminosity uncertainties. The rightmost bin in the plots contains the overflow.

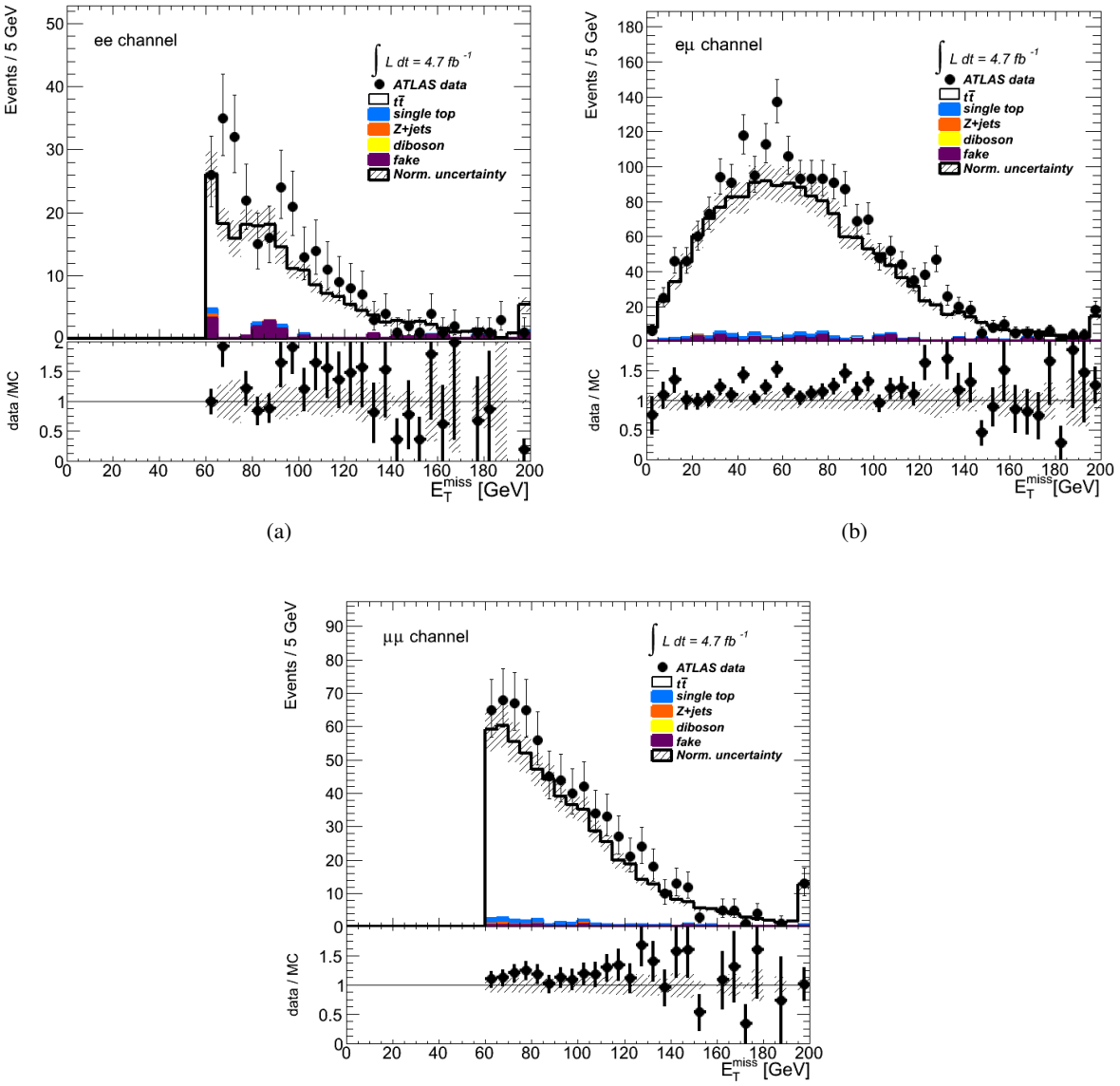

(a) (b)

(c)

Figure 6.5: Distributions of E_T^{miss} for the e^+e^- (a), $e^\pm\mu^\mp$ (b) and $\mu^+\mu^-$ (c) decay modes at the standard selection. Data is compared with the expectation from MC simulation and the data-driven estimation of fakes distribution in section 4.1. The hatched areas give the normalisation uncertainty including signal, background and luminosity uncertainties. The rightmost bin in the plots contains the overflow.

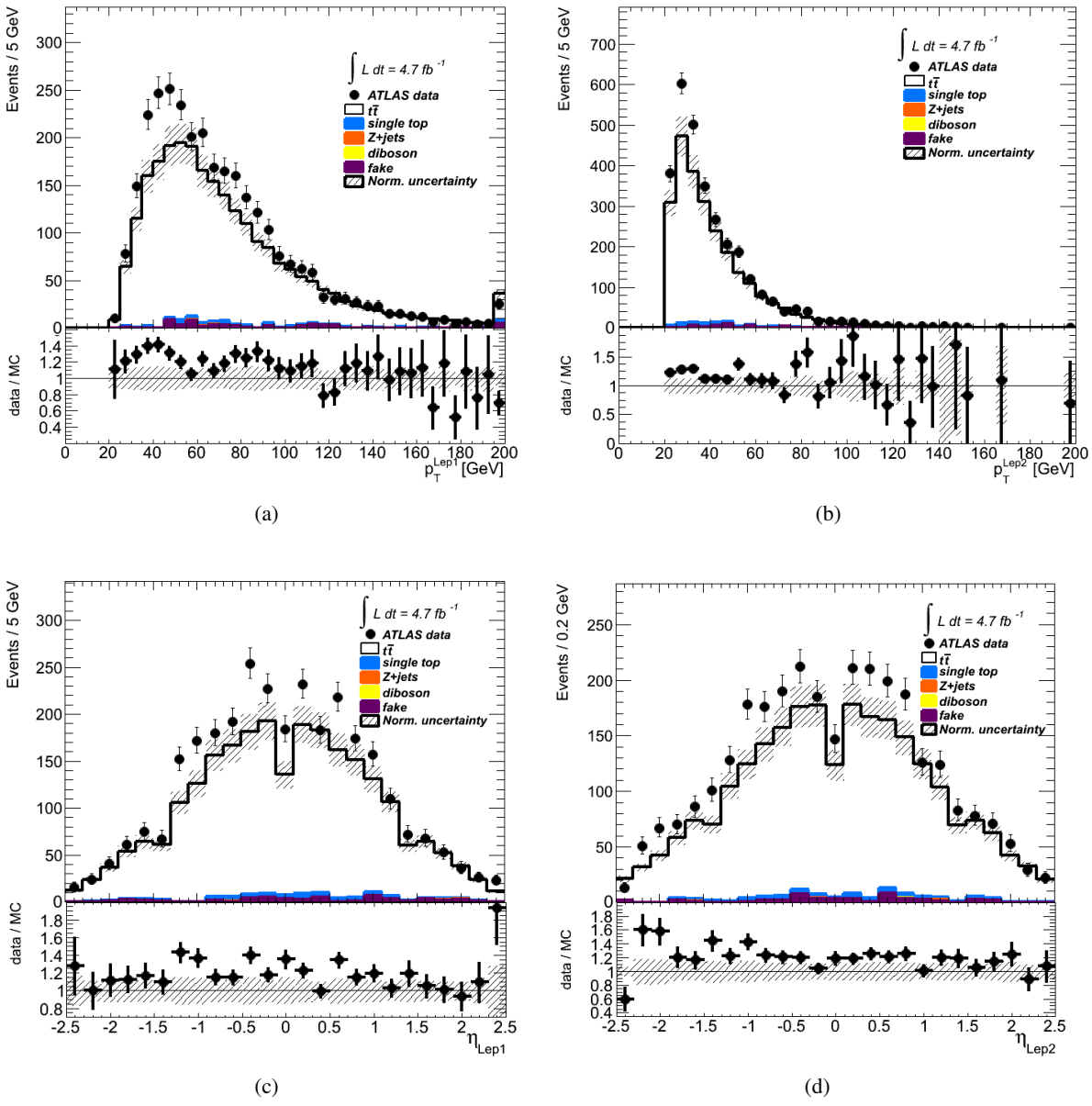

Figure 6.6: Distributions for p_{T} distributions (upper row) and η distributions (lower row) of the highest p_{T} lepton and the second highest p_{T} lepton, respectively. Histograms show the comparison between data and the expectation from MC simulation and the data-driven estimation of fakes distribution in section 4.1. The hatched area displays the normalisation uncertainty including signal, background and luminosity uncertainties. The rightmost bin in (a) and (b) contains the overflow.

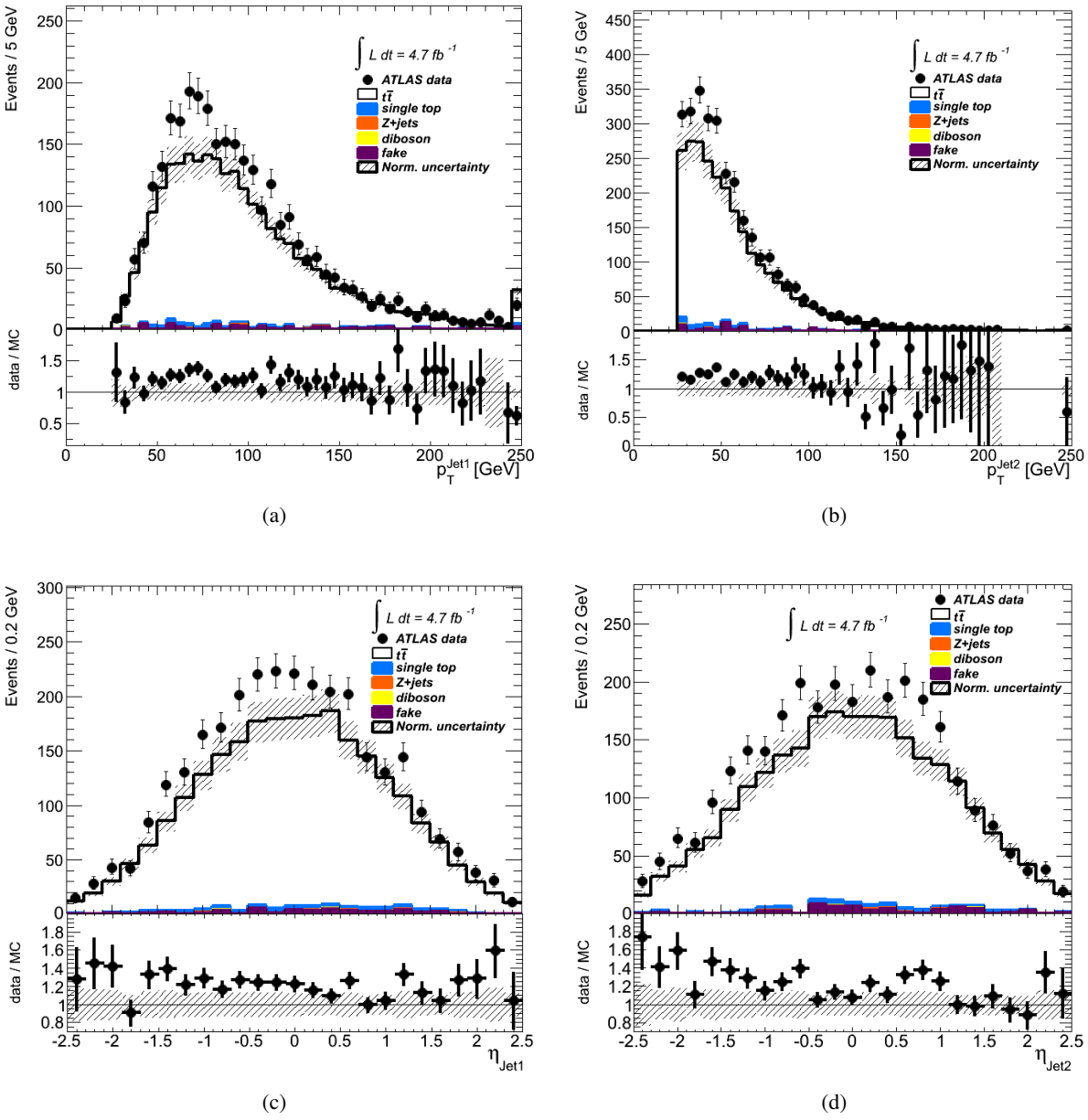

Figure 6.7: Distributions for the p_{T} distributions (upper row) and η distributions (lower row) of the highest p_{T} jet and the second highest p_{T} jet, respectively. Histograms show the comparison between data and the expectation from MC simulation and the data-driven estimation of fakes distribution in section 4.1. The hatched areas display the normalisation uncertainty including signal, background and luminosity uncertainties. The rightmost bin in (a) and (b) contains the overflow.

Data and MC samples

The number of observed dilepton candidate events is 2997, whereas the total numbers of expected events from MC simulation samples is 2493 ± 240 events. For the exspected events, the fakes background estimation is taken from data while the signal and remaining backgrounds are estimated from the MC simulation. Table 6.1 shows the expected and measured numbers of events after applying the standard selection.

Table 6.1: Events yields after the standard selection

Name	Events
$t\bar{t}$ signal	2384 ± 239
Single top	62.5 ± 6.2
Z + jets	4.1 ± 1.7
Diboson	0.4 ± 0.2
Fakes	42 ± 23
Total expected events	2493 ± 240
Observed events	2997

The understanding between the data and MC expectation distributions of different variables are described by histograms in Figure 6.8. The central top-quark mass MC sample of $m_{\text{top}} = 172.5$ GeV is used to compare with the data.

Fits and calibration curves

Based on the method discussed, templates are built for m_{T2}, $m_{\text{T2}\perp}$ and $m_{\ell b}$ as functions of the input top quark mass in the range of 165 GeV-180 GeV and then fitted by the repeated Gaussian. Figure 6.9a, 6.9c, 6.9e shows the repeated Gaussian fit on the central mass point distributions of the m_{T2}, $m_{\text{T2}\perp}$ and $m_{\ell b}$ with the standard selection. All distribution fits at different input top mass MC samples are displayed in Appendix C. The mean values of the fits at different top quark mass values are collected as in Figure 6.9b, 6.9d and 6.9f. The dependence of the observable on the top quark mass is modelled by a linear fit.

As a vadidation, the estimated mean from the Gaussian fit of the nominal value of top mass MC sample is used to extract the top quark mass for every variable. The resulting top measurements are as $m_{\text{top}} = 172.1 \pm 0.3$ GeV for m_{T2}, $m_{\text{top}} = 172.2 \pm 0.2$ GeV for $m_{\text{T2}\perp}$ and $m_{\text{top}} = 172.3 \pm 0.3$ GeV for $m_{\ell b}$ where the expected value is 172.5 GeV. It is shown that the biases of observable used in the measurements are small with 0.4 GeV for m_{T2}, 0.3 GeV for $m_{\text{T2}\perp}$ and 0.2 GeV for $m_{\ell b}$. This means that the method is reasonable to measure the top quark mass. These deviations would be taken into account to determine the top quark mass in data.

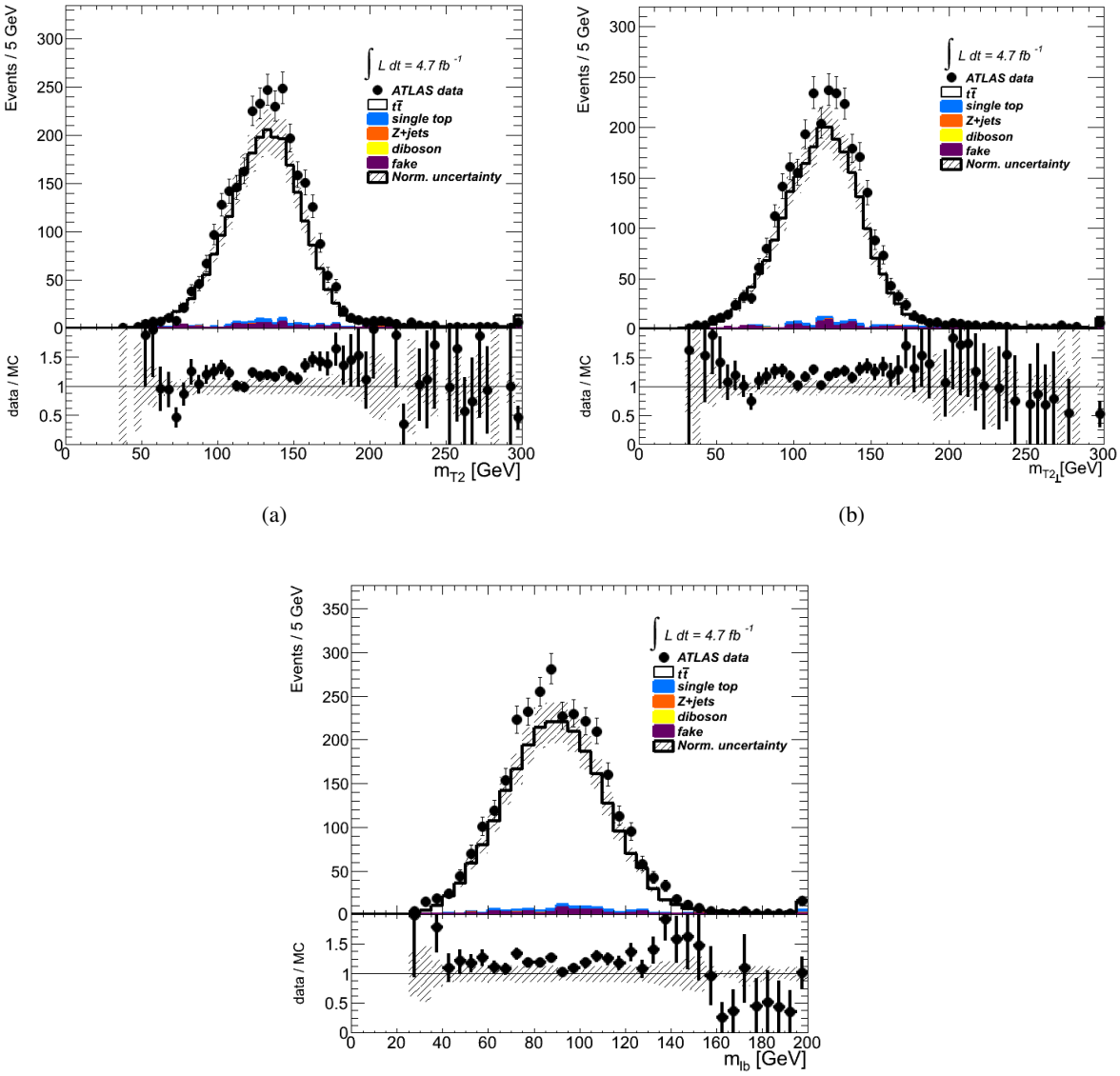

(a) (b)

(c)

Figure 6.8: Distributions observed in data together with the signal and background predictions after the standard selection, (a) for m_{T2}, (b) for $m_{\mathrm{T2}\perp}$, and (c) for $m_{\ell b}$

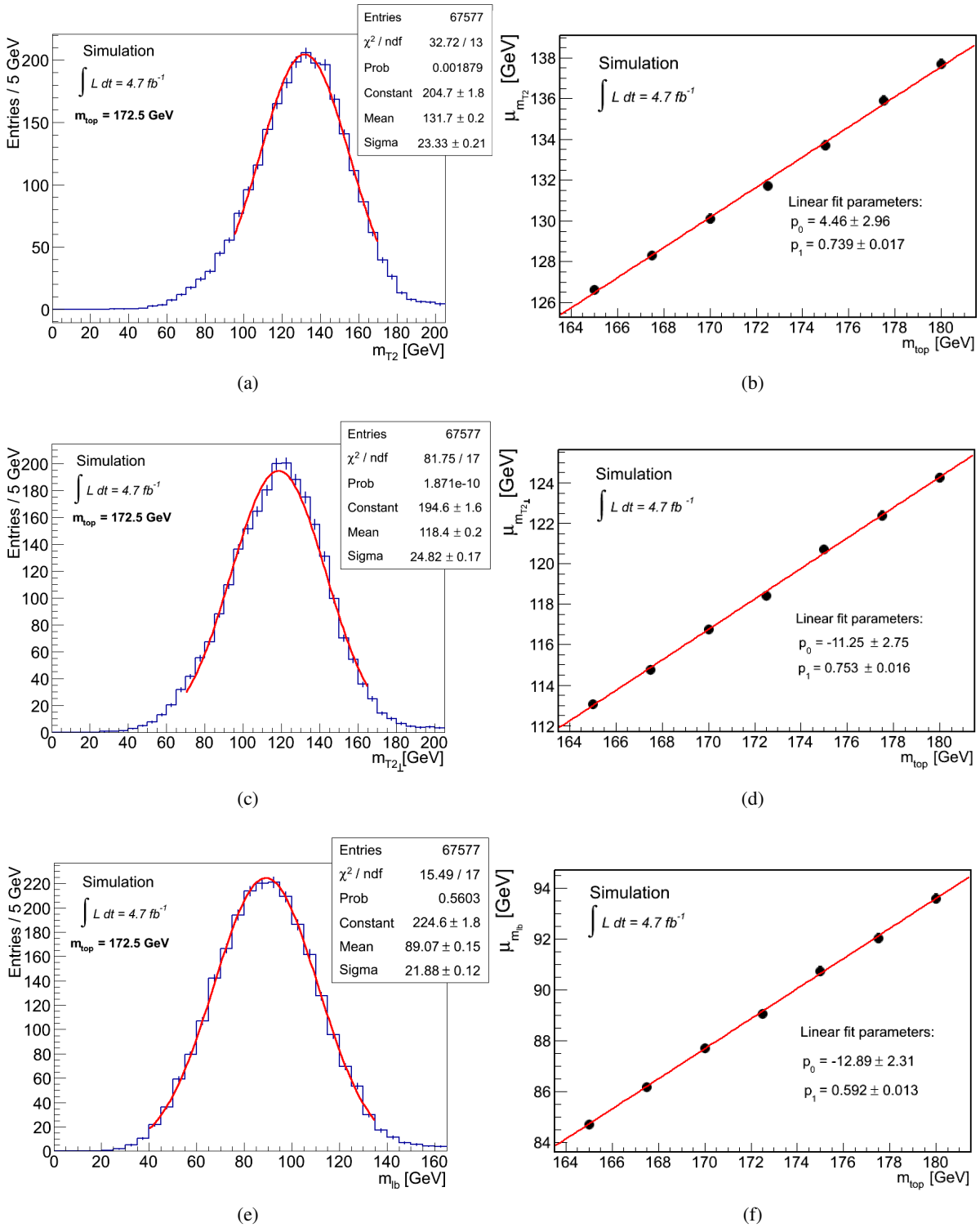

Figure 6.9: Fits of the central mass of MC sample distribution (a, c, and e) and calibration curves (b, d, and f) corresponding to the m_{T2}, $m_{\mathrm{T2}\perp}$ and $m_{\ell b}$, respectively after the standard selection.

Results and systematic uncertainties

The repeated Gaussian fit is applied for the m_{T2}, $m_{\mathrm{T2}\perp}$ and $m_{\ell b}$ distributions in data as displayed in Figure 6.10a, 6.10c and 6.10c, respectively.

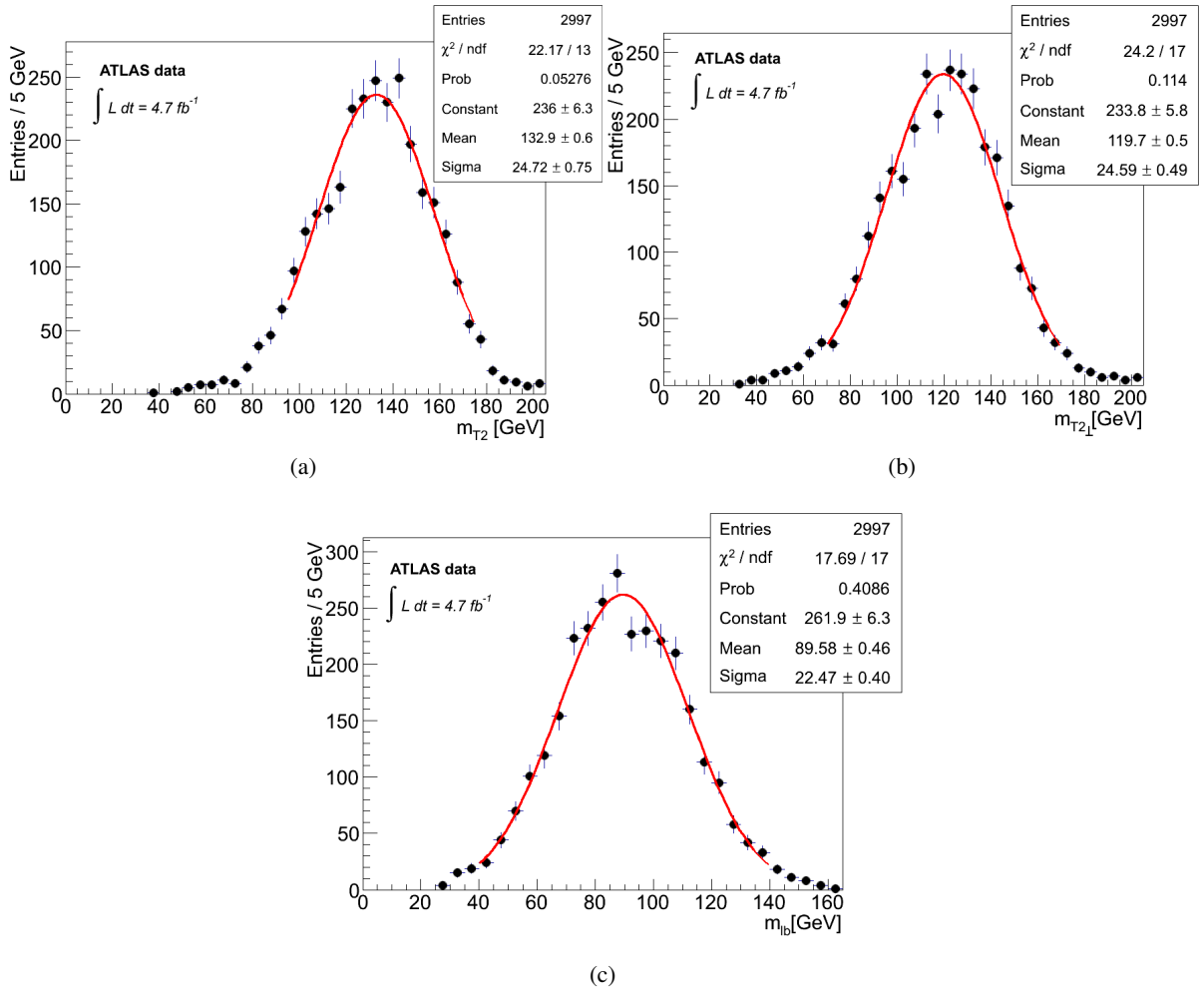

Figure 6.10: Fits of data distribution of m_{T2} (a), $m_{\mathrm{T2}\perp}$ (b) and $m_{\ell b}$ (c) after the standard selection.

The mean values of the fit function are used to calculate the top quark mass for the three chosen variables through the corresponding calibration curves. The fit values and the results of the top quark mass measurements are shown below. The uncertainties shown here are only the statistical uncertainties.

For m_{T2}:	$\mu_{m_{T2}}$ = 132.9 ± 0.6 GeV	m_{top}= 173.6 ± 0.9 GeV
For $m_{\mathrm{T2}\perp}$:	$\mu_{m_{T2\perp}}$ = 119.7 ± 0.5 GeV	m_{top}= 173.8 ± 0.7 GeV
For $m_{\ell b}$:	$\mu_{m_{\ell b}}$ = 89.6 ± 0.5 GeV	m_{top}= 173.2 ± 0.8 GeV

The systematic uncertainties of the baseline analysis are calculated as explained in Chapter 5 and summarised in Table 6.2. A detailed breakdown of the systematic components of JES, b-tagging, muon, electron, missing transverse momentum and normalisation are given in Appendix B.

Table 6.2: Systematic uncertainties of the base analysis

Source	Uncertainty (GeV)		
	m_{T2}	$m_{\mathrm{T2}\perp}$	$m_{\ell b}$
JES	1.1	1.0	0.9
b-JES	0.9	0.8	0.7
JER	0.1	0.4	0.4
JRE	< 0.1	< 0.1	< 0.1
b-tagging	0.3	0.3	0.5
Muons	< 0.1	< 0.1	< 0.1
Electrons	0.1	0.2	< 0.1
Missing transverse momentum	< 0.1	< 0.1	< 0.1
Method calibration	0.1	0.1	0.1
Normalisation	0.1	0.1	0.1
ISR/FSR	0.7	0.7	0.5
UE	< 0.1	< 0.1	< 0.1
CR	0.2	0.4	0.2
Hadronisation	< 0.1	0.3	0.3
MCGen or Ren/Fac	0.5	0.6	0.3
Total systematic uncertainty	1.7	1.8	1.5
Total uncertainty	1.9	1.9	1.7

One can see that the main contributions of the uncertainties are the JES systematics, the b-JES, ISR/FSR, MCGen or Ren./Fac., *b*-tagging and JER systematics for all variables considered in the study. Figure 6.11 performs the weight (ω_i) of each uncertainty component (σ_i) to the total uncertainty (σ_{total}).

$$\omega_i = \frac{\sigma_i^2}{\sigma_{total}^2} \times 100\%$$

The JES value is the most dominant component, weighing nearly 34% (m_{T2}) and 28% ($m_{\mathrm{T2}\perp}$ and $m_{\ell b}$) of the total uncertainty, followed by the b-JES with 22% (m_{T2}), 18% ($m_{\mathrm{T2}\perp}$) and 17% ($m_{\ell b}$), respectively.

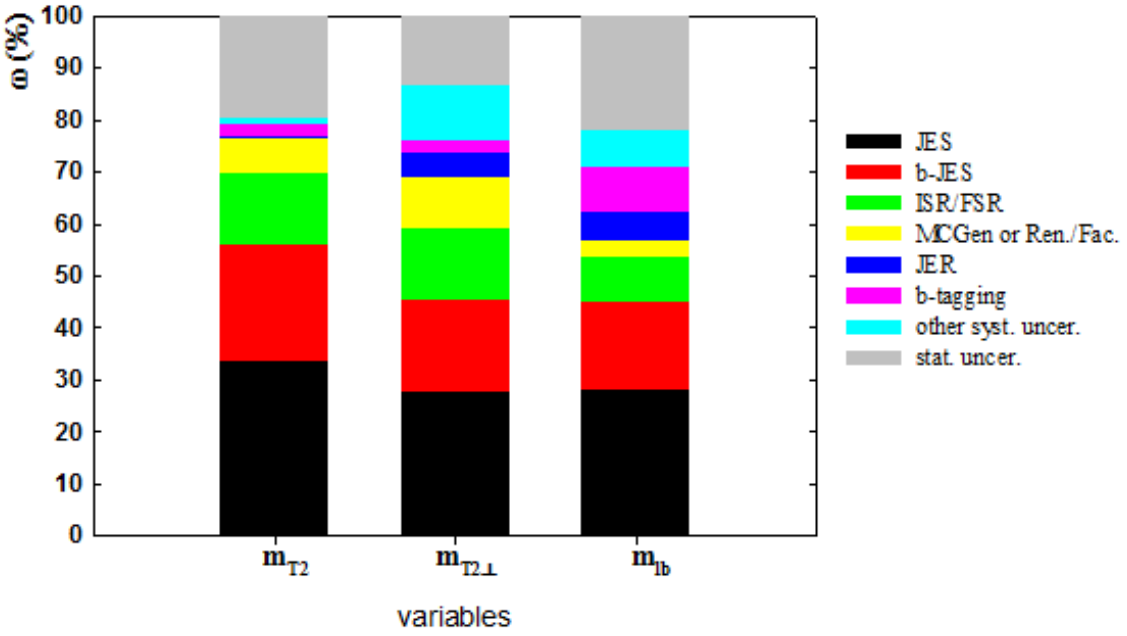

Figure 6.11: Weight distributions of uncertainty components in the baseline analysis.

6.4 Analysis with optimised selection

In order to minimise the uncertainties of the measurements, extra cuts are applied. This section presents the results of the analysis when choosing a new working point for MV1 corresponding to a *b*-tagging efficiency of 85% and an extra cut on p_{T}^{jet}.

Selection

The same selection as the baseline analysis is applied, except that the *b*-tagging efficiency is modified to an efficiency of 85% and a stronger cut on p_{T}^{jet} is applied. The optimal extra cut value on p_{T}^{jet} is determined by the optimised analysis introduced in subsection 4.3.3. The p_{T}^{jet} value is scanned from the baseline cut of 25 GeV to 50 GeV in steps of 5 GeV and then chosen based on the optimal value of total uncertainty. The values of systematic and total uncertainties from the scan are listed in Appendix B. From the results based on the scanning, a cut $p_{\mathrm{T}}^{jet} > 45$ GeV is chosen (see Figure 6.12).

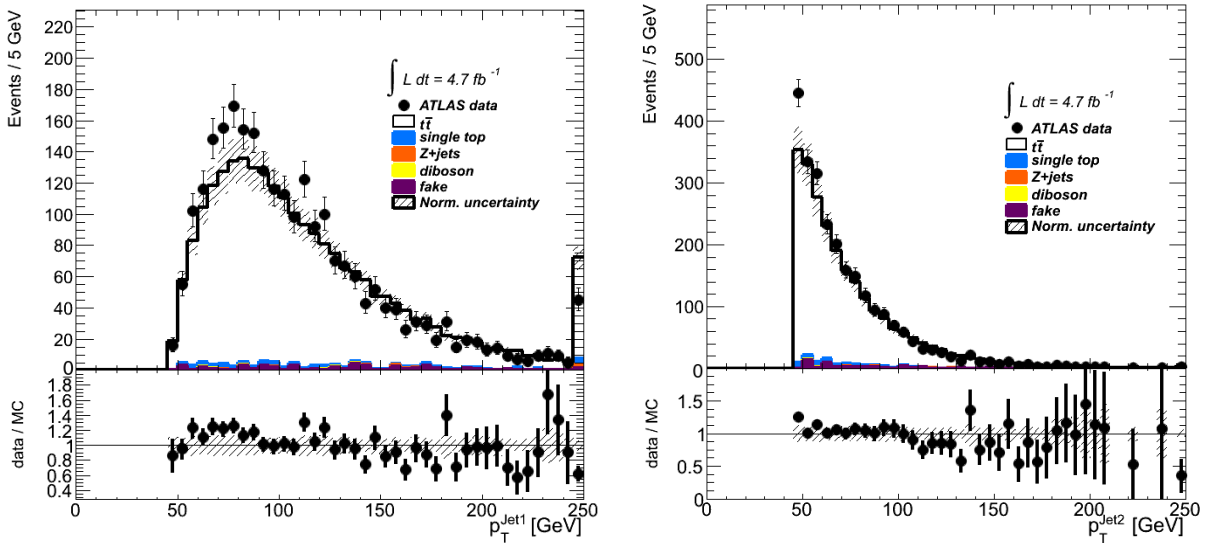

(a) (b)

Figure 6.12: The distributions of the highest (a) and second highest (b) p_{T} b-tagged jets after optimised selection. Histograms show the comparison between data and the expectation from MC simulation and the data-driven estimation of fakes distribution in Section 4.1. The hatched area displays the normalisation uncertainty including signal, background and luminosity uncertainties. The rightmost bin in the plots contains the overflow.

Data and MC samples

The events yield after applying the optimisation cuts are shown in Table 6.3. Note that only statistical uncertainties are shown in the Table. The observed events yield using the additional cuts are about 500 events smaller than the baseline analysis, thus increasing the statistical uncertainty of the measurements.

Table 6.3: Events yield after the optimisation selection

Name	Events
$t\bar{t}$ signal	2291 ± 229
Single top	58.7 ± 5.9
Z + jets	7.6 ± 3.0
Diboson	3.7 ± 1.4
Fakes	39 ± 21
Total expected events	2400 ± 231
Observed events	2523

Similarly to the baseline analysis, the agreement between data and MC simulation for the three variables is shown in Figure 6.13. One can see that the m_{T2}, $m_{\mathrm{T2}\perp}$ and $m_{\ell b}$ distributions with the optimised selection describe the agreement between data and the expectation from MC simulation much better than that of the standard selection, which is attributed to better understanding of the higher efficiency b-tagging point when requiring two b-tagged jets.

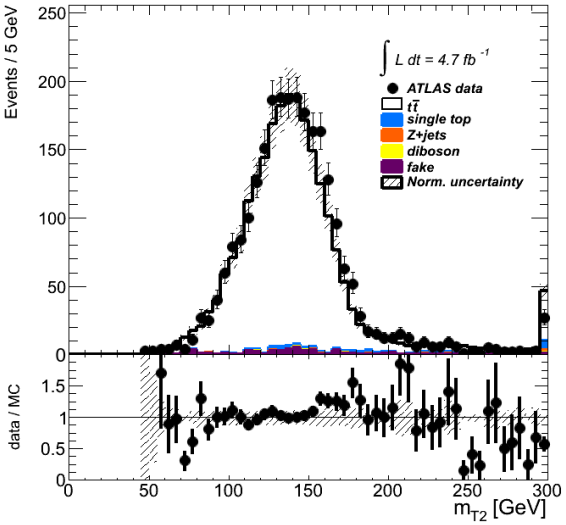

(a)

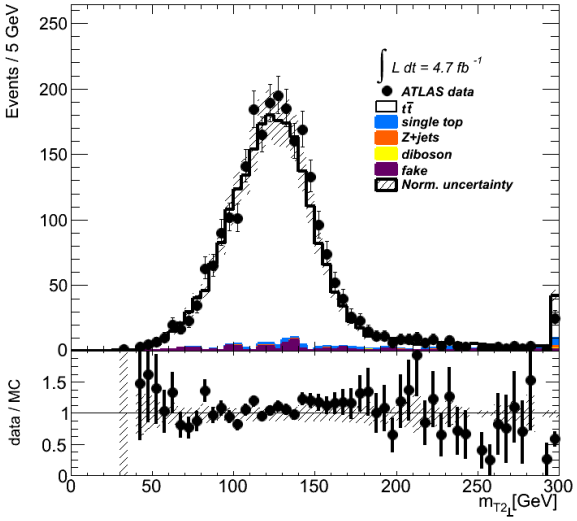

(b)

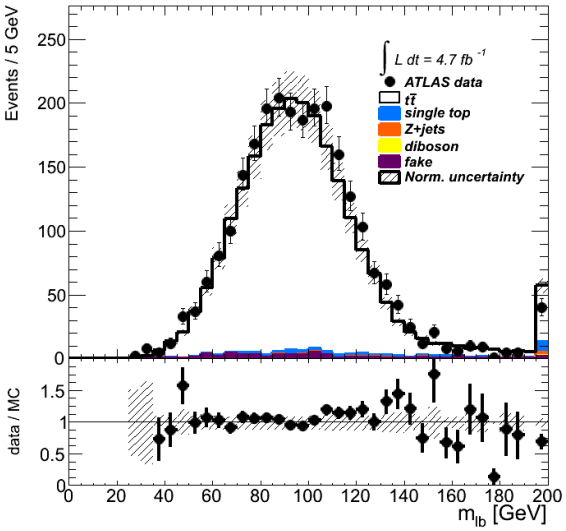

(c)

Figure 6.13: Data together with MC simulation of the m_{T2} (a), $m_{\mathrm{T2}\perp}$ (b) and $m_{\ell b}$ (c) distributions after optimised selection.

Fits and calibration curves

The repeated Gaussian fit is applied for every distribution of the MC simulation (Appendix C) as well as data (Figure 6.14a, 6.14c and 6.14e) and yields the fit values estimated. The calibration curve corresponding to each variable is created from the MC simulation and are plotted in Figure 6.14b, 6.14d and 6.14f.

Results and systematic uncertainties

The measurements of the top quark mass are performed using the optimised selection and calibration curves, obtaining the following top quark mass values. The uncertainties shown here are only the statistical uncertainties.

For m_{T2}: $\mu_{m_{\mathrm{T2}}} = 138.6 \pm 0.7$ GeV $m_{\mathrm{top}} = 175.1 \pm 0.9$ GeV
For $m_{\mathrm{T2}\perp}$: $\mu_{m_{\mathrm{T2}\perp}} = 124.3 \pm 0.6$ GeV $m_{\mathrm{top}} = 174.1 \pm 0.8$ GeV
For $m_{\ell b}$: $\mu_{m_{\ell b}} = 94.4 \pm 0.5$ GeV $m_{\mathrm{top}} = 174.1 \pm 0.9$ GeV

The systematic uncertainties using the new selection are shown in Table 6.4. A more detail systematic components can be found in Appendix B. Most uncertainties of the systematic components are reduced, compared to the baseline analysis, particularly the object systematics related to jets such as JES, b-JES, JER and b-tagging and $t\bar{t}$ production modelling. This leads to a considerable decrease of the total systematic uncertainty for each observable.

Table 6.4: Systematic uncertainties of the analysis with the optimisation cuts

Source	Uncertainty (GeV)		
	m_{T2}	$m_{\mathrm{T2}\perp}$	$m_{\ell b}$
JES	1.1	0.8	0.8
b-JES	0.9	0.8	0.6
JER	0.5	0.5	0.3
JRE	0.2	< 0.1	0.1
b-tagging	0.1	0.1	0.2
Muons	< 0.1	0.1	< 0.1
Electrons	< 0.1	0.1	< 0.1
Missing transverse momentum	< 0.1	0.1	< 0.1
Method calibration	0.1	0.1	0.1
Normalisation	0.1	0.1	0.1
ISR/FSR	0.3	0.3	0.2
UE	< 0.1	< 0.1	< 0.1
CR	0.1	0.1	< 0.1
Hadronisation	0.3	0.2	0.5
MCGen or Ren/Fac	0.4	0.4	0.2
Total systematic uncertainty	1.6	1.4	1.3
Total uncertainty	1.9	1.6	1.5

Figure 6.15 displays the weight distributions in percentage of systematic components to the total uncertainty of top mass measurements with the optimised selection. It can be seen that the JES and b-JES systematics contribute the most for all variables applied in the study. They have the same weight values

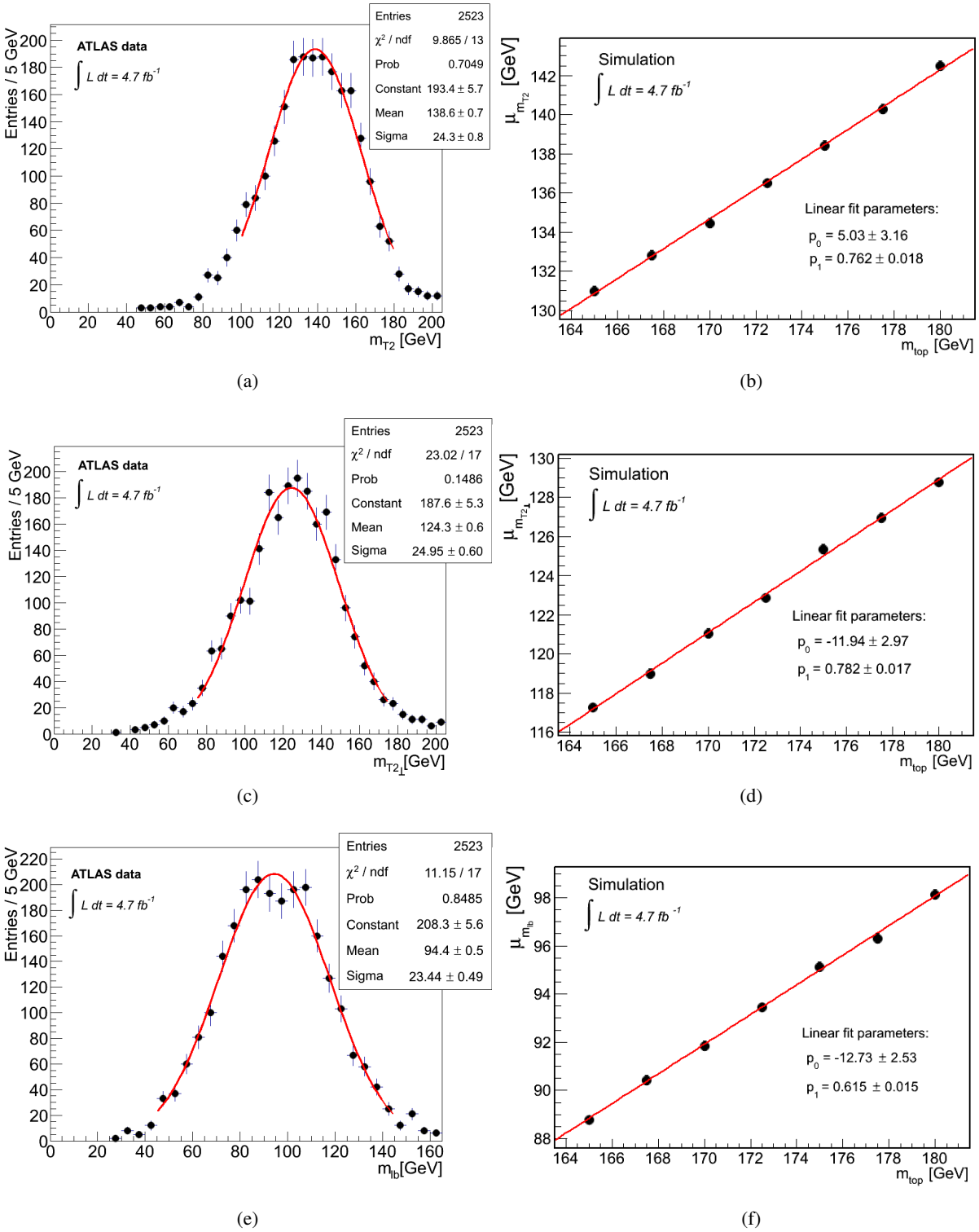

Figure 6.14: Fits in data (a, c, e) and calibration curves (b, d, f) of the m_{T2}, $m_{\mathrm{T2}\perp}$ and $m_{\ell b}$ distributions after optimised selection.

to the total uncertainty as the baseline analysis for m_{T2}, with 34% and 22% of the weight, respectively. The JES and b-JES of the $m_{T2\perp}$ variable share the same weight of 25%, while 28% and 16% are the weight values of JES and b-JES for the $m_{\ell b}$.

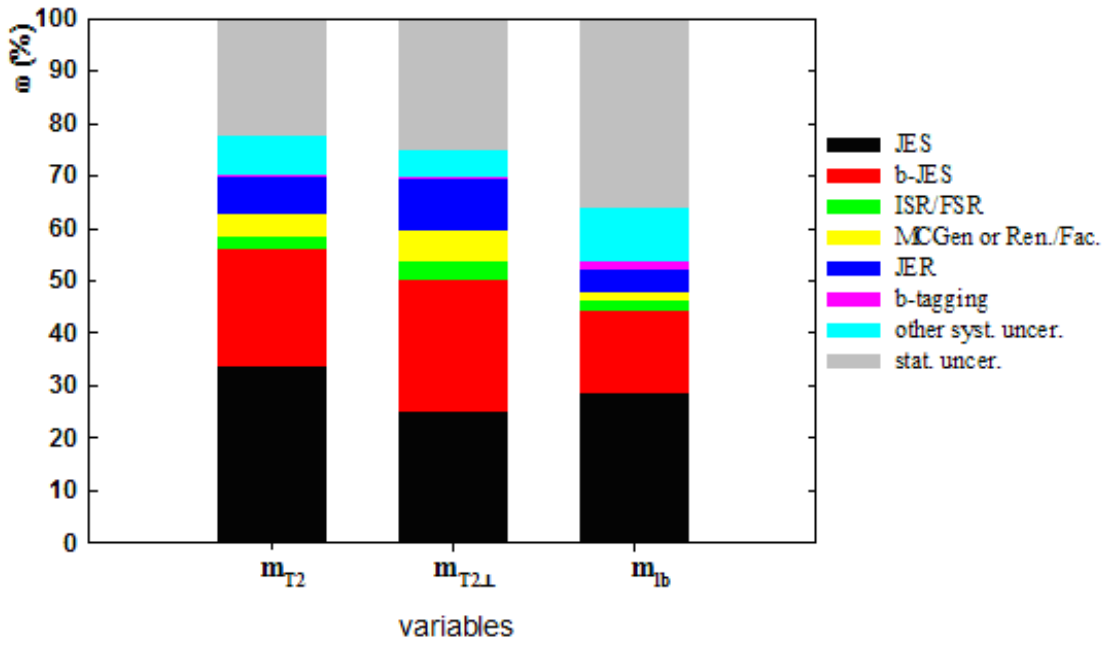

Figure 6.15: Weight distribution of uncertainty components in the optimised analysis.

6.5 Final results

In this study, three variables of the m_{T2}, $m_{T2\perp}$, and $m_{\ell b}$ are used to measure the top quark mass with two selections.

The baseline analysis with the standard selection obtained a top quark mass of:

For m_{T2}: m_{top}= 173.6 ± 0.9 (stat.) ± 1.7 (syst.) GeV
For $m_{T2\perp}$: m_{top}= 173.8 ± 0.7 (stat.) ± 1.8 (syst.) GeV
For $m_{\ell b}$: m_{top}= 173.2 ± 0.8 (stat.) ± 1.5 (syst.) GeV

The optimised analysis measured a top quark mass applying the optimisation cuts, leading to the following results:

For m_{T2}: m_{top}= 175.1 ± 0.9 (stat.) ± 1.6 (syst.) GeV
For $m_{T2\perp}$: m_{top}= 174.1 ± 0.8 (stat.) ± 1.4 (syst.) GeV
For $m_{\ell b}$: m_{top}= 174.1 ± 0.9 (stat.) ± 1.3 (syst.) GeV

As expected from the optimisation cuts, the systematic uncertainties in the optimised analysis are reduced. The relative reduction of the systematic uncertainty is 5.9% for m_{T2}, 22.2% for $m_{T2\perp}$ and 13.3%

for $m_{\ell b}$, compared to the baseline measurement. However, the relative importance of the statistical uncertainties in this case slightly increase, for example, increasing 0.1 GeV for $m_{\mathrm{T2}\perp}$ and $m_{\ell b}$.

Compared to the ATLAS result in summer 2012, given $m_{\mathrm{top}} = 175.2 \pm 1.6$ (stat.) ± 3.0 (syst.) GeV using the mean of the m_{T2} variable in the $e^{\pm}\mu^{\mp}$ channel [7], both the statistical and systematic uncertainties are reduced by approximately a factor of 2 thanks to some improvements. This study also uses the $e^{+}e^{-}$ and $\mu^{+}\mu^{-}$ modes. On the m_{top} analysis side, all MC variations samples used to create the calibration curve are now processed with the ATLAS full simulation instead of ATLAS fast simulation. This leads to a better precision in computing the mean values of the fit on variable distributions as well as obtaining the top-quark mass. Moreover, a change of the nominal signal MC from MC@NLO + HERWIG generator to POWHEG + PYTHIA generator with more improvement of some observed quantities gives an effect on the uncertainty of m_{top}. Due to this change, samples estimating systematic uncertainties are more consistent with the nominal MC sample, for instance UE, CR and MCGen systematic variations. The JES systematics is calculated more precisely by a parameterisation with different components, as described in Section 5.1, leading to a decrease of systematic uncertainty.

During the time of the study, a new ATLAS top-quark mass measurement was released as preliminary note [64]. This measurement used $m_{\ell b}$ estimator with the template method in the dilepton decay channel, giving a value of $m_{\mathrm{top}} = 173.09 \pm 0.64$ (stat.) ± 1.50 (syst.) GeV. Contributting in this measurement, the results in this study were used to check the validity of the top mass result in the ATLAS measurement, especially the top-quark mass for the $m_{\ell b}$ variable, giving a compatibility with the ATLAS result. In addition, this study also highlights some optimisation selections, for example using a higher b-tagging efficiency or selecting jets with higher p_{T}, which can be applied for further reduce the uncertainty of the top-quark mass measurement for the paper publication.

CHAPTER 7

Conclusions

This study used three different variables (m_{T2}, $m_{\mathrm{T2}\perp}$ and $m_{\ell b}$) to measure the top quark mass in the $t\bar{t}$ →dilepton decay channel with 4.7 fb^{-1} ATLAS data at $\sqrt{s}$ = 7 TeV collected in 2011. The method applied for the measurements was the calibration curve method.

The measurement is dominated by the systematic uncertainties, which mostly come from contributed systematics related to jet objects such as JES and b-JES.

An optimised selection did not generally have a big impact on the total uncertainty for m_{T2}, although there were some rearrangements in the contribution of the systematic components. On the other hand, the additional cuts led to a quite significant decrease of the total systematic uncertainty for $m_{\mathrm{T2}\perp}$ and $m_{\ell b}$. However, the statistical uncertainty is slightly increased due to the more stringent cuts.

Among the three variables used, $m_{\ell b}$ yields the result with the smallest uncertainty because this variable does not require a full event reconstruction. A total uncertainty of 1.5 GeV is the lowest value achieved in the study, by using this variable, which is very similar to the ATLAS measurement in dileptonic decay channel using this variable in 2013. [64].

In order to improve the accuracy of the measurements further, more studies can be considered.

- For m_{T2}, the Gaussian fit function chosen in the analysis may not be appropriate to describe the distributions of this variable. Therefore, a more suitable choice of a fit function could improve the final result of the measurement.
- An improved understanding of JES and b-JES calibration procedure will lead to a reduction of the systematic uncertainty.
- The data at $\sqrt{s}$ = 8 TeV collected in 2012 by the ATLAS detector and improvements of MC simulation samples should help to reduce the uncertainty values of the top quark mass measurement.

APPENDIX A

Basic concepts

Transverse momentum

The transverse momentum $\vec{p}_{\mathrm{T}}$ is defined as the momentum determined in the transverse plane including x and y axes. It is only composed of the x and y components of the momentum: $\vec{p}_{\mathrm{T}} = \begin{pmatrix} p_x \\ p_y \\ 0 \end{pmatrix}$.

Transverse energy

The transverse energy E_{T} of an object is determined by: $E_{\mathrm{T}} = \sqrt{\mathrm{m}^2 + (\vec{p}_{\mathrm{T}})^2}$.

Missing transverse momentum

Missing transverse momentum $\vec{p}_{\mathrm{T}}^{miss}$ is the momentum lost due to the limitation of apparatus for the measurement as well as undetected particles. Because of momentum conservation, the missing transverse momentum is the vectorial sum of the transverse momenta of all detected particles and objects. In this study, the missing transverse momentum is the vectorial sum of the transverse momenta of all leptons and jets: $\vec{p}_{\mathrm{T}}^{miss} = -(\vec{\mathrm{p}}_{\mathrm{T}}^{\mathrm{leptons}} + \vec{\mathrm{p}}_{\mathrm{T}}^{\mathrm{jets}})$.

Missing transverse energy

Missing transverse energy E_{T}^{miss} is the energy of an undetected particle in the transverse plane. The undetected particle in this measurement is due to neutrinos with $m_\nu \approx 0$; therefore, missing transverse energy is defined as: $E_{\mathrm{T}}^{miss} = \sqrt{\mathrm{m}^2 + (\vec{p}_{\mathrm{T}}^{miss})^2} \Rightarrow E_{\mathrm{T}}^{miss} \approx |\vec{p}_{\mathrm{T}}^{miss}|$.

Invariant mass

Invariant mass of two objects a and b is determined by:

$$
\begin{aligned}
m_{ab}^2 &= \tilde{p}_{ab}^2 = (\tilde{p}_a + \tilde{p}_b)^2 \\
&= (E_a + E_b)^2 - (\vec{p}_a - \vec{p}_b)^2 \\
&= E_a^2 + E_b^2 + 2E_aE_b - \vec{p}_a^2 - \vec{p}_b^2 - 2\vec{p}_a \cdot \vec{p}_b \\
&= m_a^2 + m_b^2 + 2(E_aE_b - \vec{p}_a \cdot \vec{p}_b)
\end{aligned}
$$

The scalar sum of all selected leptons and jets momenta

The scalar sum of all selected leptons and jets momenta (H_{T}) of a dilepton event candidate is defined:

$$H_{\mathrm{T}} = p_T^{lep1} + p_T^{lep2} + p_T^{jet1} + p_T^{jet2}$$

where: p_T^{lep1}, p_T^{lep2}, p_T^{jet1} and p_T^{jet2} are the module of the transverse momentum of the first lepton, second lepton, leading jet, and sub-leading jet respectively.

APPENDIX **B**

Tables of systematic component values

Systematic uncertainties at different binning range (n bins) of the baseline analysis

nbins	Systematic uncertainty (GeV)			Total uncertainty (GeV)		
	m_{T2}	$m_{\mathrm{T2}\perp}$	$m_{\ell b}$	m_{T2}	$m_{\mathrm{T2}\perp}$	$m_{\ell b}$
7	1.72	1.80	1.58	1.93	2.00	1.80
8	1.80	1.81	1.54	1.96	1.97	1.74
9	1.89	1.78	1.46	2.02	1.91	1.65
10	1.96	1.79	1.51	2.08	1.92	1.69

Systematic uncertainties at different p_{T}^{jet} cuts of the optimised analysis

p_{T}^{jet} cut values (GeV)	Systematic uncertainty (GeV)			Total uncertainty (GeV)		
	m_{T2}	$m_{\mathrm{T2}\perp}$	$m_{\ell b}$	m_{T2}	$m_{\mathrm{T2}\perp}$	$m_{\ell b}$
25	1.69	1.58	1.36	1.85	1.70	1.52
30	1.64	1.71	1.35	1.80	1.83	1.52
35	1.91	1.45	1.35	2.06	1.60	1.53
40	1.81	1.35	1.35	2.00	1.54	1.56
45	1.64	1.37	1.25	1.87	1.58	1.52
50	1.73	1.47	1.42	1.99	1.68	1.72

JES systematic components

Source	Uncertainty with the standard selection (GeV)			Uncertainty with the optimisation cuts (GeV)		
	m_{T2}	$m_{\mathrm{T2}\perp}$	$m_{\ell b}$	m_{T2}	$m_{\mathrm{T2}\perp}$	$m_{\ell b}$
Detector NP1	0.557	0.504	0.413	0.637	0.505	0.452
Detector NP2	0.005	0.006	0.007	0.046	0.010	0.006
Mixed NP1	0.048	0.002	0.006	0.051	0.032	0.003
Mixed NP2	0.092	0.079	0.060	0.052	0.035	0.016
Modelling NP1	0.376	0.368	0.218	0.303	0.256	0.189
Modelling NP2	0.175	0.152	0.104	0.134	0.138	0.172
Modelling NP3	0.153	0.166	0.145	0.145	0.180	0.134
Modelling NP4	0.015	0.004	0.004	0.050	0.016	0.021
Statistical NP1	0.099	0.023	0.039	0.048	0.032	0.019
Statistical NP2	0.007	0.031	0.036	0.020	0.026	0.008
Statistical NP3	0.077	0.094	0.103	0.077	0.088	0.099
EtaIntercalibrationmodelling	0.438	0.401	0.463	0.535	0.362	0.366
EtaIntercalibration_TotalStat	0.060	0.015	0.100	0.138	0.061	0.089
JES_Flavour composition	0.027	0.025	0.021	0.043	0.036	0.055
JES_Flavour responese	0.023	0.018	0.038	0.042	0.010	0.036
Pile-up offset (μ term)	0.680	0.593	0.490	0.581	0.385	0.448
Pile-up offset (NPV term)	0.034	0.027	0.028	0.047	0.035	0.010
Relative non-closure MC	0.073	0.075	0.055	0.034	0.063	0.064
Single Particle hight p_{T}	0.076	0.031	0.026	0.028	0.001	0.015
Total	1.097	0.989	0.859	1.098	0.821	0.801

b-tagging systematic components

Source	Uncertainty with the standard selection (GeV)			Uncertainty with the optimisation cuts (GeV)		
	m_{T2}	$m_{\mathrm{T2}\perp}$	$m_{\ell b}$	m_{T2}	$m_{\mathrm{T2}\perp}$	$m_{\ell b}$
BtagB	0.262	0.277	0.373	0.014	0.028	0.135
BtagC	0.007	0.020	0.009	0.040	0.030	0.004
BtagL	0.010	0.034	0.015	0.031	0.105	0.171
BtagStatB	0.204	0.180	0.300	0.046	0.017	0.003
BtagStatC	0.022	0.001	0.005	0.265	0.014	0.043
BtagStatL	0.063	0.005	0.005	0.007	0.016	0.019
Total	0.339	0.333	0.478	0.075	0.117	0.222

Electron systematic components

Source	Uncertainty with the standard selection (GeV)			Uncertainty with the optimisation cuts (GeV)		
	m_{T2}	$m_{\mathrm{T2}\perp}$	$m_{\ell b}$	m_{T2}	$m_{\mathrm{T2}\perp}$	$m_{\ell b}$
ElTrigS	0.001	0.063	0.004	0.033	0.013	0.024
ElRecIDS	0.037	0.016	0.043	0.006	0.051	0.033
ElES	0.120	0.121	0.061	0.032	0.117	0.014
ElER	0.016	0.059	0.001	0.018	0.019	0.003
Total	0.126	0.150	0.077	0.049	0.130	0.044

Muon systematic components

Source	Uncertainty with the standard selection (GeV)			Uncertainty with the optimisation cuts (GeV)		
	m_{T2}	$m_{\mathrm{T2}\perp}$	$m_{\ell b}$	m_{T2}	$m_{\mathrm{T2}\perp}$	$m_{\ell b}$
MuTrigS	0.030	0.011	0.017	0.033	0.022	0.006
MuRecIDS	0.033	0.011	0.030	0.034	0.068	0.004
MuptS	0.034	0.020	0.013	0.020	0.002	0.020
MuPtR	0.076	0.010	0.005	0.036	0.067	0.0001
Total	0.094	0.027	0.037	0.063	0.098	0.021

E_{T}^{miss} systematic components

Source	Uncertainty with the standard selection (GeV)			Uncertainty with the optimisation cuts (GeV)		
	m_{T2}	$m_{\mathrm{T2}\perp}$	$m_{\ell b}$	m_{T2}	$m_{\mathrm{T2}\perp}$	$m_{\ell b}$
E_{T}^{miss}CellOut	0.041	0.002	0.030	0.011	0.056	0.002
E_{T}^{miss}Pileup	0.030	0.001	0.035	0.039	0.009	0.020
Total	0.051	0.002	0.046	0.040	0.056	0.020

Signal and background normalisation systematic components

Source	Uncertainty with the standard selection (GeV)			Uncertainty with the optimisation cuts (GeV)		
	m_{T2}	$m_{\mathrm{T2}\perp}$	$m_{\ell b}$	m_{T2}	$m_{\mathrm{T2}\perp}$	$m_{\ell b}$
Signal	0.025	0.001	0.011	0.077	0.019	0.044
Fakes	0.030	0.115	0.004	0.075	0.100	0.069
Single top						
t-channel	0.038	0.024	0.004	0.028	0.008	0.012
s-channel	0.013	0.009	0.015	0.018	0.025	0.032
Wt-channel	0.005	0.007	0.013	0.006	0.001	0.102
Z+jets	0.052	0.040	0.060	0.046	0.017	0.017
Diboson	0.022	0.013	0.005	0.022	0.011	0.013
Total	0.080	0.126	0.065	0.124	0.107	0.137

APPENDIX C

Fits at different mass points

All fits of the three variables at different top mass values of MC samples are shown in this Section. The fits with the baseline analysis are displayed in Figure C.1 for m_{T2}, Figure C.2 for $m_{\mathrm{T2}\perp}$ and Figure C.3 for $m_{\ell b}$. Figure C.4, C.5, C.6 perform the fits of m_{T2}, $m_{\mathrm{T2}\perp}$ and $m_{\ell b}$ distributions with the optimised analysis.

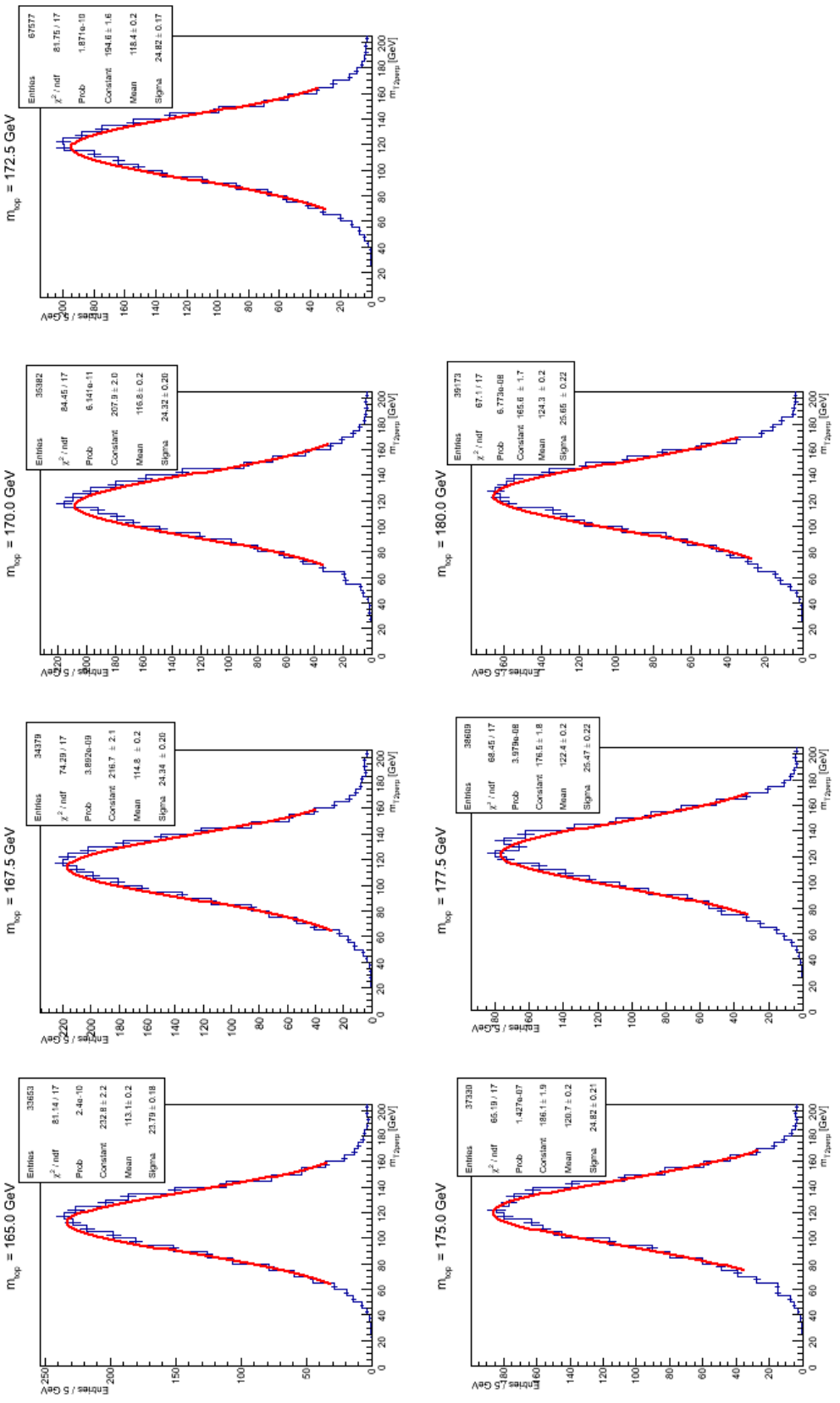

Figure C.1: Fits of the m_{T2} distribution at different input top mass points with the baseline analysis.

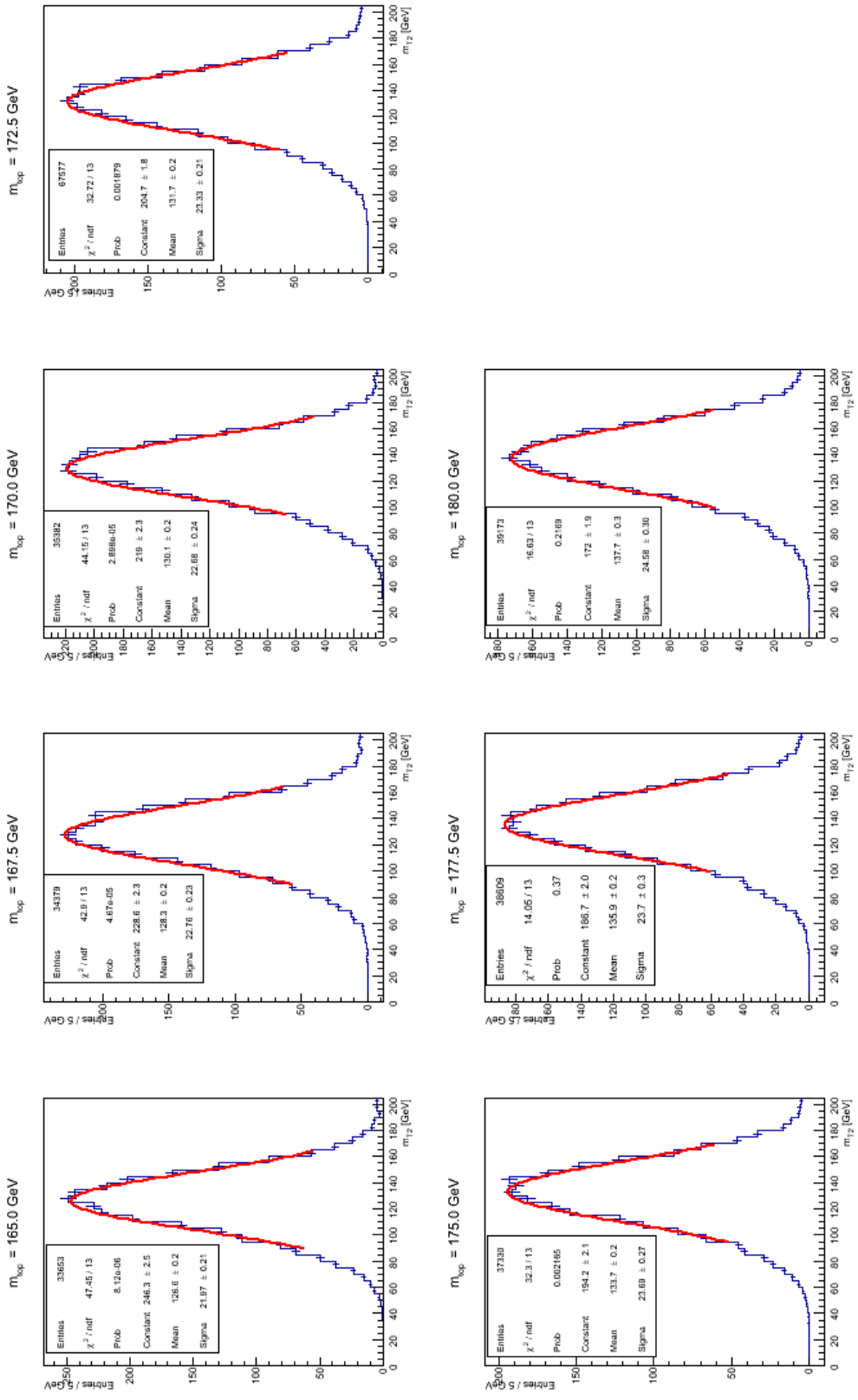

Figure C.2: Fits of the $m_{\mathrm{T2}\perp}$ distribution at different input top mass points with the baseline analysis.

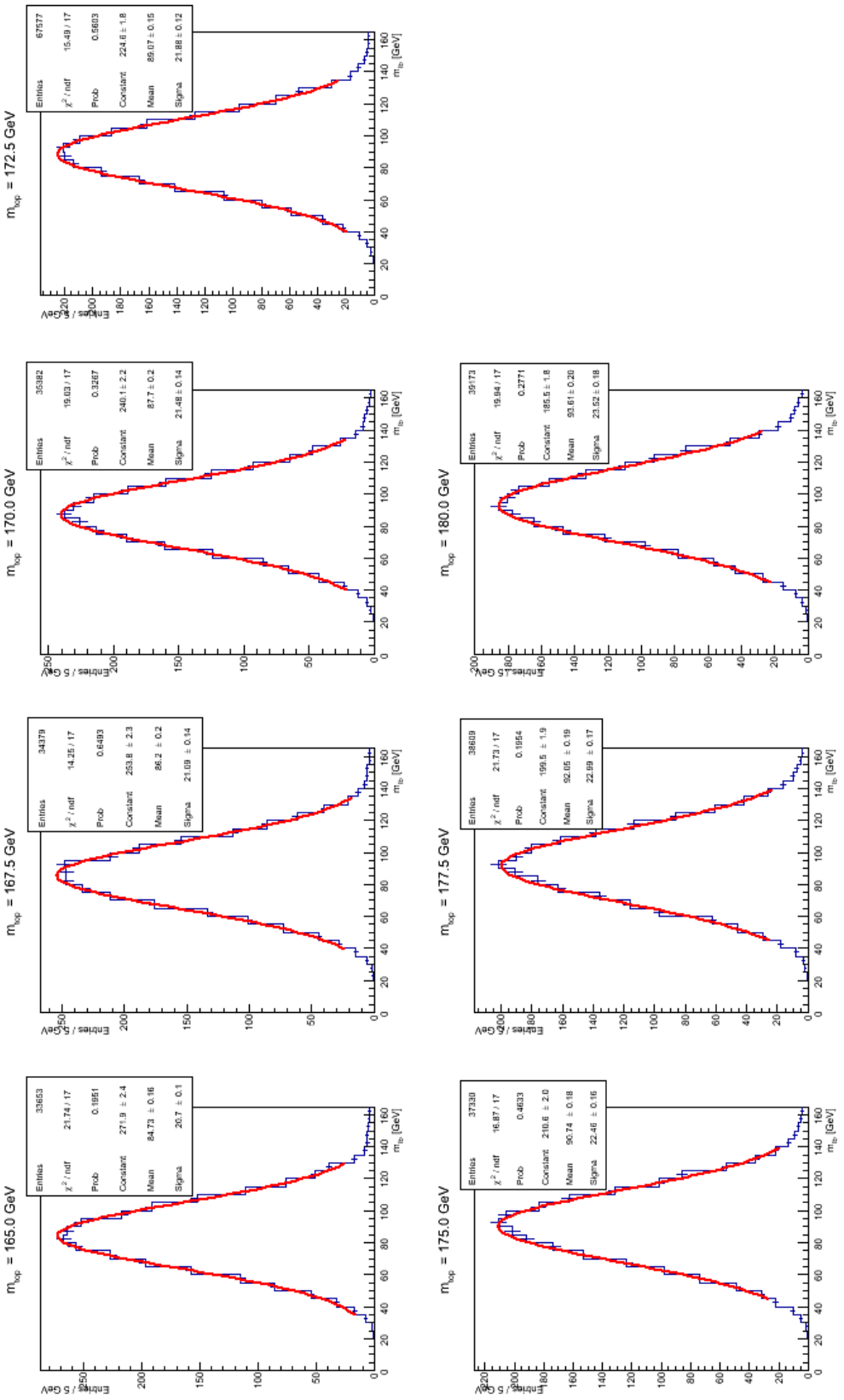

Figure C.3: Fits of the $m_{\ell b}$ distribution at different input top mass points with the baseline analysis.

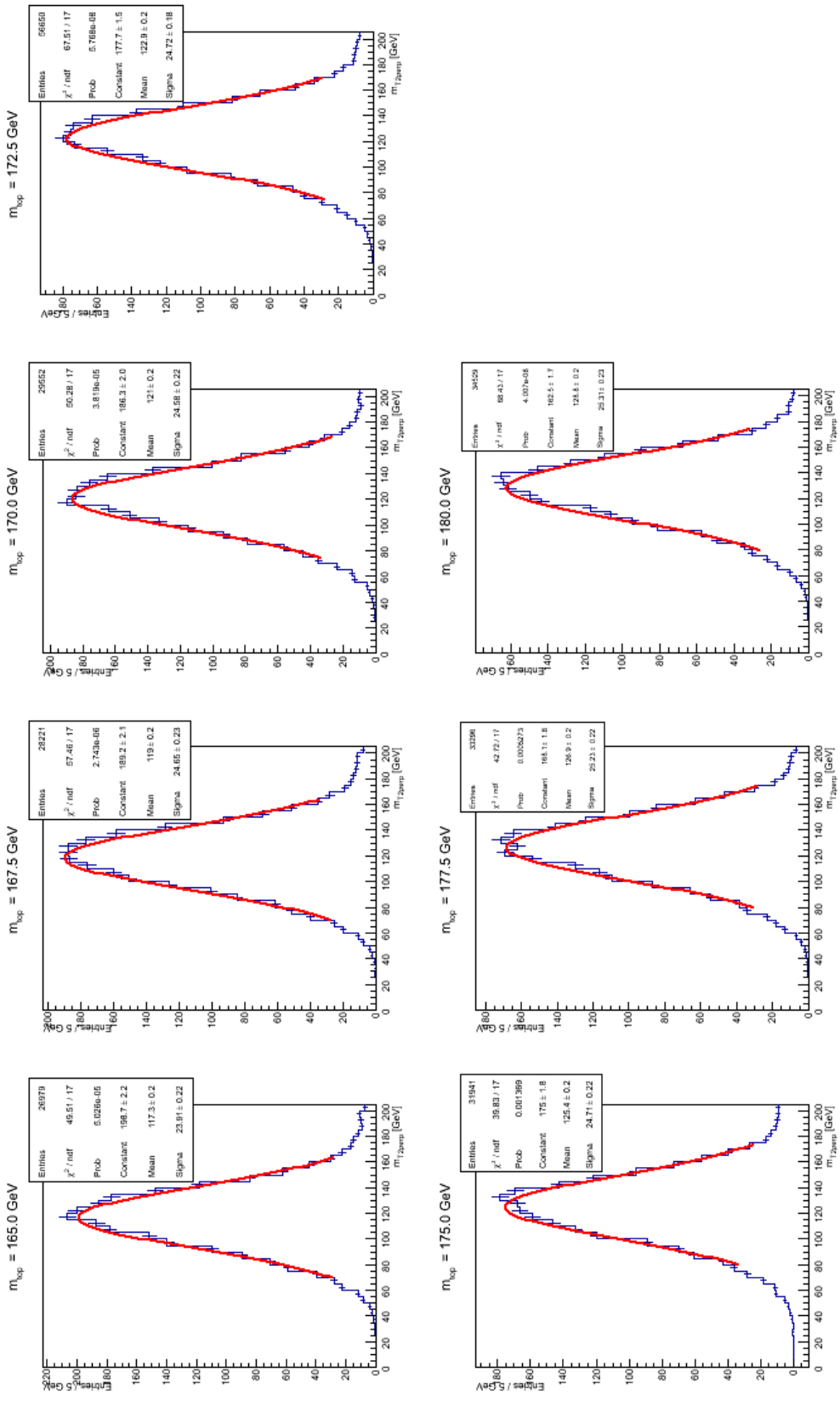

Figure C.4: Fits of the m_{T2} distribution at different input top mass points with the optimised analysis.

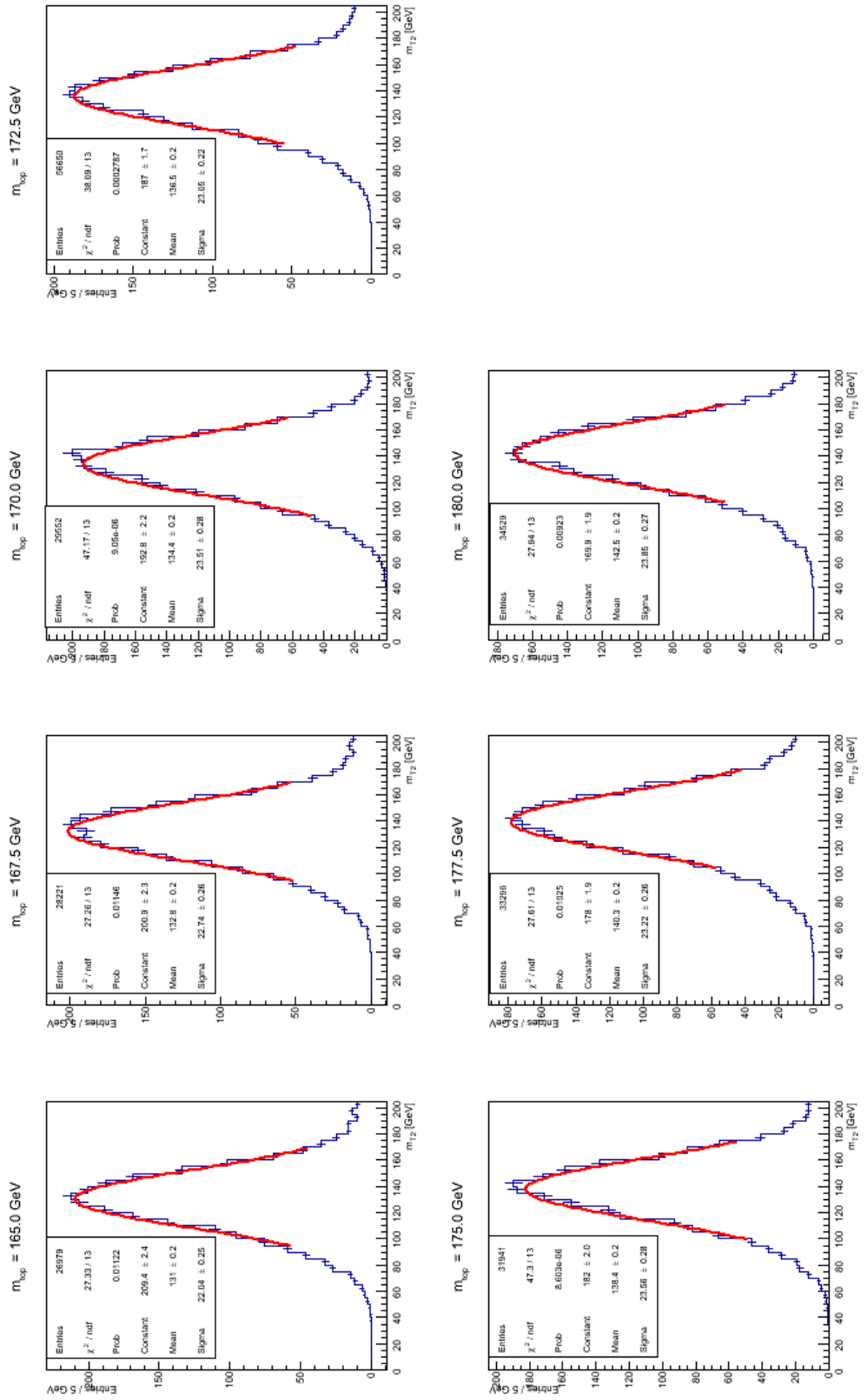

Figure C.5: Fits of the $m_{\mathrm{T2}\perp}$ distribution at different input top mass points with the optimised analysis.

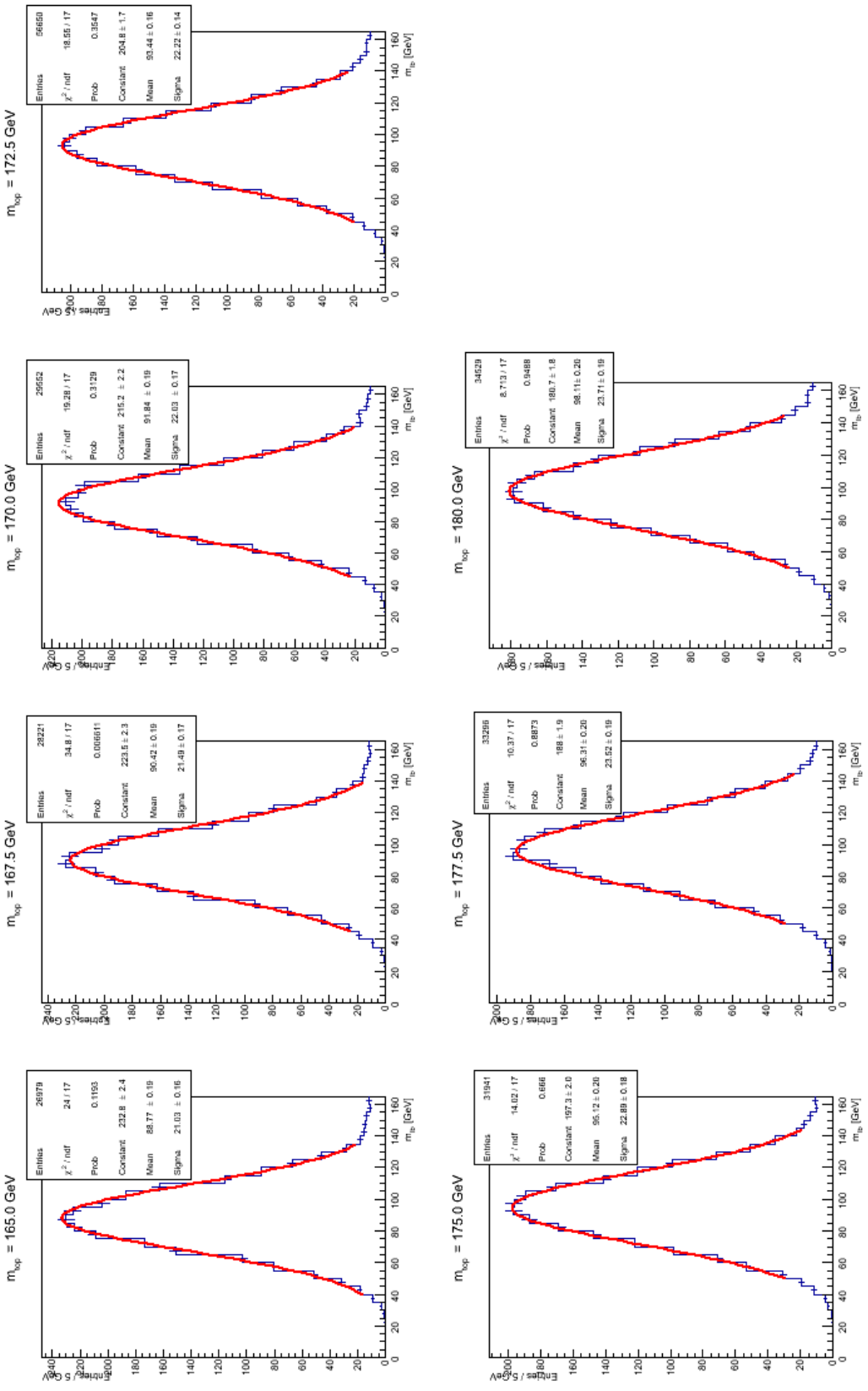

Figure C.6: Fits of the $m_{\ell b}$ distribution at different input top mass points with the optimised analysis.

Bibliography

[1] M. Kobayashi and T. Maskawa,
"CP-Violation in the Renormalisable Theory of Weak Interaction",
Prog. Theor. Phys. Vol. 49 No.2, pp. 652-657 (1973), DOI: 10.1143/PTP.49.652.

[2] CDF Collaboration, F. Abe et al.,
"Observation of Top Quark Production in $p\bar{p}$ Collisions with the Collider Detector at Fermilab",
Phys. Rev. Lett. 74, 2626-2631 (1995), DOI: 10.1103/PhysRevLett.74.2626.

[3] D0 Collaboration, S. Abachi et al., "Observation of the Top Quark",
Phys. Rev. Lett. 74, 2632–2637 (1995), DOI: 10.1103/PhysRevLett.74.2632.

[4] LEP Working Group for Higgs boson searches and ALEPH and DELPHI and L3 and OPAL Collaborations, R. Barate et al., "Search for the Standard Model Higgs Boson at LEP",
Phys.Lett. B565 61-75.CERN-EP-2003-011 (2003), DOI: 10.1016/S0370-2693(03)00614-2, arXiv:hep-ex/0306033.

[5] A. Quadt, "Top quark physics at hadron colliders", *Eur. Phys. J.* C48 (2006),
DOI: 10.1140/epjc/s2006-02631-6, URL: http://arxiv.org/abs/hep-ph/0507207.

[6] CDF-D0 Collaboration, Tevatron Electroweak Working Group, "Combination of CDF and DO results on the mass of the top quark using up to 8.7 fb^{-1} at the Tevatron" (2013),
arXiv:1305.3929[hep-ex].

[7] ATLAS Collaboration,
"Top quark mass measurement in the eμ channel using the m_{T2} variable at ATLAS",
ATLAS-CONF-2012-082, CERN, June 2012.

[8] ATLAS Collaboration, "Measurement of the Top Quark Mass from $\sqrt{s}$ = 7 TeV ATLAS data using a 3-dimensional Template Fit", ATLAS-CONF-2013-046, CERN, May 2013.

[9] CMS Collaboration, "Measurement of the top–quark mass in ttbar events with dilepton final states in pp collisions at $\sqrt{s}$ = 7 TeV", *Eur. Phys. J.* C72, 2202 (2012), arXiv:1209.2393v2.

[10] CMS Collaboration, Chatrchyan et al., "Measurement of the top-quark mass in $t\bar{t}$ events with lepton+jets final states in pp collisions at $\sqrt{s}$=7 TeV", *J. High Energy Phys.* 12.arXiv:1209.2319. CMS-TOP-11-015. CERN-PH-EP-2012-250 (Sept. 2012) 105. 33 p.

[11] A. Barr, C. Lester and P. Stephens, "m_T2: the truth behind the glamour", *J. Phys.* G29 (2003),
DOI: 10.1088/0954-3899/29/10/304, arXiv:hep-ph/0304226.

[12] P. Konar et al., "Superpartner Mass Measurement Technique using 1D Orthogonal Decompositions of the Cambridge Transverse Mass Variable *M_T*2",
Phys.Rev.Lett. 105 (2010) 051802, DOI: 10.1103/PhysRevLett.105.051802,
arXiv:0910.3679 [hep-ph].

[13] D. Griffiths, *Introduction to Elementary Particles*, 1st ed.,
WILEY-VCH Verlag GmbH & Co kGaA, Weinheim, 2008, ISBN: 978-3-527-40601-2.

[14] D. H. Perkins, *Introduction to high energy physics*, 4th ed.,
Addison-Wesley Publishing Company, 2000, ISBN: 9780521621960,
URL: http://books.google.com/books?id=e63cNigcmOUC.

[15] M. J. Herrero, "The Standard Model" (June 1998), arXiv:hep-ph/9812242.

[16] Particle Data Group, J. Beringer et al., "Review of Particle Physics",
Phys.Rev. D86, 010001 (2012), URL: http://pdg.lbl.gov.

[17] P. W. Higgs, "Broken symmetries, massless particles and gauge fields",
Phys.Lett. 12 132 (1964).

[18] P. W. Higgs, "Spontaneous symmetry breakdown without massless bosons",
Phys. Rev. 145 (1966).

[19] W. Bernreuther, "Top quark physics at the LHC", *J. Phys.* G35 (2008),
arXiv:hep-ph/0805.1333.

[20] J. R. Incandela et al., "Status and prospects of top-quark physics",
Prog. Part. Nucl. Phys. 63 (2009), arXiv:hep-ex/0904.2499.

[21] G. Degrassi et al., "Higgs mass and vacuum stability in the Standard Model at NNLO",
JHEP 08 (2012), arXiv:1205.6497.

[22] The Gfitter Group, M. Baak, M. Goebel et al.,
"The Electroweak Fit of the Standard Model after the Discovery of a New Boson at the LHC",
Eur. Phys. J. C72 (2012), DOI: 10.1140/epjc/s10052-012-2205-9,
arXiv:hep-ex/1209.2716v2.

[23] ATLAS Collaboration, "Determination of the Top Quark Mass with a Template Method in the All Hadronic Decay Channel using 2.04 fb^{-1} of ATLAS data", ATLAS-CONF-2012-030,
CERN, Mar. 2012.

[24] CDF Collaboration, T. Aaltonen et al.,
"Top quark mass measurement using the template method at CDF",
Phys. Rev. D 83, 111101(R) (2011), DOI: 10.1103/PhysRevD.83.111101,
URL: http://link.aps.org/doi/10.1103/PhysRevD.83.111101.

[25] D0 Collaboration, V. M. Abazov et al.,
"Measurement of the top-quark mass in $p\bar{p}$ collisions using events with two leptons",
Phys. Rev. D 86, 051103(R) (2012), DOI: 10.1103/PhysRevD.86.051103,
URL: http://link.aps.org/doi/10.1103/PhysRevD.86.051103.

[26] K. Y. Wong, "Studies of a top quark mass measurement in the dilepton channel using the mT2 variable at ATLAS", CERN-THESIS-2011-297, BONN-IB-2012-03,
MSc Thesis: University of Bonn, 2012.

[27] CMS Collaboration, "Mass determination in the $t\bar{t}$ system with kinematic endpoints",
CMS PAS TOP-11-027, CERN, Sept. 2012.

[28] M. Burns, K. Kong, K. T. Matchev et al., "Using Subsystem MT2 for Complete Mass Determinations in Decay Chains with Missing Energy at Hadron Colliders",
JHEP 0903 143 (2009), DOI: 10.1088/1126-6708/2009/03/143, arXiv:0810.5576.

[29] A. J. Barr and C. G. Lester,
"A review of the mass measurement techniques proposed for the Large Hadron Collider",
Journal of Physics G: Nuclear and Particle Physics 37.123001 (2010),
DOI: 10.1088/0954-3899/37/12/123001.

[30] CDF Collaboration, "Top quark mass measurement using m_{T2} in the dilepton channel at CDF",
Phys. Rev. D81.031102 (2010), arXiv:hep-ex/0911.2956.

[31] H. Cheng and Z. Han, "Minimal kinematic constraints and m_{T2}",
JHEP0812 (2008) 063 0812.063 (2008), arXiv:hep-ph/0810.5178.

[32] W. S. Cho et al., "Measuring the top quark mass with m_T2 at the LHC",
Phys.Rev. D78 034019 (2008), arXiv:hep-ph/0804.2185v1.

[33] C. Lester and D. Summers,
"Measuring masses of semi-invisibly decaying particles pair produced at hadron colliders",
Phys.Lett. B463.99–103 (1999), arXiv:hep-ph/9906349.

[34] O. S. Brüning et al., eds., *LHC Design Report. 1. The LHC Main Ring*,
CERN-2004-003-V-1, CERN-2004-003, Geneva, 2004,
URL: https://cdsweb.cern.ch/record/782076.

[35] O. S. Brüning et al., eds., *LHC Design Report. 2. The LHC infrastructure and general services*,
CERN-2004-003-V-2, CERN-2004-003, Geneva, 2004.

[36] *The LHC guide*, URL: large-hadron-collider.

[37] ATLAS Collaboration, ed.,
ATLAS Detector and physics performance technical design report, Volume 1.
CERN-LHCC-99-14, 1999.

[38] D. Acosta et al., eds., *CMS physics: Technical design report.*
CERN-LHCC-2006-001, CMS-TDR-008-1, 2006.

[39] K. Aamodt et al., "The ALICE experiment at the CERN LHC", *JINST* 3.S08002 (2008),
DOI: 10.1088/1748-0221/3/08/S08002.

[40] A. A. Alves et al., "The LHCb Detector at the LHC", *JINST* 3.S08005 (2008),
DOI: 10.1088/1748-0221/3/08/S08005.

[41] C. Lefèvre, *The CERN accelerator complex. Complexe des accélérateurs du CERN.*

[42] ATLAS Collaboration, ed.,
ATLAS Detector and physics performance technical design report, Volume 2.
CERN-LHCC-99-15, 1999.

[43] ATLAS Collaboration, G. Aad et al.,
"The ATLAS experiment at the CERN Large Hadron Collider", *JINST* 3.S08003 (2008),
DOI: 10.1088/1748-0221/3/08/S08003.

[44] *ATLAS photos*, URL: http://www.atlas.ch/photos/.

[45] ATLAS Pixel Collaboration, J. Grosse-Knetter et al., "The ATLAS pixel detector",
Nucl. Istrum. Meth. A 568.252 (2006).

[46] ATLAS Muon Collaboration and E. Diehl, "ATLAS Muon Detector Commissioning" (2009),
arXiv:physics.ins-det/0910.2767.

[47] ATLAS HLT/DAQ/DCS Group, ed.,
ATLAS High-Level Trigger, Data Acquisition and Controls (Technical Design Report),
CERN/LHCC/2003-022, 2003.

[48] ATLAS Pixel Collaboration, "Measurement of the top quark pair production cross section with ATLAS in pp collisions at $\sqrt{s}$ = 7 TeV", *Eur. Phys. J.* C71.1577 (2011).

[49] ATLAS Production Group, *Data Periods*, URL: https://atlas-taggervices.cern.ch/taggervices/RunBrowser/runBrowserReport/rBR_Period_Report.php.

[50] S. Ask et al., eds., *Report from the Luminosity Task Force.*
Tech. rep. ATL-GEN-PUB-2006- 002.CERN, 2006.

[51] ATLAS Collaboration, "Improved luminosity determination in pp collisions at $\sqrt{s}$ = 7 TeV using the ATLAS detector at the LHC" (2013), arXiv:1302.4393.

[52] *2011 pp Collisions*, URL: https://twiki.cern.ch/twiki/bin/view/AtlasPublic/LuminosityPublicResults\#2011_pp_Collisions.

[53] *2011 Data Periods for pp running*, URL: http://atlas-tagservice.cern.ch/tagservice/RunBrowser/runBrowserReport/rBRPeriodReport.php?fnt=data11*.

[54] S. Agostinelli and others, "GEANT4: A simulation toolkit",
Nucl. Instru. Meth. A506.250-303 (2003).

[55] ATLAS Production Group, *Top group's MC11(a,b,c) Samples For 2011 Data Analyses*,
URL: https://twiki.cern.ch/twiki/bin/viewauth/AtlasProtected/TopMC11.

[56] *Top Systematic Uncertainties 2011 rel 17. 2011*, URL: https://twiki.cern.ch/twiki/bin/viewauth/AtlasProtected/TopSystematicUncertainties2011.

[57] J. G. Salamanna et al., "Object selection and calibration, background estimations and MC samples for the Autumn 2012 Top Quark analyses with 2011 data",
ATL-COM-PHYS-2012-1197, CERN, 2012.

[58] ATLAS Muon Combined Performance Group, *MuidMuonCollection*, URL: https://twiki.cern.ch/twiki/bin/viewauth/AtlasProtected/MuidMuonCollection.

[59] M. Cacciari and G. P. Salam and G. Soyez, "The anti-kt jet clustering algorithm",
JHEP 04.:063 (2008).

[60] "Selection of jets produced in proton-proton collisions with the Atlas detector using 2011 data", Technical Report ATL-COM-PHYS-2012-067, CERN, 2012.

[61] ATLAS Collaboration, "Commissioning of the ATLAS high-performance b-tagging algorithms in the 7 TeV collision data", ATLAS-CONF-2011-102, CERN, 2011,
URL: https://cdsweb.cern.ch/record/1369219.

[62] A. K. Sinervo,
Definition and Treatment of Systematic Uncertainties in High Energy Physics and Astrophysics,
2003, URL: https://cdsweb.cern.ch/record/931829.

[63] ATLAS Collaboration, "Jet energy scale and its systematic uncertainty in proton-proton collisions at $\sqrt{s}$ = 7 TeV with ATLAS 2011 data", ATLAS-CONF-2013-004, CERN, 2013.

[64] ATLAS Collaboration, "Measurement of the Top Quark Mass in Dileptonic Top Quark Pair Decays with $\sqrt{s}$ = 7 TeV ATLAS data", ATLAS-CONF-2013-077, CERN, July 2013.

List of Figures

List of Tables